NASA CR 54691

McDonnell Report E368

Study of Arc-Jet Propulsion Devices

by

W. M. Van Camp

D.W. Esker

R.J. Checkley

W.G. Duke

J.C. Kroutil

S.E. Merrifield

R.A. Williamson

Prepared for

National Aeronautics and Space Administration

Contract NAS 3-5758

MCDONNELL

RESEARCH DIVISION

March 1966

Requests for copies of this report
should be referred to:

National Aeronautics and Space Administration
Scientific and Technical Information Facility
P.O. Box 33
College Park, Maryland 20740
Attn: NASA Representative RQT-2448

NASA CR-54691

McDonnell Report E368

Copy No. 39

March 1966

Study of Arc-Jet Propulsion Devices

Final Report

by

W.M. Van Camp

D.W. Esker

R.J. Checkley

W.G. Duke

J.C. Kroutil

S.E. Merrifield

R.A. Williamson

Prepared for

National Aeronautics

and Space Administration

Contract NAS 3-5758

Technical Management

NASA - Lewis Research Center

Cleveland, Ohio 44135

James S. Sovey

Henry R. Hunczak

RESEARCH DIVISION

MCDONNELL AIRCRAFT CORPORATION

LAMBERT - ST. LOUIS MUNICIPAL AIRPORT. BOX 516. ST LOUIS 66. MO.

PREFACE

The work described in this report was performed by McDonnell Aircraft Corporation under Contract NAS3–5758 for the Lewis Research Center of the National Aeronautics and Space Administration. The contract period was November 20, 1964 through December 19, 1965. Messrs. James Sovey and Henry Hunczak of NASA were technical managers of the program.

The work was accomplished in the Plasma Physics Research Laboratory under the direction of W.M. Van Camp. The project leader was D.W. Esker. The persons responsible for the research projects included in this program were:

Arc-jet thrustors	D.W. Esker J.C. Kroutil
Thrust	D.W. Esker
Mass flux	J.C. Kroutil
Impact pressure	J.C. Kroutil
Velocity	S.E. Merrifield R.A. Williamson
Stagnation enthalpy	D.W. Esker
Excitation temperature	R.J. Checkley
Electron density	W.G. Duke

Other personnel who contributed to the program were G.D. Rucker, A.J. Theiler, H.B. Crist, W.C. Good, C.R. Wheeler, and R.T. Turnbull.

CONTENTS

Summary v

1 Introduction 1

2 Arc-jet thrustors 3

3 Arc-jet performance measurements 9

4 Nozzle exit plane measurements 19

5 Power balance at nozzle exit plane 43

6 Arc region flow properties 51

7 Conclusions 57

8 Appendices

Appendix A – Thrust stand 61

Appendix B – Mass flux probe 63

Appendix C – Impact pressure probe 68

Appendix D – Photometric velocity meter 69

Appendix E – Stagnation enthalpy probe 81

Appendix F – Spectrophotometer 84

Appendix G – Langmuir probe 90

Appendix H – Test data 93

9 References 101

10 Distribution list 103

SUMMARY

The exhaust flow of arc-jet propulsion devices was studied with specialized diagnostic tools in order to identify factors in the energy transfer mechanism for the production of thrust and for the utilization of propellant energy; thereby, providing information leading to improvements in the design and performance of arc-jet propulsion devices.

The hydrogen thrustors used in the experimental program included 3 radiation-cooled and 3 water-cooled arc-jets of the constricted arc design, a regeneratively-cooled arc-jet of the semi-constricted arc design, and a water-cooled high current MPD arc-jet.

The constricted arc thrustors were operated over an arc power range of 6 to 42 kW and a hydrogen flow rate range of 3.5×10^{-4} to 5.5×10^{-4} lb/sec. The semi-constricted arc thrustor was operated at a power input of 30 kW and a hydrogen flow rate of 7.35×10^{-4} lb/sec and the MPD arc-jet was operated over a power range of 32 to 108 kW and a range of hydrogen flow rate of 0 to 1.32×10^{-4} lb/sec.

The thrust and specific impulse characteristics of each of the different thrustor configurations operating in a vacuum were obtained with a thrust stand. The measured thrust of the constricted arc units varied from 0.28 to 0.44 lbs and the specific impulse ranged from 700 to 1100 sec. The semi-constricted arc thrustor recorded a thrust level of 0.713 lb at a specific impulse level of 970 sec and the MPD arc-jet thrust ranged from 0.13 to 0.30 lb with a specific impulse range of 1000 sec to 2600 sec.

Nozzle exit plane profile measurements of mass flux, impact pressure, velocity, and stagnation enthalpy were obtained over 12 operating conditions of the water-cooled constricted arc thrustor and one operating condition on the regeneratively-cooled semi-constricted arc thrustor.

Mass flux profiles measured with a water-cooled mass flux probe exhibited dips on the exhaust centerline for both of the thrustor configurations. Integration of the profiles yielded 97% of the metered propellant flow rate for the semi-constricted arc thrustor and a range of 80 to 90% for the water-cooled arc-jet.

The impact pressure profiles were peaked on the exhaust centerline and asymmetric for the constricted arc thrustor and possessed a dip on the centerline for the semi-constricted arc thrustor. Integration of the pressure profiles resulted in thrust 88 to 100% of the measured thrust.

Velocity profiles were obtained by means of the dual photocell velocity meter and the combination of mass flux and impact pressure measurements. The profiles were peaked on the exhaust centerline for both arc-jet configurations; however, the semi-constricted arc profile was not as sharply peaked as the water-cooled arc-jet profiles.

Stagnation enthalpy profiles were obtained with a water-cooled calorimetric probe which peaked sharply on the exhaust centerline for both arc-jet configurations. The ratio of centerline enthalpy to bulk stagnation enthalpy ranged between 2.1 and 4.1.

Electron concentrations between 0.9×10^{13} and 2.0×10^{13} (electrons/cm^3) were measured on the constricted arc thrustor with a Langmuir probe while values between 1.0×10^{14} and 1.8×10^{14} electrons/cm^3 were obtained by spectroscopic techniques.

Total power flux profiles were obtained through a combination of the mass flux and stagnation enthalpy profiles which peaked sharply on the exhaust centerline for the constricted arc thrustor and were relatively flat for the semi-constricted arc unit. Integration of these profiles yielded a range of 75 to 100% agreement with the measured power in the exhaust flow.

The distribution of the kinetic power flux obtained from the velocity and mass flux measurements showed the largest concentration of kinetic power existed on the exhaust centerline. Integration of these profiles resulted in an estimate of the non-uniform losses of both arc-jets to be less than 5% of the input power.

The sum of the frozen flow and thermal power flux profiles resulted in a sharply peaked distribution which became more pronounced as the input power was increased.

A calculation of the gas temperature profiles for two operating conditions on the constricted arc-jet was made which resulted in a thermal power estimate of 7% of the input power for these two conditions.

A comparison of the measured exit plane profiles with an estimate of the flow conditions at the constrictor throat based on an equilibrium calculation indicated that a rapid mixing of the constrictor flow must occur in the nozzle expansion if the estimated throat conditions are to be consistent with the measured exit properties.

1 Introduction

The electrothermal arc-jet has been the subject of much research and development work in recent years and considerable progress has been made towards establishing a reliable configuration capable of operation for long durations.

Improvement of the thrust efficiency requires a detailed knowledge of the power losses occurring in the conversion of electrical power to kinetic thrust power. These losses include heat transfer to the thrustor body due to conduction, convection, radiation, and electron condensation from the high temperature plasma, frozen flow losses as a result of the rapid expansion, profile losses due to non-uniformities in exhaust flow, and expansion losses due to incomplete conversion of thermal to kinetic energy. Improvement of the thrust efficiency would also be enhanced by a knowledge of the mechanism of energy transfer from the arc to the gas.

In order to investigate the losses and energy exchange processes occurring in hydrogen arc-jets, various techniques have been under development at McDonnell under NASA contracts NAS8-2519 and NAS3–3562 for measuring the performance and exhaust jet characteristics. Initially, the work of the present contract, NAS3–5758, was to concentrate on measuring the performance and exit plane characteristics of three arc-jets: a radiation-cooled, a regeneratively-cooled, and a magneto-plasmadynamic (MPD) device. Since leakage difficulties were encountered with the radiation-cooled arc-jet early in the program, a water-cooled arc-jet having a similar internal configuration was substituted.

It is anticipated that the development of reliable measurement techniques, application of these techniques to determining the performance characteristics of the three types of arc-jets, and an analysis and comparison of these results will allow a better understanding of the thrust producing mechanism and lead to the design of devices having improved performance characteristics.

2 Arc-jet thrustors

Four different types of arc-jet thrustors were used in this work: radiation-cooled, water-cooled regeneratively-cooled, and magnetoplasmadynamic (MPD). Table 2.1 identifies the specific arc-jets on which performance and exhaust jet measurements were performed.

2.1 Radiation-cooled arc-jets

Performance measurements were obtained on three radiation-cooled arc-jets (NAS–1, MAC–2 and MAC–3). The arc-jets had the same general

Table 2.1 Identification of arc-jets used in experimental program

Arc-jet	Nozzle cooling	Type	Power range tested (kW)	Mass flow rate range tested (lb/sec) x 10^{-4}	Measurements performed	Ref. Fig.
NAS–1	Radiation	Constricted arc	6 – 30	4.5 – 6.5	Thrust, radiation power loss	2.1
MAC–2	Radiation	Constricted arc	6 – 30	4.5 – 5.5	Thrust	2.1
MAC–3	Radiation	Constricted arc	6 – 30	4.5 – 5.5	Velocity, radiation power loss	2.1
MAC–4	Water	Constricted arc	20 – 40	3.6 – 4.5	Exit plane mass flux, impact pressure, velocity profiles	2.2
MAC–5	Water	Constricted arc	10 – 42	3.5 – 4.5	Thrust, exit plane impact pressure, stagnation enthalpy, excitation temperature profiles and electron densities	2.2
MAC–7	Water	Constricted arc	20 – 35	3.6 – 4.5	Nozzle static pressure, electron density	2.2
GSC–2	Regenerative	Semi-constricted arc	30	7.35	Thrust, exit plane mass flux, impact pressure, velocity, stagnation enthalpy excitation temperature profiles	2.4
MAC–X–1	Water	Magnetoplasma-dynamic	30 – 86	1.32 – 0	Thrust	2.5

Note 1 – Arc-jets designated MAC–2,3,4,5, and 7 were designed and fabricated by McDonnell.

Note 2 – Arc-jets designated NAS–1 and GSC–2 were received from NASA Lewis Research Center.

configuration (constricted arc) as shown in Fig. 2.1. However, the NAS–1 thrustor had a smaller constrictor diameter. The cylindrical cathode is thoriated tungsten and is electrically isolated from the anode by a boron nitride spacer. The inner contour of the anode nozzle includes an arc chamber, a short constrictor, and a divergent section. The propellant enters the arc chamber through four 0.040 inch diameter holes drilled tangentially through the arc chamber wall at an angle of 20^{o} in the axial direction. The radial pressure gradient created by the tangential injection of the propellant stabilizes the arc and provides sufficient cooling to prevent constrictor erosion.

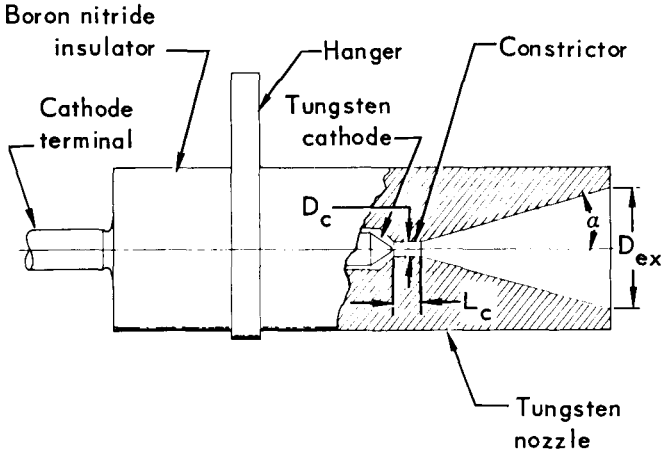

Note: All dimensions are in inches

	D	D_c	D_{ex}	L_c	α
NAS–1	1.875	0.150	1.500	0.300	15°
MAC–2 & 3	1.875	0.250	1.500	0.500	15°

Fig. 2.1 Radiation-cooled 30 kW arc-jet

The necessity of tangential injection for stable operation required a two component anode; a thoriated tungsten nozzle section and a molybdenum end cap form a plenum surrounding the arc chamber. The hydrogen propellant is admitted to the plenum through an inlet stem and passes through the injection holes into the arc chamber.

Difficulties were encountered with both of these arc-jets due to propellant leakage at the tungsten-molybdenum braze joint and propellant inlet stem after several hours of operating time. Attempts to obtain a reliable seal with this configuration were unsuccessful.

In view of the sealing difficulties with these radiation cooled thrustors, exit plane measurements originally scheduled for this thrustor were made on a water-cooled arc-jet.

2.2 *Water-cooled arc-jet*

Figure 2.2 presents the nozzle configuration for the water-cooled arc-jet of the constricted arc design. The cathode assembly for this unit was the same as for the radiation-cooled arc-jet. The internal dimensions of the nozzle contour was identical to the MAC–2 arc-jet (Fig. 2.1). The three arc-jets of this configuration were designated MAC–4, MAC–5, and MAC–7. Figure 2.3 is a photograph of the water-cooled arc-jet components.

2.3 *Regeneratively-cooled arc-jet*

Experimental measurements were made on a regeneratively-cooled arc-jet of the semi-constricted arc design. Figure 2.4 presents a sketch of this thrustor configuration. Two arc-jets units (designated GSC–1, and GSC–2) were used in the experimental program. The first unit (GSC–1), purchased from the Giannini Scientific Corporation, developed a gas leak at the braze joint near the thrustor exit plane after approximately

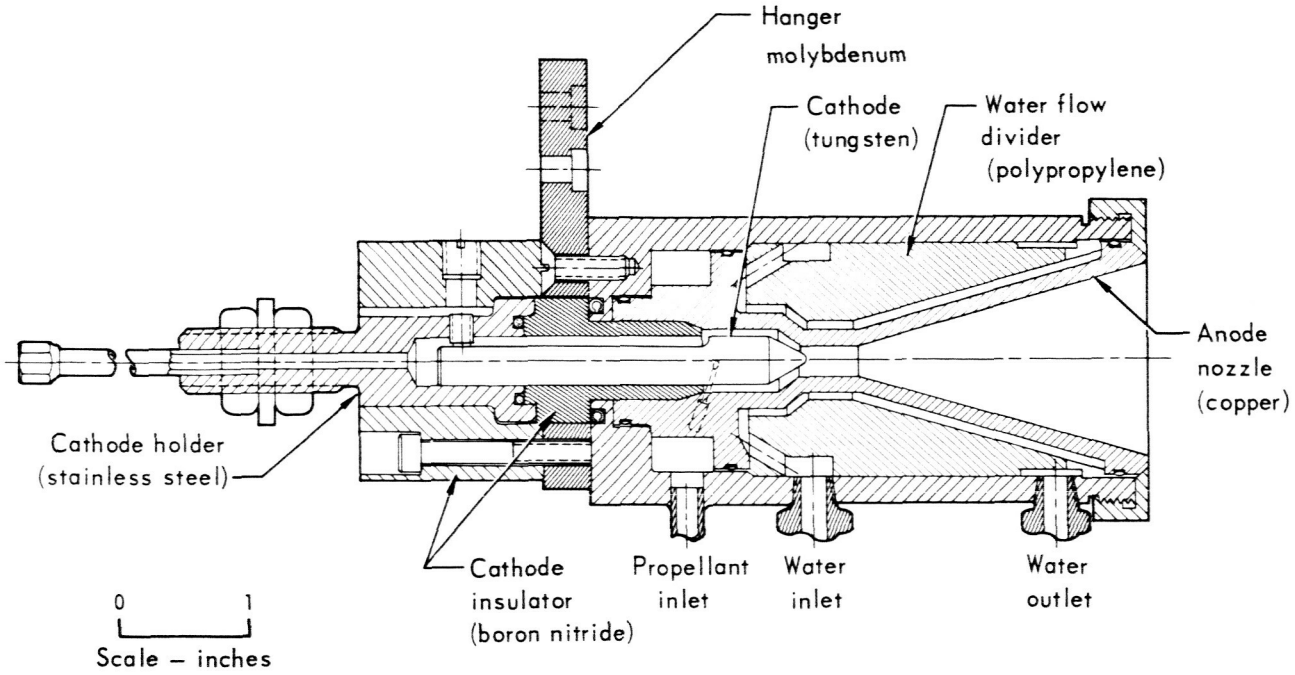

Fig. 2.2 Water-cooled arc-jet (MAC–5)

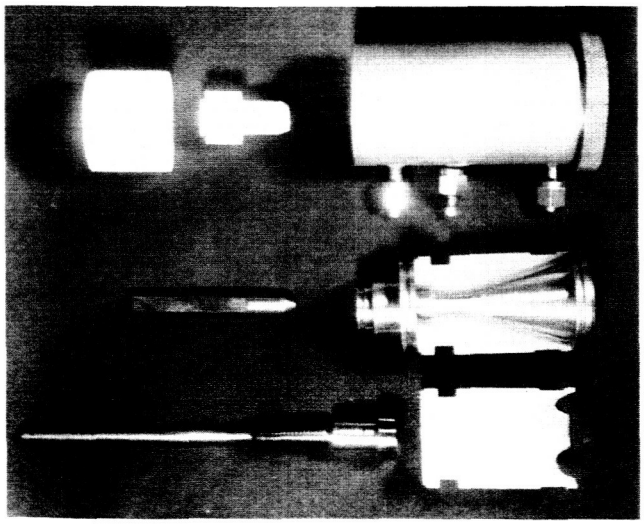

Fig. 2.3 Water-cooled arc-jet components

2.4 hours of test time. Continued operation of this arc-jet proved erratic and inspection of the unit upon disassembly revealed that the boron nitride insulator surrounding the cathode had failed.

A second regeneratively-cooled thrustor, made by Giannini, received from the NASA Lewis Research Center was designated GSC–2 and was used for the remainder of the program. This unit operated satisfactorily. A report of the development of the regeneratively 30 kW arc-jet is presented in Ref. 1.

The significant differences of this design as compared to the constricted arc design are the method of nozzle cooling and the arc chamber configuration. This arc chamber is designed such that the arc attachment region is within the arc chamber and does not pass into the divergent region.

Table 2.2 presents the dimensions of the GSC–2 thrustor configuration.

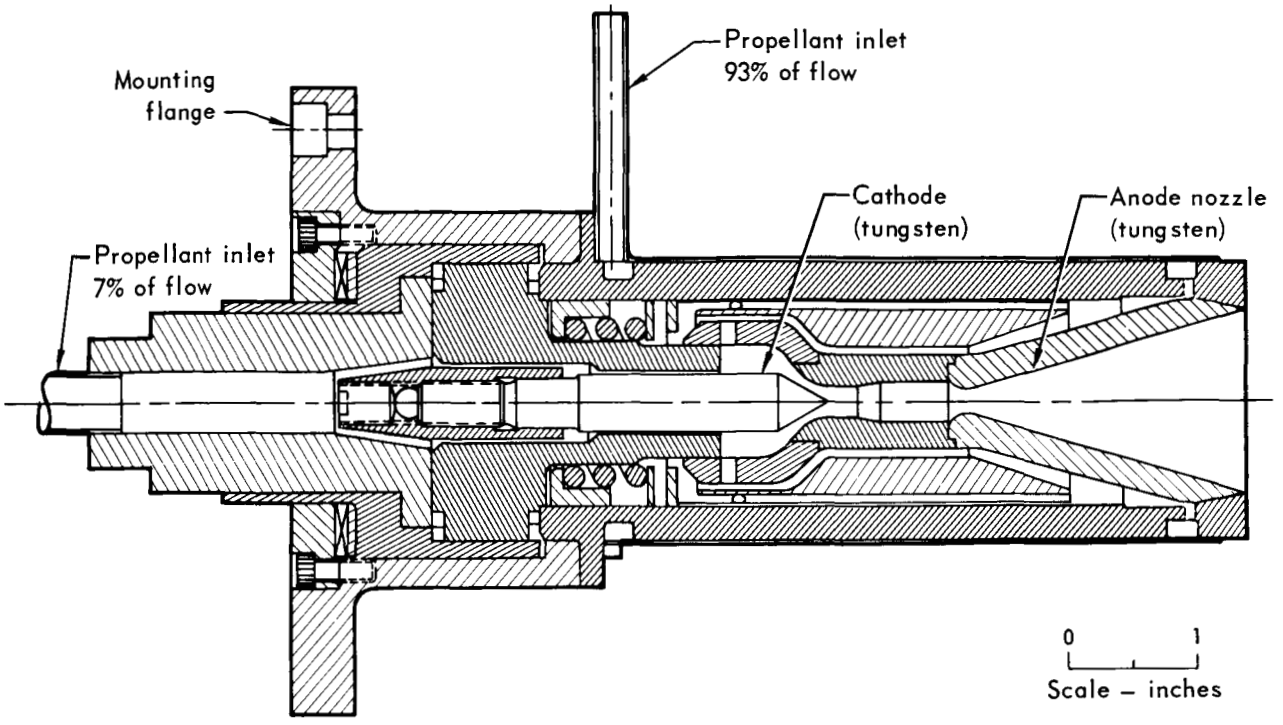

Fig. 2.4 Regeneratively cooled arc-jet (GSC–1, GSC–2)

2.4 MPD arc-jet

The MPD arc-jet is shown in Fig. 2.5. This thrustor is a laboratory device incorporating a water-cooled tungsten cathode, copper nozzle, and copper anode. The throat diameter is 0.5 inches and the exit area ratio is 19.8. The essential features of this arc-jet are (a) cooling passages designed for high heat transfer rates, (b) variable gas injection ports to determine the effect of gas injection angle on thrustor performance, (c) isolated anode so that the ratio of anode current collecting diameter to cathode arc diameter would be as large as possible. This enhances the thrust contribution due to the induced magnetic field – arc current interaction sometimes referred to as the "self-blowing interaction."

Table 2.2 Dimensions of regeneratively-cooled arc-jet (GSC–2)

Arc chamber diameter (inlet)	0.250 in.
Arc chamber diameter (maximum)	0.312 in.
Arc chamber length (nominal)	1.125 in.
Nozzle throat diameter	0.187 in.
Nozzle cone half-angle	15°
Nozzle area ratio	60:1
Cathode-anode gap (minimum)	0.060 in.
Cathode tip angle (total)	60°

2.5 Arc-jet test facilities

The subsystems necessary for hydrogen arc-jet operation include electrical power supplies, a

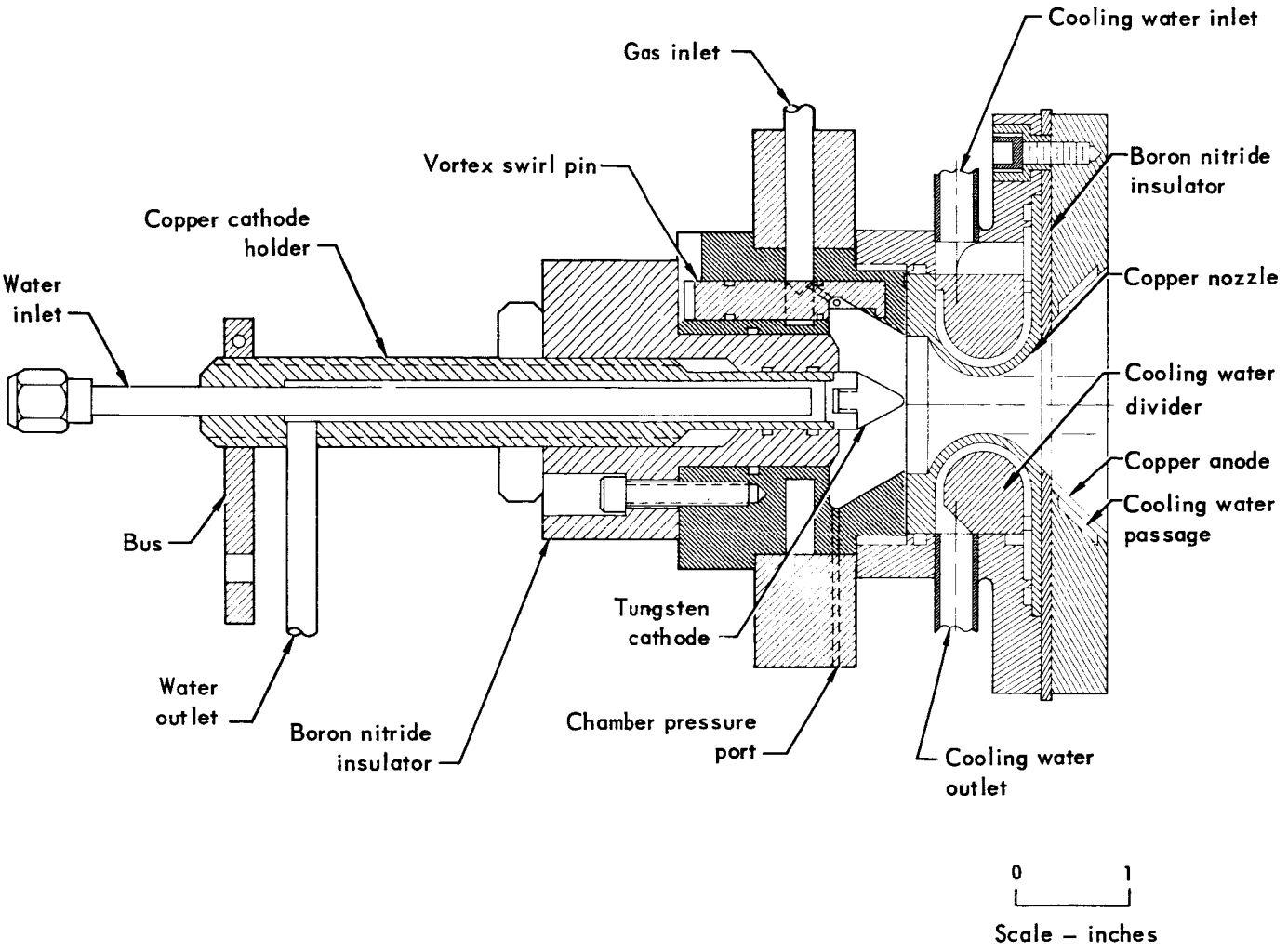

Fig. 2.5 MPD arc-jet (X–1)

vacuum system, instrumentation, and propellant supply system.

Power supplies – All arc-jet tests except those performed on the MPD arc-jet were conducted using a 60 kW Miller (type SR 1500 F–1, special) as the electrical supply for the arc load. This power supply has a three phase full-wave rectifier with saturable reactor current control providing the necessary drooping output characteristic. To obtain the minimum sparking potential of hydrogen, a 400 volt open circuit voltage was used.

A one megawatt A.O. Smith power unit was used for the MPD arc-jet tests since the operating power of this jet was above the capacity of the Miller unit. The one megawatt unit is also three phase, full rectified with saturable reactor current control.

Vacuum systems – Two vacuum systems were employed in the experimental program. The tests performed on the NAS–1, MAC–2, MAC–4, MAC–5, and MPD arc-jets were conducted in a mechanical vacuum system, consisting of two mechanical booster assemblies, a holding pump,

four 16 inch diameter oil booster pumps, and other valving, fillers and piping. This system has a pumping capacity of 4×10^{-4} lb/sec of hydrogen at 0.4 torr. A two stage heat exchanger consisting of water and liquid nitrogen baffles was located in the vacuum tank to protect the pumping system and improve the pumping characteristics. Five different test sites were used for the diagnostic and performance tests to better utilize the vacuum system.

The GSC–2 arc-jet tests were performed in a 6-foot diameter steam ejector vacuum system. This system was capable of maintaining the background pressure of hydrogen at 0.2 torr at a flow rate of 7.35×10^{-4} lb/sec.

Instrumentation – The instrumentation of the hydrogen arc-jets and vacuum system was designed to measure the parameters shown in Table 2.3. All electrical signals were continuously recorded on a direct print oscillograph at a paper speed of 0.25 inches per second.

Table 2.3 Description of instrumentation

Parameter	Measurement	Method of measurement
Power input	Arc voltage	D.C. Voltmeter and oscillograph recording of voltage divider network
	Arc current	D.C. Ammeter and oscillograph recording of 50 mV shunt output
Propellant flow rate	Flowmeter pressure	Bourdon gauge and oscillograph recording of transducer output
	Flowmeter temperature	Oscillograph recording of copperconstantan thermocouples
Power loss	Inlet and outlet cooling water temperature (8)	Oscillograph recording of copperconstantan thermocouples
	Cooling water flow rates (3)	"Rotameter" flow meters
System pressures	Swirl chamber	Bourdon and aneroid gauges
	Arc chamber	Aneroid gauge and oscillograph recording of transducer output
	Ambient exhaust* (vacuum)	Aneroid gauge, thermopile gauge, ionization gauge, and oscillograph recordings of an ionization gauge output
	Nozzle (static)	Aneroid gauge and thermopile vacuum gauge

Propellant supply to the thrustors from eight 2000 psi storage bottles was manifolded and regulated to 75 psi supply pressure. The flow was then throttled by a needle valve into a sonic nozzle flowmeter. The stagnation pressure upstream of the flowmeter was used in conjunction with precision calibrations to set the mass flow rate.

The arc-jet cooling water was supplied continuously at a constant head of 200 psi by a turbine water pump.

2.6 *Test procedure*

Prior to starting the arc-jet, the test section and arc chamber were evacuated and purged with an inert gas. Hydrogen was then introduced into the arc chamber until the pressure exceeded 50 torr at which time an open circuit voltage of 400 volts was applied across the electrodes of the arc-jet.

The hydrogen flow was then stopped. When the arc chamber pressure fell to approximately 2 torr, the arc initiated, at which time the hydrogen flow was initiated, thus stabilizing the arc. The desired operating condition was then set by adjusting either the hydrogen flow and/or the supply current. Visual observations were made during operation to insure proper expansion of the gas in the nozzle.

During the test a continuous oscillograph recording was made of all operating parameters except the cooling water flow-rate. When a test was made using a diagnostic device, the water flow rate and many of the same operation parameters being recorded on the oscillograph were read and recorded.

Normal shut down consisted of turning off the power supply, then the hydrogen flow followed by an inert gas purge of the vacuum system.

3 Arc-jet performance measurements

Performance and operating data obtained for the arc-jets are summarized in Table 3.1.

The measurement of the arc-jet thrust, combined with the propellant mass flow-rate, and power input is sufficient to define the performance of the arc-jet. The specific impulse is obtained from the relation.

$$I_{sp} = \frac{T}{\dot{m}} \qquad (1)$$

where I_{sp} = specific impulse (sec)

T = thrust (lb)

m = propellant mass flow-rate (lb/sec)

The thrust efficiency of the arc-jet is the ratio of kinetic thrust power to input power and is given by

$$\eta_{Thrust} = 0.0218 \frac{T^2}{P_{IN}\dot{m}} \qquad (2)$$

where η_{Thrust} = thrust efficiency

P_{IN} = power input (kW)

The power input is calculated from

$$P_{IN} = IV \times 10^{-3}$$

where I = arc current (amps)

V = arc voltage (volts)

The arc-jet thrust measurements were obtained with two thrust stands which are described in Appendix A.

Table 3.1 Arc-jet performance and operating ranges

Arc-jet	NAS-1	MAC-2	MAC-5	GSC-2	MAC-X-1
Thrust (lb)	0.22–0.43	0.21–0.40	0.22–0.45	0.713	0.15
Specific impulse (sec)	380–970	380–800	510–1120	970	1140–2280
Thrust efficiency (%)	21.8–24.8	17.8–23.8	22.3–26.6	52.6	10.6–17.5
Power input (kW)	60–35.7	6.0–30.0	10.3–50.7	30.5	35–108
Arc voltage (volts)	152–251	126–190	131–148	212	85–96
Arc current (amps)	34–211	33–199	33–378	141	300–1200
Propellant flow rate (lb/sec) x 10^{-4}	3.5–5.5	3.5–5.5	3.6–4.5	7.35	0–1.32

3.1 Performance of radiation-cooled arc-jets

NAS–1 Radiation-cooled arc-jet

Thrust – Figure 3.1 (a) shows the thrust characteristics of the NAS–1 arc-jet. The cathode gap was 0.130 inch and the constrictor section had a 0.060 inch radius at the inlet. The cathode gap distance is determined by extending the cathode forward until it seats against the constrictor inlet and then retracting at a measured length. Three representative flow rates were chosen and the power varied over the operating range of the arc-jet. The data are reproducible to within 5% over the series of three tests. Figures 3.1 (b) and 3.2 are cross plots showing thrust and specific impulse as a function of propellant flow rate. The thrust efficiency for this arc-jet as a function of power input is shown in Fig. 3.3.

Electrical characteristics – Figure 3.4 presents the arc voltage – current dependence for various propellant flow rates as measured on the NAS–1 arc-jet. The typical arc negative resistance characteristic is apparent. For the 100 to 200 amp current range the voltage decreases in a linear manner.

Arc chamber pressure – The pressure in the arc chamber was measured at a position adjacent to the cathode and at the rear of the arc chamber. The data were obtained during the thrust measurements and are plotted in Fig. 3.5. As shown the chamber pressure increases approximately, linearly with power input.

Arc efficiency – Figure 3.6 shows the radiation calorimeter used to measure arc efficiency, which is defined as the ratio of input power minus the power radiated from the arc-jet to the input power. The calorimeter is a double-walled water-cooled copper cylinder that completely encloses the thrustor except at the exit plane. The arc efficiencies as measured on the NAS–1 thrustor are presented in Fig. 3.7. For the power range tested the arc efficiency ranges from 90 to 98%, with the highest efficiencies recorded at the highest mass flow rates.

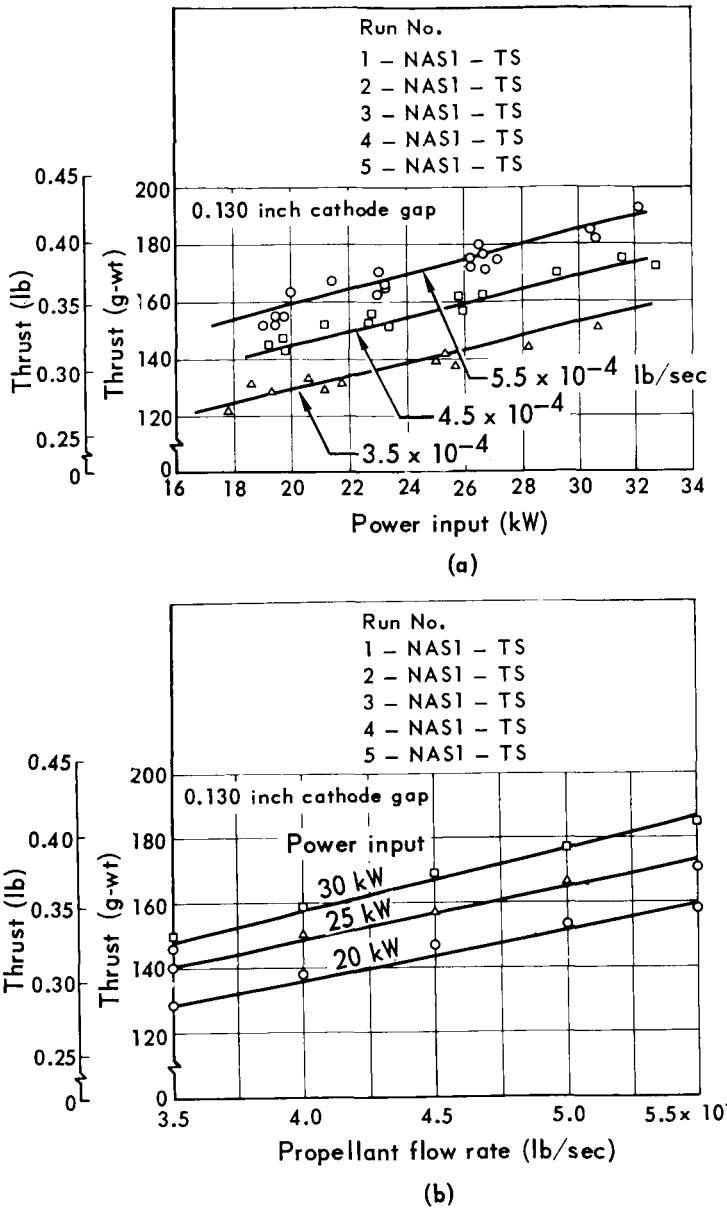

Fig. 3.1 Thrust characteristics of NAS–1 radiation-cooled thrustor

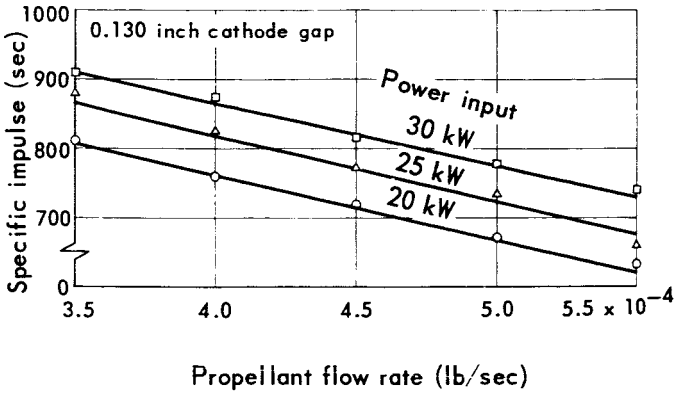

Fig. 3.2 Specific impulse characteristics of NAS–1 radiation cooled thrustor

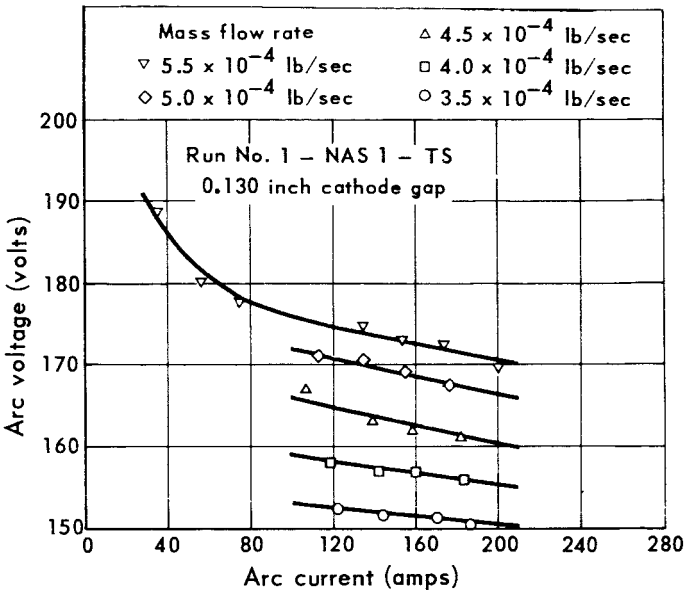

Fig. 3.4 Electrical characteristics of NAS–1 radiation-cooled arc-jet

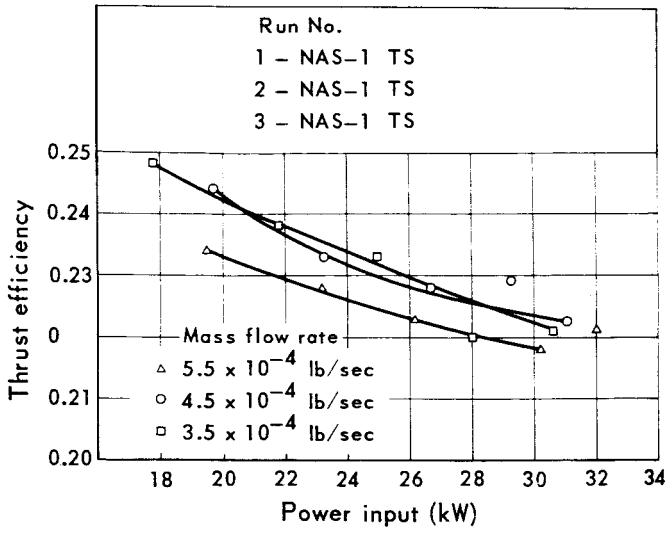

Fig. 3.3 Thrust efficiency of NAS–1 radiation-cooled arc-jet

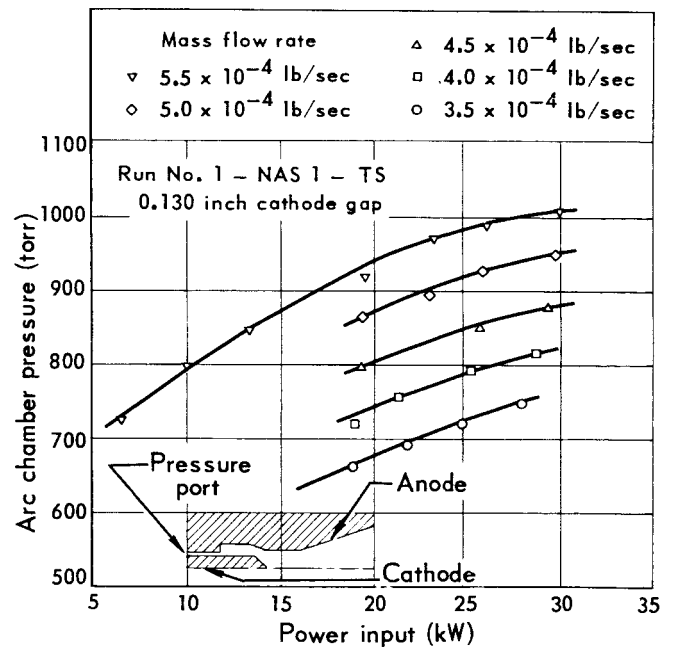

Fig. 3.5 Arc chamber pressure on NAS–1 radiation-cooled arc-jet

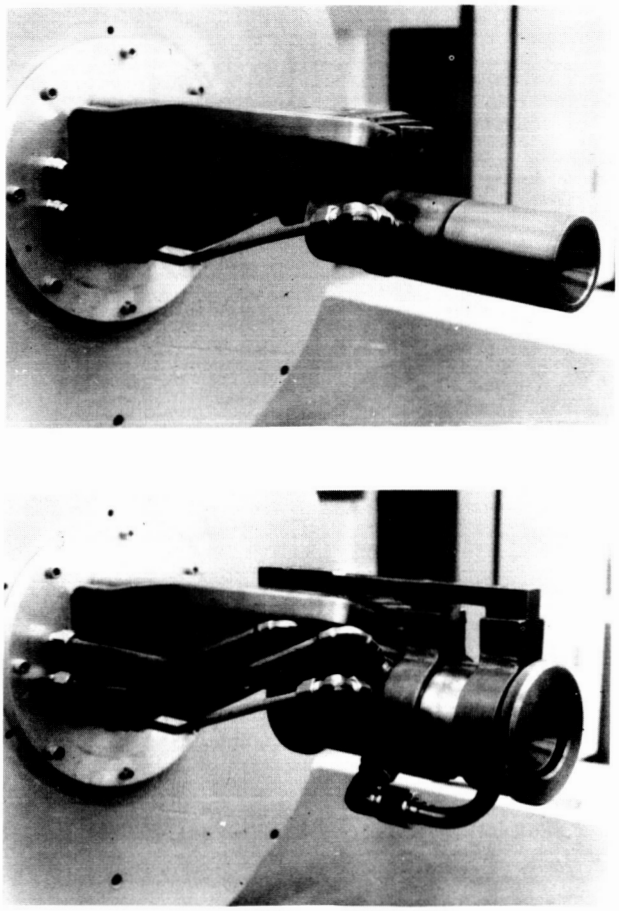

Fig. 3.6 NAS–1 radiation-cooled arc-jet with and without calorimeter

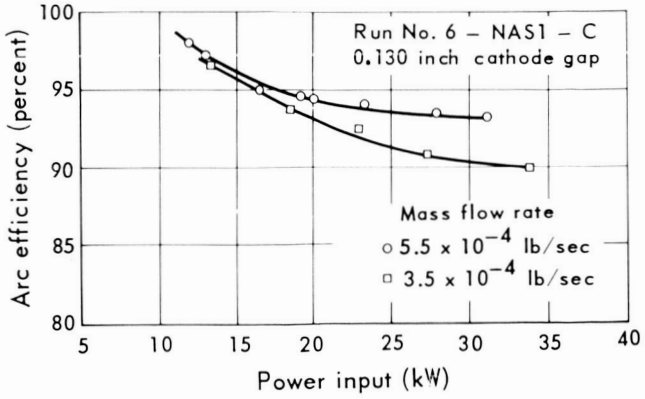

Fig. 3.7 Arc efficiency of NAS–1 radiation-cooled arc-jet

MAC–2, MAC–3 Radiation-cooled arc-jets

Thrust – The thrust characteristics of the MAC–2 radiation-cooled arc-jet are presented in Fig. 3.8 (a) for an electrode gap of 0.300 inches. Thrust levels are lower for this arc-jet than the NAS–1 at comparable operating conditions. Figures 3.8 (b) and 3.9 show the specific impulse characteristics of this arc-jet as a function of mass flow and power input. The thrust efficiency is plotted in Fig. 3.10 and the data are lower than the NAS–1 efficiencies by approximately 1 to 2% over the range tested.

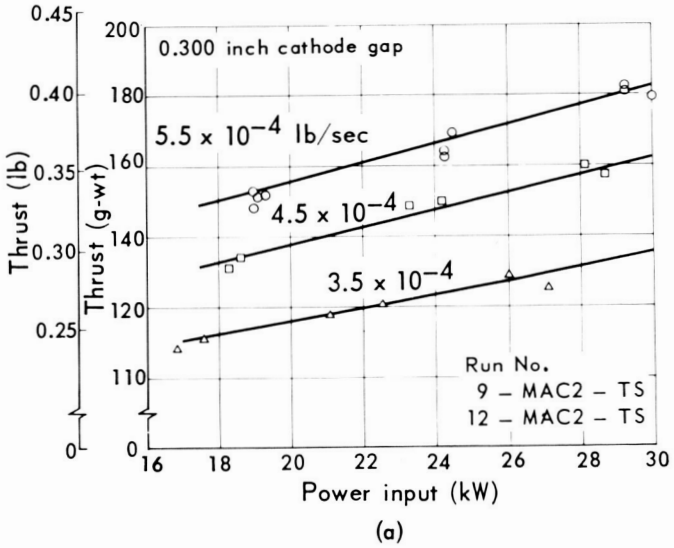

(a)

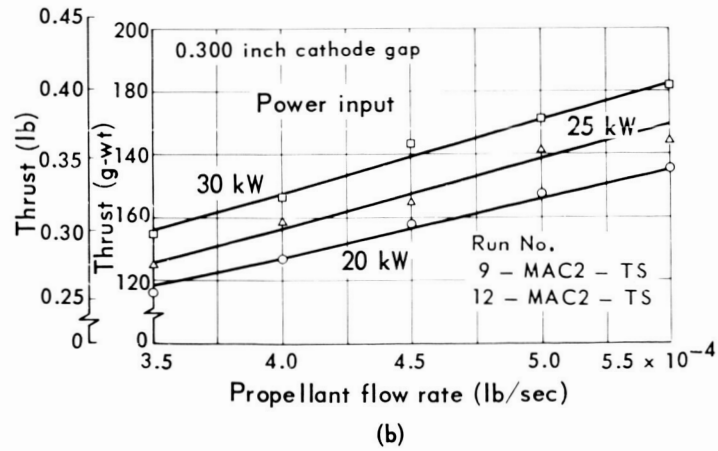

(b)

Fig. 3.8 Thrust characteristics of MAC–2 radiation-cooled thrustor

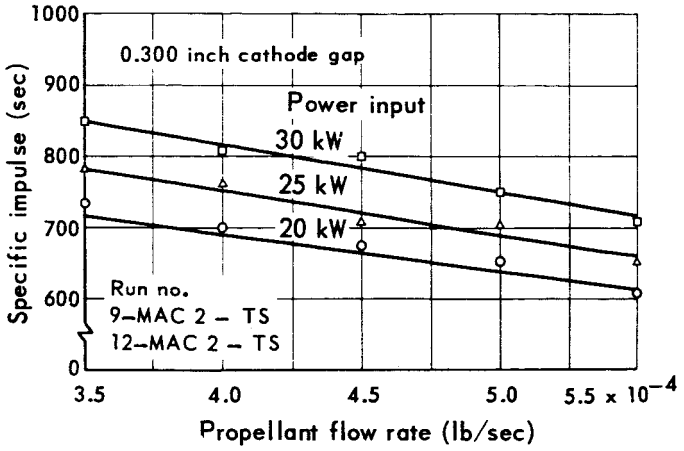

Fig. 3.9 Specific impulse characteristics of MAC–2 radiation-cooled thrustor

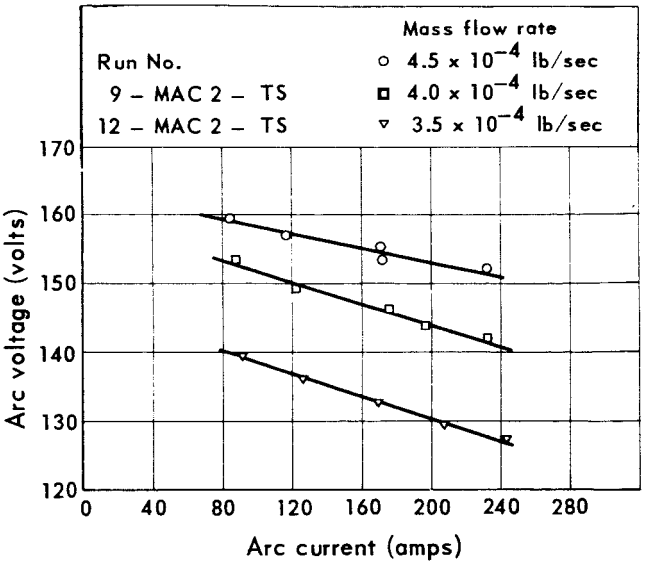

Fig. 3.11 Electrical characteristics of MAC–2 radiation-cooled arc-jet

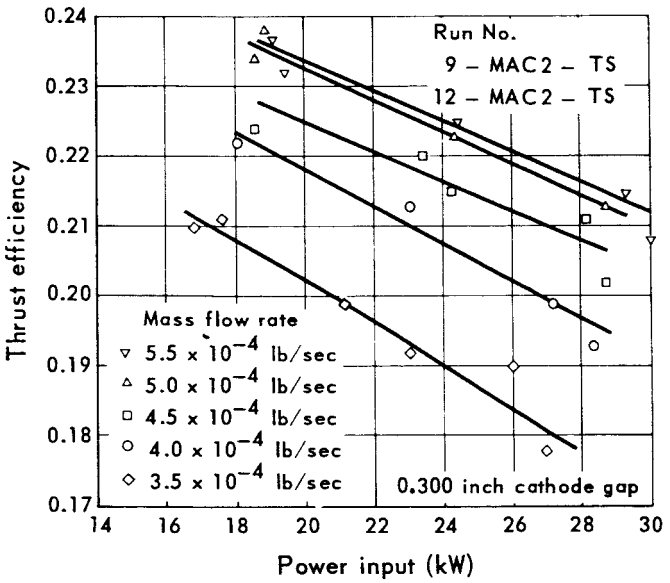

Fig. 3.10 Thrust efficiency of MAC–2 radiation-cooled arc-jet

Electrical characteristics – The arc voltage-current relationship for the MAC–2 arc-jet is presented in Fig. 3.11. The general dependence of voltage with current is similar to the NAS–1 thrustor; however, the voltages are lower by approximately 15 volts at a given current and mass flow rate. The lower voltage is due to the decreased chamber pressure resulting from the larger throat diameter.

Arc chamber pressure – Figure 3.12 shows the variation of arc chamber pressure with arc input power and propellant mass flow rate. As pointed out above, the pressures are lower than the NAS–1 arc-jet by approximately 415 torr at 30 kW.

Arc efficiency – Failure of the main braze joint of the MAC–2 arc-jet occurred before calorimeter measurements could be obtained. However, measurements were obtained on the MAC–3 radiation-cooled unit which was identical in design and configuration. The electrical and arc chamber characteristic of these two arc-jets were within 1% of each other. Figure 3.13 is a plot of the MAC–3 arc efficiency versus power input.

The arc efficiency of the MAC–2 and –3 configurations is approximately 3 to 5% lower than the NAS–1 configuration and as such may account for the difference in thrust efficiencies for these two arc-jets. The greater power loss by radiation is

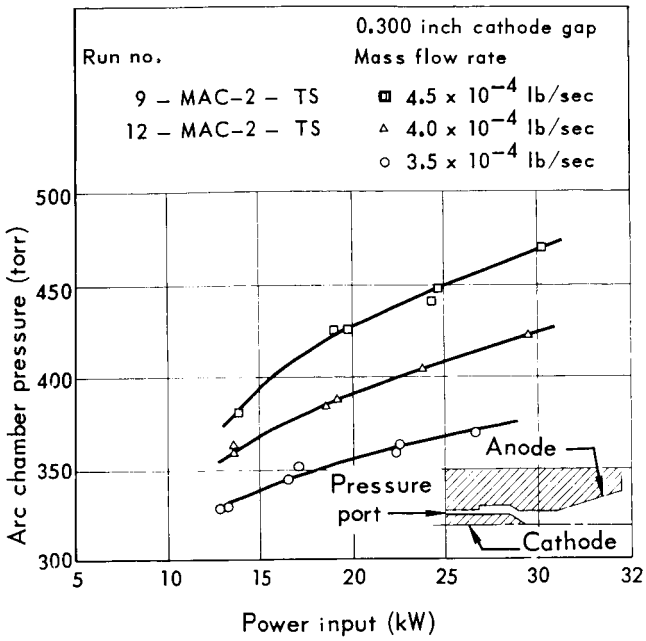

Fig. 3.12 Arc chamber pressure on MAC–2 radiation-cooled arc-jet

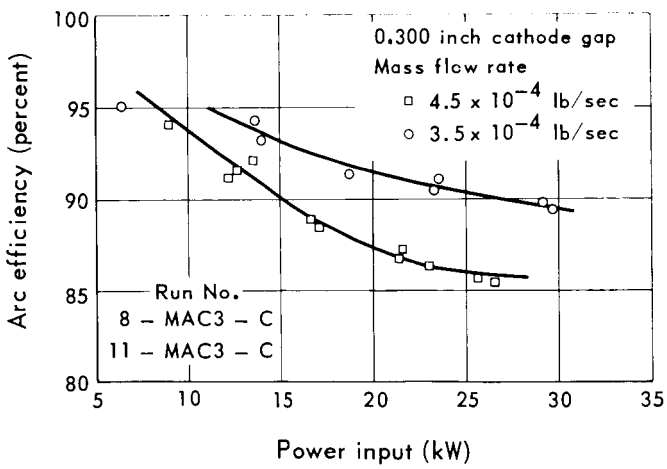

Fig. 3.13 Arc efficiency of MAC–3 radiation-cooled arc-jet

due to the somewhat larger surface area exposed to the plasma and the larger current levels which are required at a given power level. The anode loss which is due to condensation of electrons at the anode surface is proportional to the current level.

3.2 *Performance of water-cooled arc-jets*

Three water-cooled arc-jets were fabricated which had the identical internal configuration as the MAC–2 and –3 radiation-cooled arc-jets. These water-cooled arc-jets were designated MAC–4, MAC–5 and MAC–7.

Thrust – Figure 3.14 (a) shows the thrust as a function of input power and hydrogen flow rate for the MAC–5 arc-jet. The cathode gap for these tests was 0.300 inches. Three flow rates were

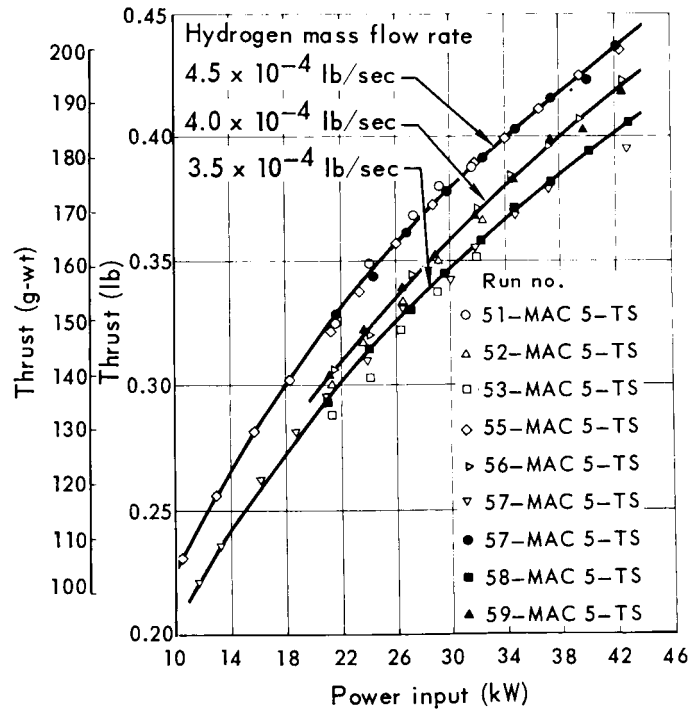

Fig. 3.14(a) Thrust characteristics of MAC–5 water-cooled thrustor

chosen and the power was varied over the operating range. Figure 3.14 (b) is a plot of the thrust as a function of hydrogen flow rate and is obtained by a cross plot of Fig. 3.14 (a). Specific impulse characteristics are presented in Fig. 3.15 as a function of input power and flow rate.

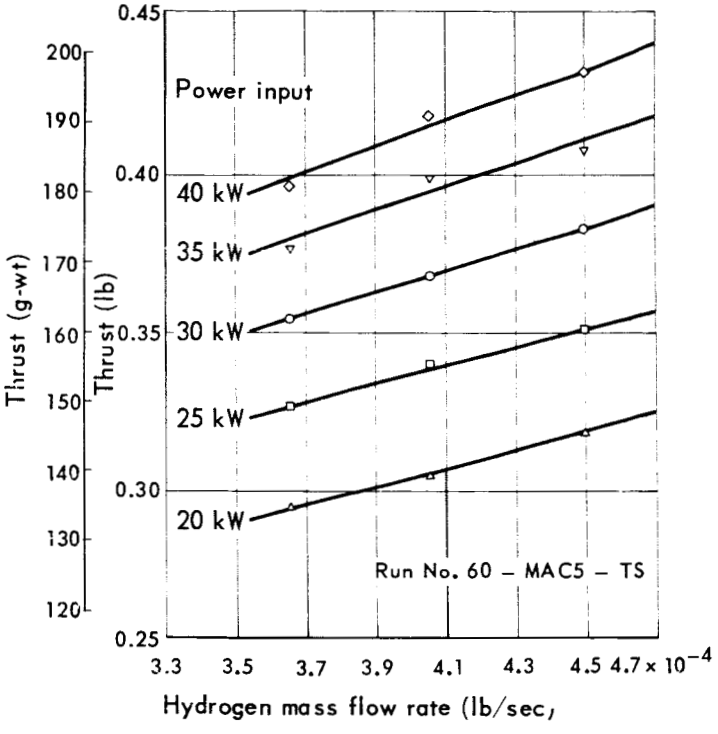

Fig. 3.14(b) Thrust characteristics of MAC–5 water-cooled thrustor

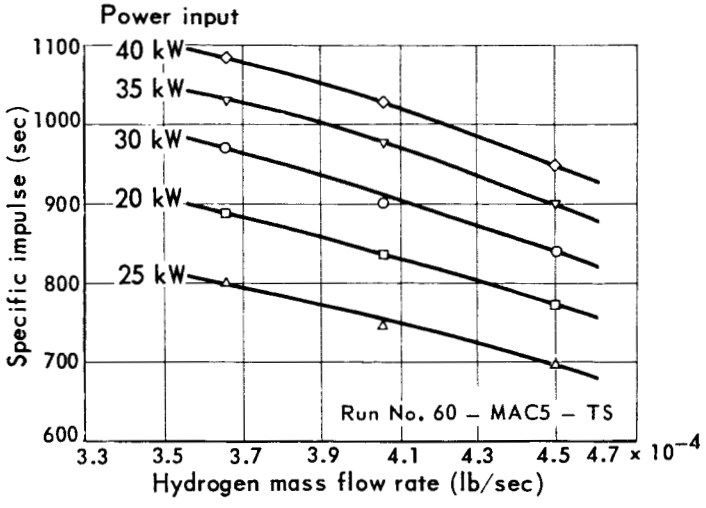

Fig. 3.15 Specific impulse characteristics of MAC–5 water-cooled thrustor

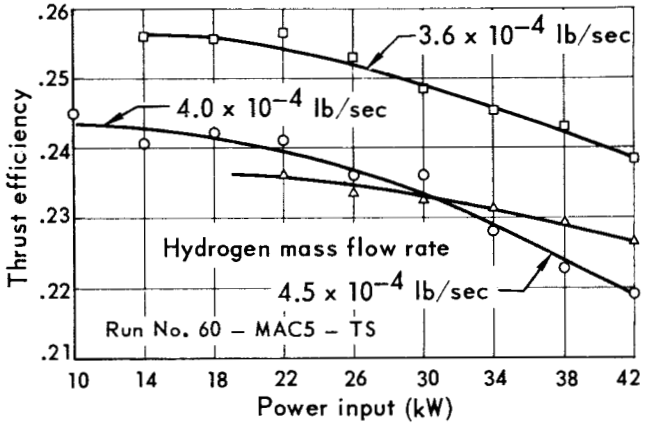

Fig. 3.16 Thrust efficiency characteristics for MAC–5 arc-jet

Comparison of the thrust efficiency data (Fig. 3.16) with that obtained on the MAC–2 arc-jet indicates the water-cooled arc-jet performance is slightly higher than the radiation-cooled version. This result is in contrast with the results reported in Ref. 2 wherein it is concluded that the thrust efficiency was a strong function of the nozzle wall temperature.

Electrical characteristics – Figure 3.17 presents the arc voltage-current characteristics for the MAC–5. The voltages are lower than the MAC–2 radiation-cooled arc-jet at comparable operating conditions and is most probably due to the decreased arc chamber pressure for the water-cooled unit. The electrical characteristics of the MAC–4 and MAC–7 arc-jets were similar to the MAC–5 curves and were within ±3% of each other for the full range of conditions tested.

Arc chamber pressure – The arc chamber pressure – power input relation (Fig. 3.18) for the MAC–5 arc-jet is approximately linear for the 10

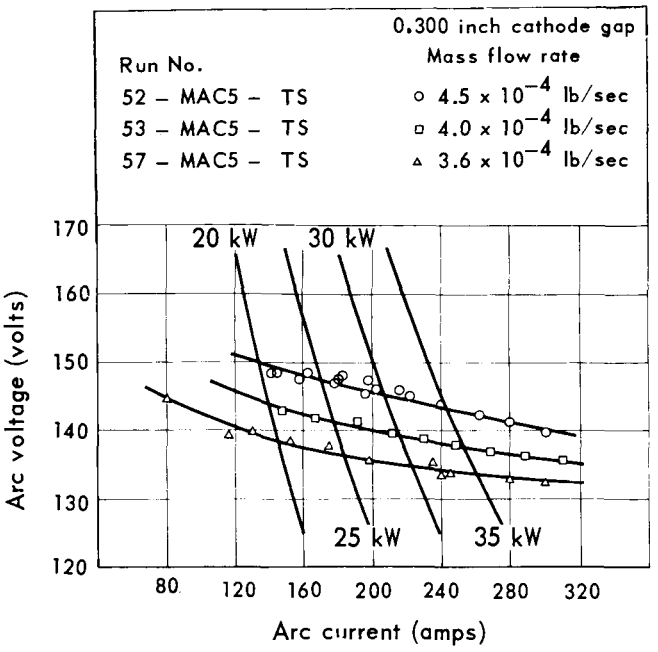

Fig. 3.17 Electrical characteristics of MAC–5 water-cooled arc-jet

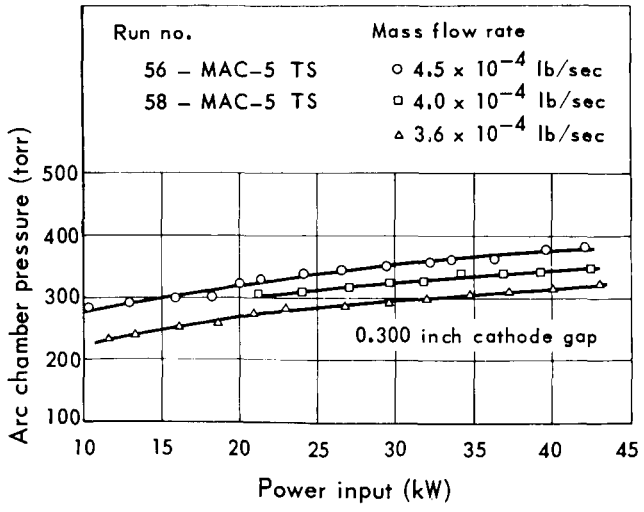

Fig. 3.18 Arc chamber pressure on MAC–5 water-cooled arc-jet

to 42 kW power range. The magnitude of the pressures is lower than the MAC–2 radiation-cooled arc-jet by approximately 102 torr at the 30 kW level. The chamber pressure relations for the MAC–4 and MAC–7 arc-jet were within 3% of the MAC–5 data.

Arc efficiency – Figure 3.19 presents the arc efficiency for the MAC–5 arc-jet. The arc efficiency is the ratio of the power input minus the power losses transferred to the nozzle cooling water to the power input. The efficiency shows only a slight dependence on propellant mass flow rate and is 9 to 13% lower than the MAC–2 radiation arc-jet. Since the arc efficiency is lower for the water-cooled configuration, the conversion of thermal energy to kinetic energy must be more efficient in the water-cooled unit for the overall thrust efficiency was higher on this unit than on the radiation arc-jet.

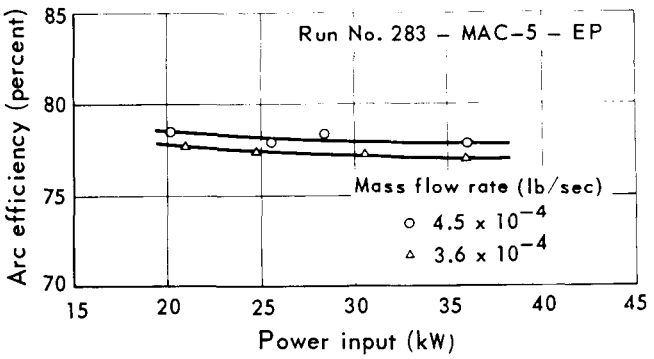

Fig. 3.19 Arc efficiency of MAC–5 water-cooled arc-jet

3.3 *Performance of regeneratively-cooled arc-jets*

All tests on the regeneratively-cooled thrustor GSC–2 were conducted at a nominal operating condition of 1000 sec specific impulse and power input of 30 kW. Three tests of the GSC–2 arc-jet

were made on the McDonnell thrust stand to compare the thrust measurements made at the Giannini Scientific Corporation.

A total of 15 thrust measurements were made at the 30 kW, 7.35 x 10^{-4} lb/sec operating condition during these three tests. The average of these data was 0.708 lb with an average deviation of ±0.004 lb.

A comparison of thrust readings obtained with that measured by Giannini is presented in Table 3.2.

A typical set of operating parameters obtained during the initial tests of this thrustor is presented in Table 3.3.

Continued operation of this thrustor conducted for exit plane measurements resulted in an increasing voltage characteristic. After approximately 32 hours of operation the parameters of Table 3.3 were measured.

The increasing voltage trend was also observed during the 500 hour lifetime test of this thrustor configuration (Ref. 3).

Table 3.3 Effect of run time on operating parameters

	Initial test	After 32 hours run time
Power input (kW)	30.9	30.4
Arc voltage (volt)	212	232
Arc current (amp)	146	131
Hydrogen mass flow rate (lb/sec)	7.35 x 10^{-4}	7.37 x 10^{-4}
Arc chamber pressure (torr)	959	984

Table 3.2 Comparison of McDonnell and Giannini thrust and specific impulse data on GSC–2 arc-jet

Tested by	Power input (kW)	Hydrogen flow rate (lb/sec)	Tank pressure (torr)	Thrust measurement			Specific impulse (sec)	Thrust efficiency (%)
				(P_eA_e*) (lb)	Reading (lb)	Total (lb)		
MAC	0	7.35 x10^{-4}	0.22	0.005	0.198	0.203		
MAC	30.0	7.35 x10^{-4}	0.22	0.005	0.708	0.713	970	50.3
GSC	0	7.30 x10^{-4}	0.90	0.020	0.180	0.200		
GSC	30.0	7.30 x10^{-4}	0.65	0.013	0.714	0.727	996	52.6

*P_eA_e = Includes correction for finite background pressure

3.4 *Performance of MPD arc-jet*

Thrust – Preliminary performance measurements on the MPD arc-jet (Fig. 2.5) were obtained during this program.

The first tests of the MPD arc-jet were made with a 6 turn water-cooled solenoid mounted around the anode. This coil had a nominal diameter of 6.5 inches and was connected in series with the arc discharge. Figure 3.20 presents the thrust versus power input of this configuration for a constant mass flow of 1.32×10^{-4} lb/sec.

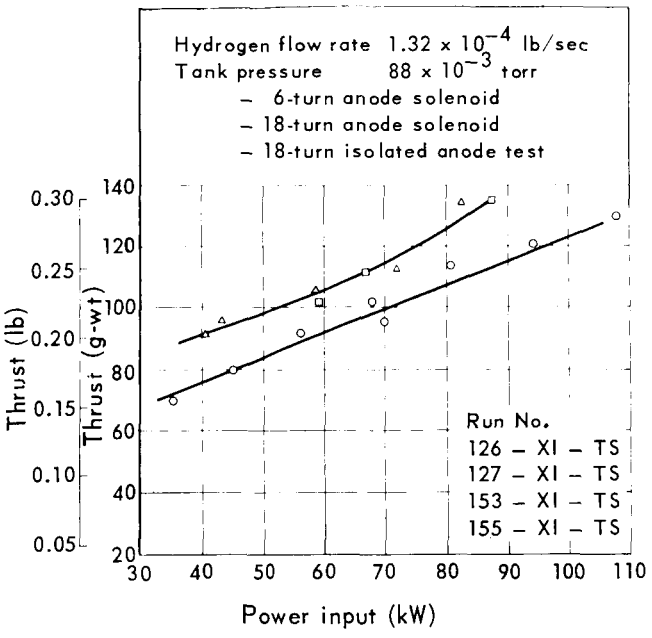

Fig. 3.20 Thrust characteristics of MPD arc-jet

To increase the specific impulse for a given power input the anode was redesigned to accept a larger solenoid. The internal geometry of the anode was held constant and the outside diameter of the anode was reduced to accommodate an 18 turn coil of 3 inches inner diameter and 7.5 inches outer diameter. As before, the solenoid was connected in series with the arc discharge.

The second test was conducted with the 18 turn solenoid at a mass flow of 1.32×10^{-4} lb/sec. The results of this test are also plotted on Fig. 3.20. The thrust values obtained on this test are approximately 15% higher than the first test indicating an increased interaction with the solenoid field. These tests were conducted with the anode and throat section in electrical contact. Visual observation indicated that the arc terminated in a region just beyond the throat.

A test of the MPD arc-jet with the 18 turn solenoid was conducted during which the anode was isolated from the throat section. This was done to increase the arc attachment radius from 0.25 inches to approximately 1.0 inch. This change should produce a significant increase in thrust if the predominant thrust mechanism is an interaction of the arc current with its own magnetic field. This interaction is a function of the ratio of the anode to cathode arc radius. The mass flow rate for this test was set at 1.32×10^{-4} lb/sec and the power was varied from 60 to 86 kW. The arc discharge was slightly unstable at currents above 600 amps. The three thrust measurements obtained on this test are plotted on Fig. 3.21 and fall essentially on the non-isolated anode thrust curve.

Zero mass flow rate test – A test was made on the MPD arc-jet with the 18 turn solenoid, during which the propellant mass flow rate was slowly reduced from 1.32×10^{-4} lb/sec to a zero mass flow condition. The radiation from the exhaust plane was characteristic of hydrogen at all flow rates except the zero flow condition. At zero flow, the plane decreased considerably and the radiation changed to a bluish-white color. The discharge was stable with zero flow and the test was terminated after 5 minutes at this condition. Inspection of the arc-jet after this test revealed a coating of tungsten on the nozzle surface. The tungsten cathode was visibly eroded and had a reduction in weight of 0.863 g. Assuming no weight loss before the zero flow condition the tungsten flow rate was 0.0029 g/sec.

The MPD arc-jet performance data are considered preliminary as a result of the large tare force encountered between the vacuum chamber and the applied magnetic field. (Appendix A)

4 Nozzle exit plane measurements

Measurement of the properties of the exhaust stream at the nozzle exit plane of the arc-jet will allow a determination of the magnitude of power losses in the conversion of electrical to kinetic thrust power. Knowledge of the exit plane flow properties should also provide qualitative information reflecting the flow phenomena in the arc chamber region.

Table 4.1 summarizes the measurements of mass flux, impact pressure, stagnation enthalpy, velocity, and excitation temperature made near the nozzle exit plane (approximately 0.015 to 0.040 inches downstream) on the regeneratively-cooled (GSC–2) arc-jet and the water-cooled (MAC–4, MAC–5) arc-jet. Estimates of the electron concentration were obtained on the water-cooled (MAC–7) arc-jet.

The measurements were taken on the regeneratively-cooled arc-jet at an operating condition of 30 kW power input and a flow rate of 7.35×10^{-4} lb/sec. Twelve operating conditions were selected for the water-cooled arc-jet measurements which consisted of power inputs of 20, 25, 30 and 35 kW at hydrogen flow rates of 3.6×10^{-4}, 4.0×10^{-4}, and 4.5×10^{-4} lb/sec.

4.1 Mass flux profiles

The mass flux profile measurements were obtained with a water-cooled mass flux probe. The

Table 4.1 Nominal arc-jet operating conditions for exit plane exhaust measurements

Arc-jet	GSC–2	MAC–4, MAC–5, MAC–7											
Hydrogen mass flow rate (lb/sec)	7.35×10^{-4}	3.6×10^{-4}				4.0×10^{-4}				4.5×10^{-4}			
Power input (kW)	30	20	25	30	35	20	25	30	35	20	25	30	35
Arc current (amps)	141	144	183	222	261	139	176	215	254	133	169	206	245
Arc voltage	212	139	136	135	134	144	142	139	138	150	148	145	143
Arc chamber pressure (torr)	960	270	285	296	306	296	312	325	335	320	337	353	365
Thrust (lb)	0.713	0.285	0.321	0.347	0.369	0.294	0.330	0.359	0.381	0.320	0.353	0.378	0.401
Specific impulse (sec)	970	810	895	980	1040	760	845	925	990	700	775	840	900
Thrust efficiency (%)	52.6	25.5	25.3	24.9	24.5	23.6	23.5	23.3	23.1	24.1	23.8	23.4	22.8

probe design, associated apparatus, and technique of operation are described in Appendix B. Basically, the probe is a device having a normal shock inlet which allows a sample of the stream to be captured. The mass flux is then the mass flow rate captured by the probe divided by the probe inlet area. Figure 4.1 shows the mass flux probe at the exit plane of the MAC–4 arc-jet exhaust.

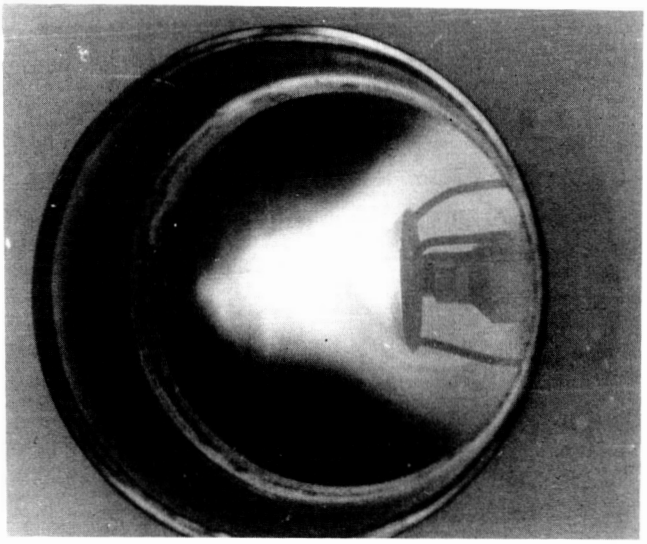

Fig. 4.1 Mass flux probe at exit plane of MAC–4 arc-jet

Mass flux measurements on MAC–4 arc-jet

Figures 4.2 through 4.5 show the mass flux profiles measured at a distance of 0.020 inches (downstream) from the nozzle exit plane of the MAC–4 water-cooled arc-jet. The measurements were taken over the twelve operating conditions selected for this arc-jet.

All the profiles exhibit a "dip" at the exhaust centerline which becomes more pronounced as the flow rate is increased. Figure 4.6 is plot of the mass flux profiles at a constant total mass flow rate of 3.6×10^{-4} for the 20 and 30 kW power levels. As shown the effect of power level on the profile is slight and produces no change of the centerline value. This comparison is typical of all the flow rates and power levels tested.

The integration of the mass flux profiles over the nozzle exit plane should equal the total mass flow through the arc-jet thrustor. Assuming cylindrical symmetry:

$$\dot{m} = 2\pi \int_{o}^{r_o} \rho u r \, dr \qquad (3)$$

where $\dot{m}$ = mass flow rate

ρu = local mass flux

r_o = nozzle exit radius

The integration was obtained graphically by plotting ρu versus r2. The integral thus becomes

$$\dot{m} = \pi \int_{o}^{r_o^2} \rho \, u \, d(r2) \qquad (4)$$

and the total mass flow equals the area under the curve multiplied by π. Table 4.2 presents the comparison of the integrated mass flux profiles with the metered mass flow rate to the arc-jet. The metered mass flow rate was measured with a sonic nozzle flowmeter located in the propellant inlet line.

Integration of the mass flux profiles resulted in 80 to 90 percent agreement with the metered flow rate for all of the conditions tested, with the integrated flow rate lower than the metered. The percentage agreement increases with increasing flow rate and except for the two profiles obtained with the larger inlet diameter, the agreement is better at the higher power levels.

It is expected that the integrated flow rate would be less than the metered flow rate due to nozzle boundary layer effects. In the boundary layer, which is estimated to be relatively thick (approximately 0.2 to 0.4 inches) the flow may be subsonic thus causing the probe measurements in this region to be low since the incoming flow is deflected away from the probe inlet. The results of profile integration suggest that this is the case since the percentage agreement increases as the energy and density of the stream is raised.

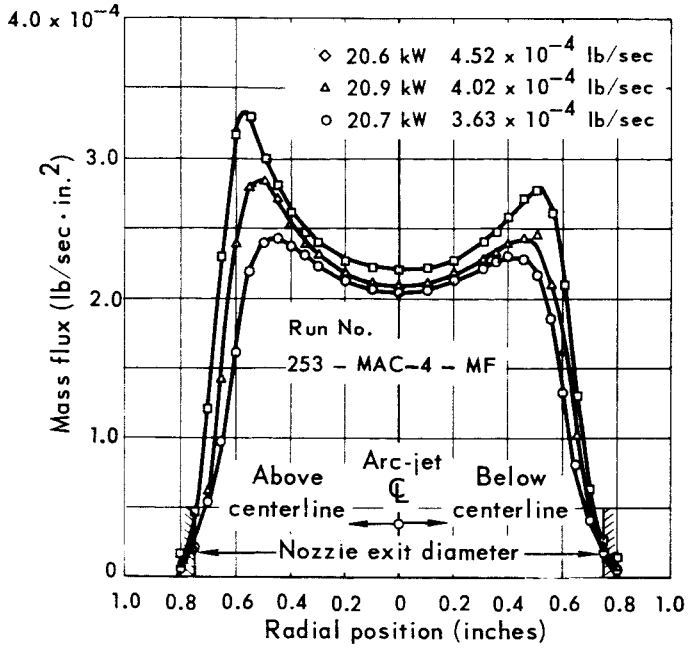

Fig. 4.2 Mass flux profiles on MAC–4 water-cooled arc-jet

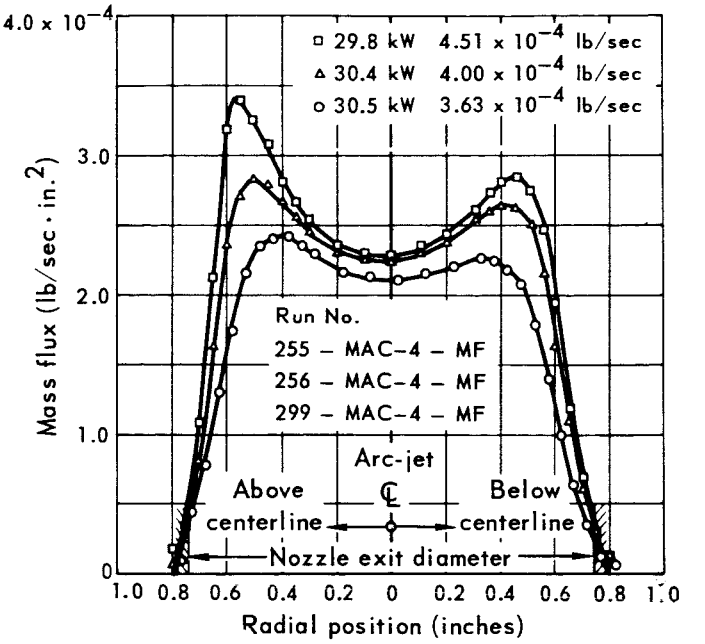

Fig. 4.4 Mass flux profiles on MAC–4 water-cooled arc-jet

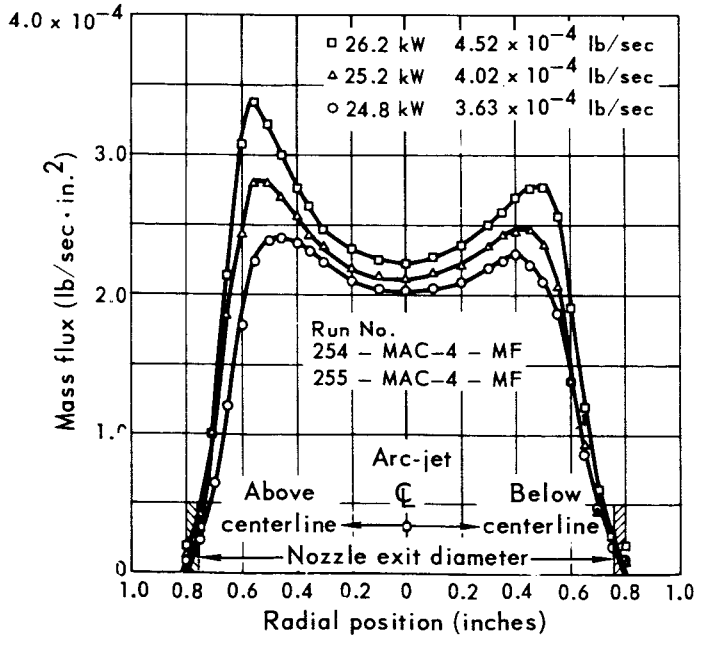

Fig. 4.3 Mass flux profiles on MAC–4 water-cooled arc-jet

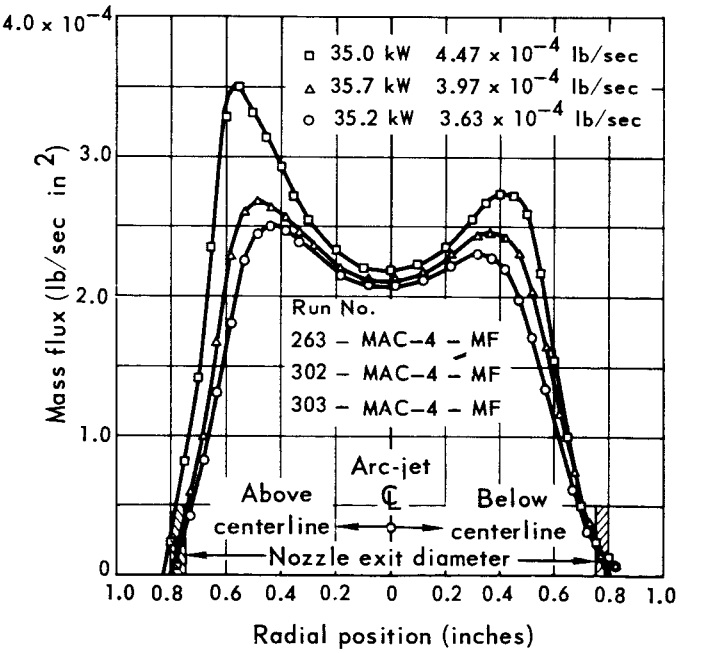

Fig. 4.5 Mass flux profiles on MAC–4 water-cooled arc-jet

Table 4.2 Mass flow rate comparisons on MAC –4 arc-jet

Power input (kW)	Metered mass flow rates (lb/sec)	Integrated mass flow rate (lb/sec)	$\frac{\text{Integrated flow rate}}{\text{Metered flow rate}} \times 100$ (percent)
20.7	3.63×10^{-4}	2.93×10^{-4}	80.7
24.8	3.63×10^{-4}	3.01×10^{-4}	83.0
30.5	3.63×10^{-4}	3.02×10^{-4}	83.2
35.2*	3.63×10^{-4}	2.82×10^{-4}	77.7
20.9	4.02×10^{-4}	3.31×10^{-4}	82.4
25.2	4.02×10^{-4}	3.44×10^{-4}	85.6
30.4	4.00×10^{-4}	3.55×10^{-4}	88.4
35.7*	3.97×10^{-4}	3.31×10^{-4}	83.5
20.6	4.52×10^{-4}	3.92×10^{-4}	86.7
26.1	4.52×10^{-4}	3.92×10^{-4}	86.7
29.8	4.51×10^{-4}	3.97×10^{-4}	88.0
35.0	4.45×10^{-4}	3.99×10^{-4}	89.2

*Probe inlet diameter increased from 0.068 inches to 0.108 inches

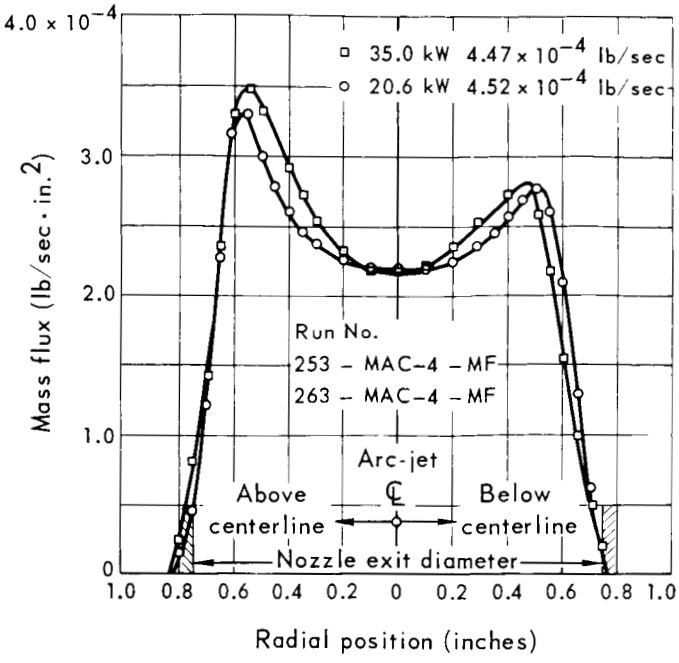

Fig. 4.6 Effect of power on mass flux profiles (MAC–4 water-cooled arc-jet)

Both of these effects should reduce the nozzle boundary layer thickness.

Incomplete capture of the normal shock at the probe lip could account for the difference between integrated and metered flow rates; however, visual observation of the bow shock at the probe lip suggest that the shock was indeed swallowed. Whenever the probe was located within a radius of approximately 0.4 inches the bow shock before sample collection was observed to stand off from the lip approximately 0.030 to 0.50 inches. Upon initiation of the collection, the bow shock moved towards the probe and attached to the probe lip.

For the purpose of calculations and comparison checks which involve the mass flux profile, it is necessary that the measured profile be adjusted to be equal the metered mass flow rate. Figure 4.7 is a typical mass flux profile which was constructed for the purpose of computations presented in the remainder of this report. Also shown in Fig. 4.7 is the measured profile. In the construction it is assumed that the mass flux values measured within a radius of 0.4 inches are quantitatively correct and so the two profiles agree in this region. However, the values at radii greater than 0.4 inches were adjusted in a manner consistent with the experimental measurements to a level where the integrated and metered flow rates were in 100 percent agreement. This construction is necessarily subjective in nature, however, it is felt that

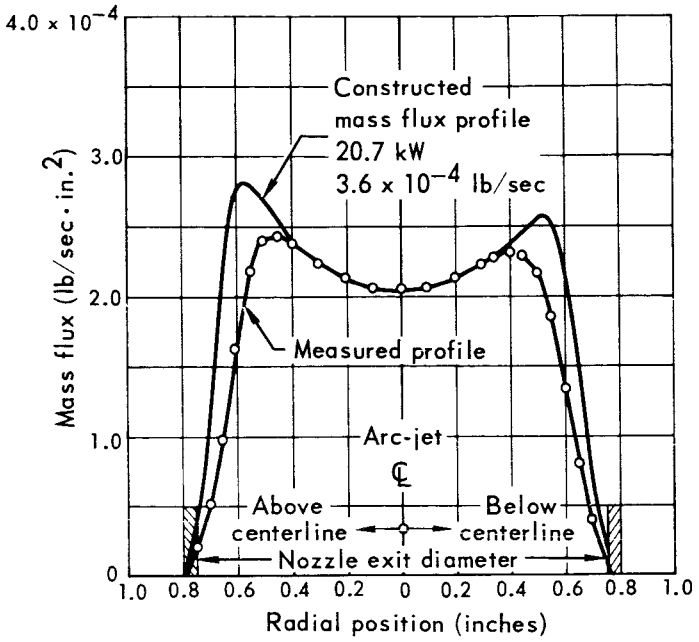

Fig. 4.7 Constructed mass flux profile on MAC–4 water-cooled arc-jet

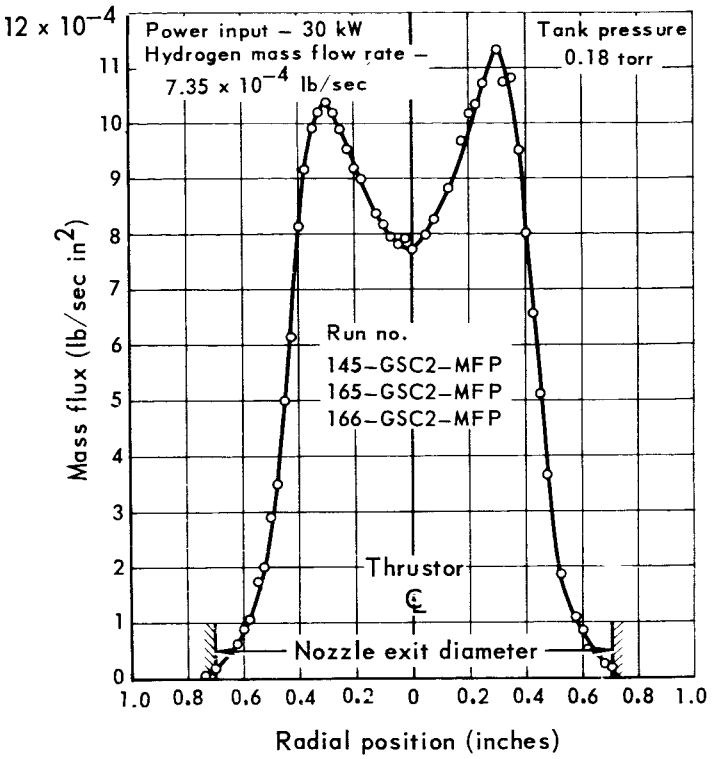

Fig. 4.8 Mass flux profile on GSC–2 regeneratively cooled arc-jet

any possible errors resulting from this construction will be minimal.

The constructed mass flux profiles were used in the derivation of the velocity profiles (Sec. 4.3), total power flux (Sec. 4.4), kinetic power flux (Sec. 5.2), and the thermal power flux (Sec. 5.4).

Mass flux measurements on GSC–2 arc-jet

Figure 4.8 is the mass flux profile measured approximately 0.020 inches downstream from the exit plane of the GSC–2 arc-jet.
The data is a summary of two traverses of the mass flux probe across the nozzle exit diameter. The power input for these tests was 30.5 kW and the hydrogen mass flow rate was 7.35 x 10^{-4} lb/sec.

The profile is slightly asymmetric as were the MAC–4 arc-jet measurements and also possesses a "dip" at the arc-jet exhaust centerline. Each half of this profile was integrated across the exit plane area and then averaged, resulting in 97% of the metered flow rate. The good agreement between integrated and metered flow rates is most likely due to the higher mass flow rate at which this thrustor was operated, and the higher wall temperature which results in a smaller nozzle boundary layer than for a water-cooled nozzle.

4.2 *Impact pressure profiles*

A measurement of the impact pressure of a high Mach number gas flow is approximately equal to the momentum flux of the stream. A water-cooled impact probe was used to obtain impact pressure profiles at the exit plane of the water-cooled MAC–4 and GSC–2 arc-jets. The probe design, associated apparatus, and technique of operation are described in Appendix C.

Impact pressure measurements on arc-jets

Figure 4.9 presents the initial impact pressure profiles measured on the MAC–4 arc-jet. These measurements were the first taken after fabrication of this arc-jet. As shown in Fig. 4.9, the profile at 20.9 kW exhibits a "blip" above the arc-jet centerline. On close examination of the arc-jet a small burr was found on one of the tangential propellant inlets. Figures 4.10 through 4.12 shows the impact pressure profiles obtained after removal of the burr for propellant flow rates ranging from 3.6×10^{-4} to 4.5×10^{-4} lb/sec and power inputs ranging from 20 to 40 kW. It can be seen that the profile symmetry was improved with the removal of the small burr. This suggests that the machining quality and alignment of the tangential injection ports can significantly affect the pressure profile.

Inspection of the profiles of Fig. 4.10 to 4.12 indicates the impact pressure distribution becomes more symmetrical as the flow rate and input power are increased. To determine if the asymmetry was due to a particular orientation of the arc-jet, the arc-jet was rotated 180 degrees about its centerline and profile measurements were taken. Data obtained on this test represented a mirror image of the data shown in Figs. 4.10 to 4.12, thus indicating the asymmetry is a thrustor configuration characteristic and not due to its orientation within the test chamber.

Each of the MAC–4 profiles possess a distinct change in slope at a radius of ± 0.60 inches. It is felt that the change in slope is a probe effect since the outer radius of the probe tip is very close to the nozzle wall at this position and as such corners the flow in front of the probe.

Impact pressure profiles were also obtained on the MAC–5 water-cooled arc-jet and were within $\pm 1\%$ of the data obtained on the MAC–4.

A check of the impact pressure profile measurements can be obtained by a comparison with the arc-jet thrust measurement. The arc-jet thrust, assuming cylindrical symmetry is given by,

$$T = 2\pi \int_{o}^{r_o} (\rho u^2 + p_s - p_a)\, r\, dr \qquad (5)$$

where T = thrust

ρu^2 = momentum flux

p_s = static pressure at nozzle exit

p_a = ambient tank pressure.

Since the impact pressure $p_i = \rho u^2$, and assuming p_s is small then

$$T = 2\pi \int_{o}^{r_o} (p_i - p_a)\, r\, dr \qquad (6)$$

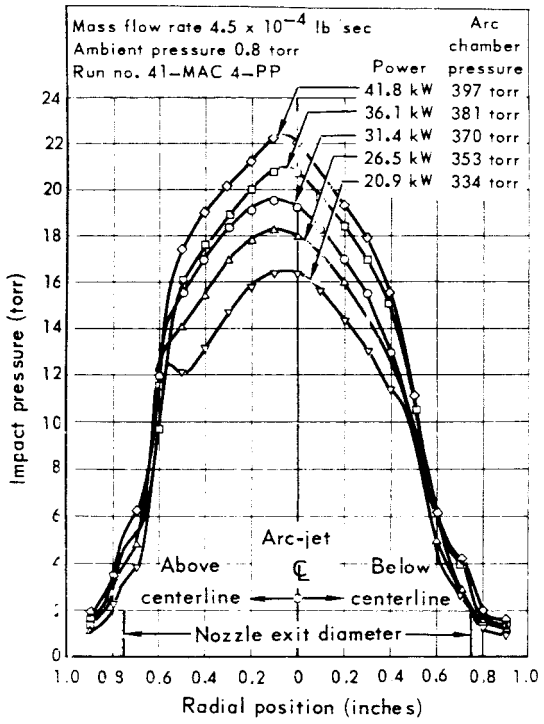

Fig. 4.9 Initial impact pressure profiles on MAC–4 water-cooled arc-jet

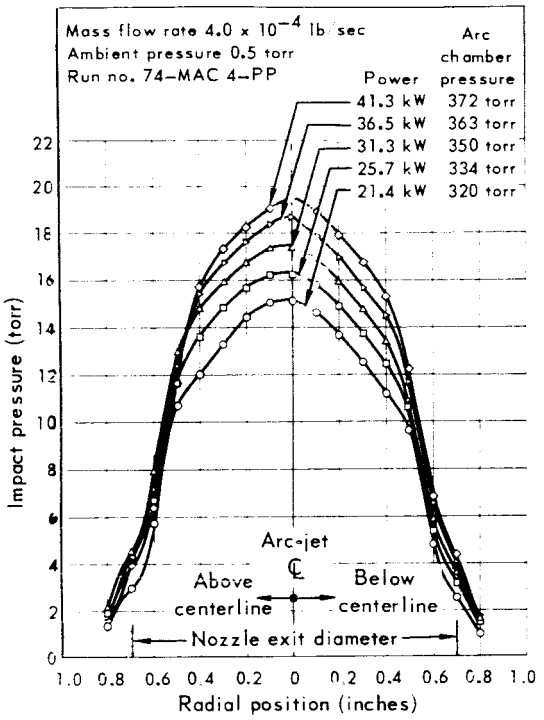

Fig. 4.11 Impact pressure profiles on MAC–4 water-cooled arc-jet

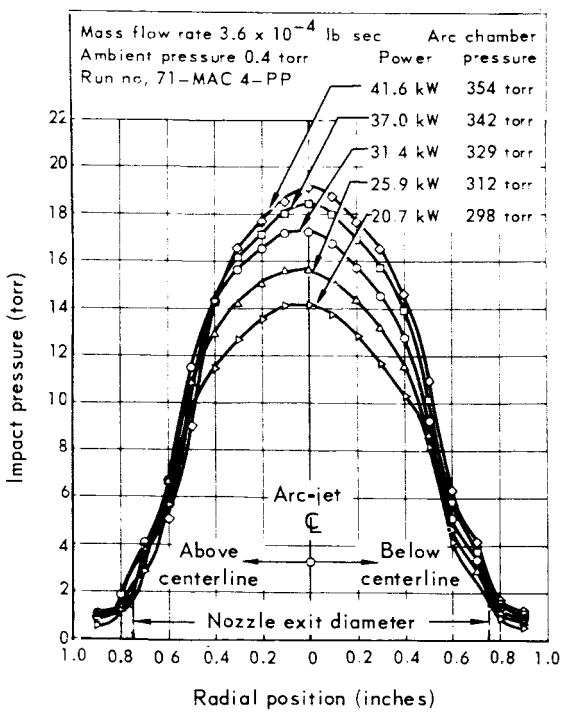

Fig. 4.10 Impact pressure profiles on MAC–4 water-cooled arc-jet

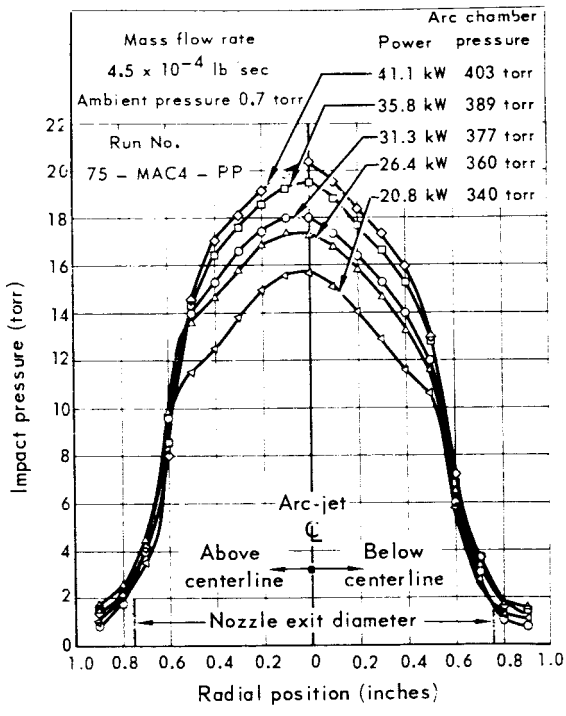

Fig. 4.12 Impact pressure profiles on MAC–4 water-cooled arc-jet

The ambient tank pressure was measured at each of the operating conditions at which profile measurements were obtained and was used in the integration of the profiles presented in Figs. 4.9 to 4.12. The results of the integration are shown in Figs. 4.13 through 4.15. In addition to the integrated thrust values the MAC–5 arc-jet thrust performance is plotted as a function of power input.

The thrust values obtained from the impact pressure profiles are generally lower than the measured thrust. This is expected since the impact pressure is only an approximate value of the momentum flux and the static pressure was neglected in the integration. The one exception is a data point on Fig. 4.15. The greatest deviation of the integrated value from the measured thrust occurs at the higher power levels and lower flow rates. One point deviates by 12% and all others deviate by less than 9%.

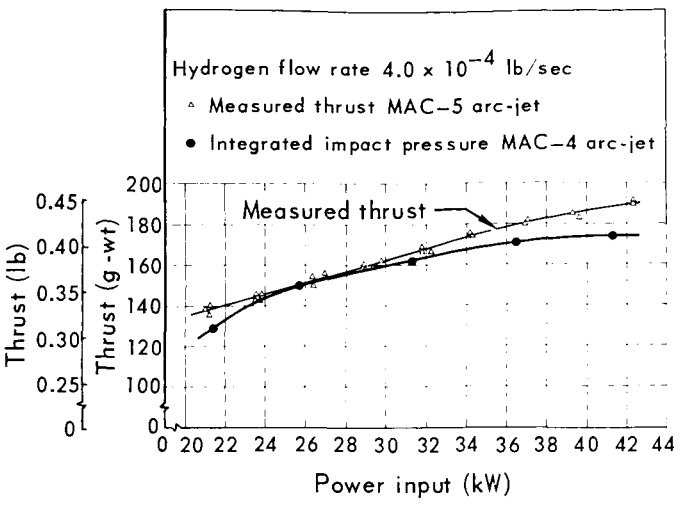

Fig. 4.14 Comparison of integrated impact pressure with measured thrust

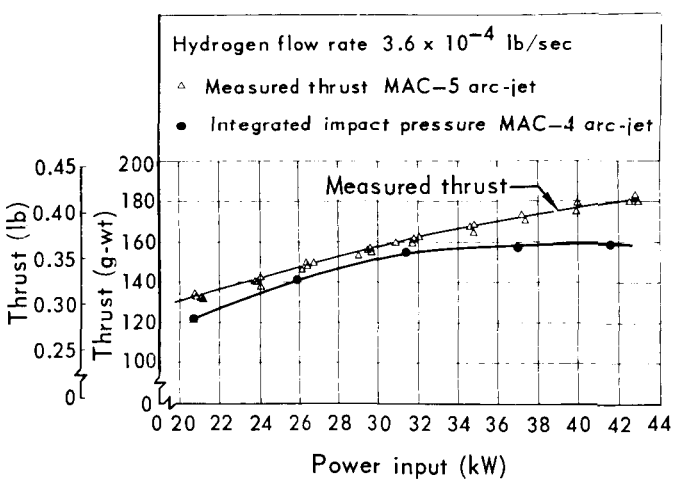

Fig. 4.13 Comparison of integrated impact pressure with measured thrust

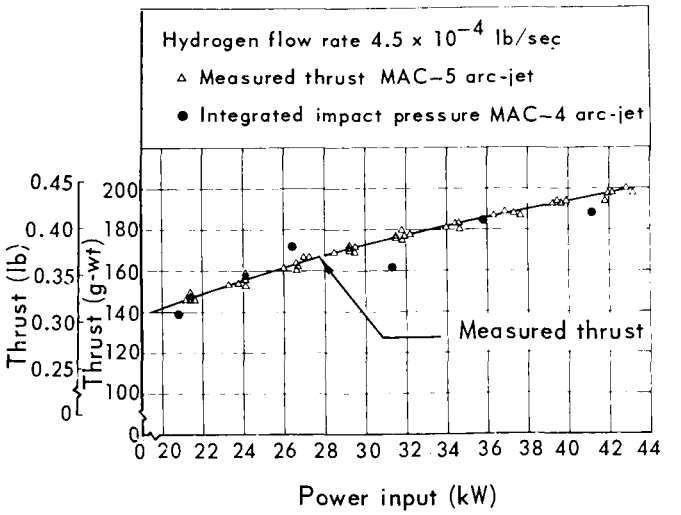

Fig. 4.15 Comparison of integrated impact pressure with measured thrust

Impact pressure measurements on regeneratively-cooled GSC–2 arc-jet

An impact pressure profile was measured at the exit plane of the GSC–2 arc-jet operating at a nominal specific impulse of 1000 sec. During this test the impact pressure probe was positioned approximately 0.020 inches downstream of the nozzle exit. The arc-jet was operated at a power input of 30.3 kW and a hydrogen mass flow rate of 7.4×10^{-4} lb/sec.

Figure 4.16 shows the profile obtained during this test. The impact pressure profile exhibits the "dip" at the arc-jet centerline which was also observed in the mass flux measurements and is in contrast to the MAC–4 profiles which peaked on centerline. This profile was integrated over the exit plane area and resulted in a thrust value of 0.66 lb.

The measured thrust value was 0.713 lb at this operating condition. The agreement between thrust levels is 92.6%.

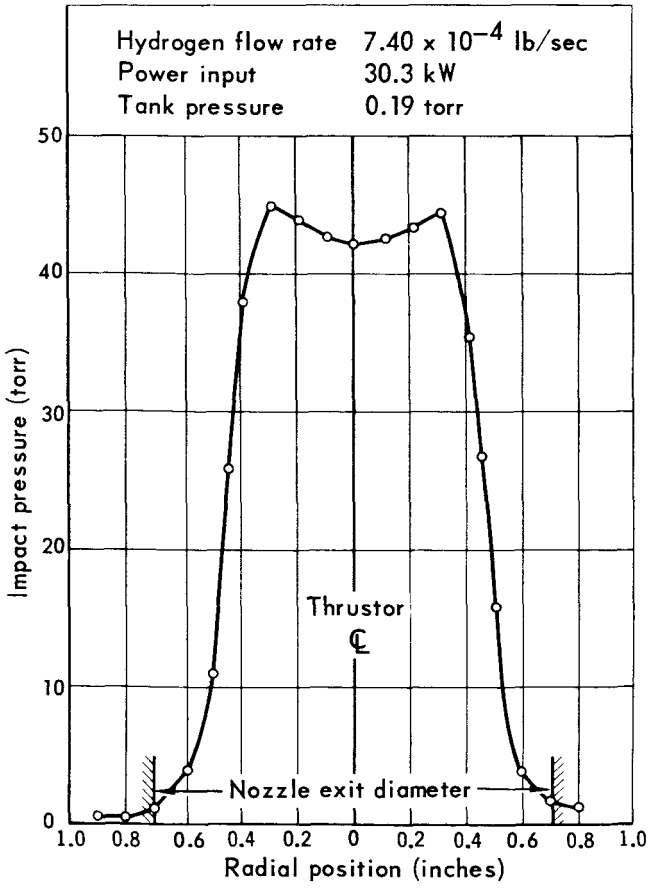

Fig. 4.16 Impact pressure profile for GSC–2 thrustor

4.3 *Velocity profiles*

Two techniques of determining the exit plane velocity profiles were employed in this experimental program. One technique utilized the dual photocell velocity meter described in Appendix D to provide a direct measurement of the exhaust velocity. The other technique made use of the mass flux and impact pressure measurements obtained with the water-cooled probes described in Appendices B and C.

The impact pressure and mass flux measurements can be combined to give a velocity profile. Since for high Mach number flows the impact pressure is approximately equal to the momentum flux ρu^2, where ρ is the gas density and u is the gas velocity, and the mass flux is ρu, a division of the local impact pressure by the local mass flux will give the local velocity, u. If the pressure is in (torr) and the mass flux is given in (lb/sec in.^{2}) the velocity (ft/sec) is obtained by the following equation:

$$u = 0.623 \frac{p_i}{\rho u} \qquad (7)$$

where p_i = impact pressure (torr).

All data obtained with the velocity meter were within 20% agreement with the data obtained with the probes. The largest deviation occurred at the jet centerline where the velocity meter records an "average" across the viewing diameter and not the local velocity. A comparison of the velocity profile obtained with the velocity meter and the probes is presented in Appendix D.

Analysis of the results indicated that the velocity meter recorded the exhaust velocity for the MAC–4 arc-jet and for the GSC–2 arc-jet, the exhaust velocity plus the local sonic speed.

While the velocity profiles, deduced from the probe measurements possess a higher degree of accuracy for the mass flow rate and enthalpy ranges tested in this program, it is anticipated that the velocity meter technique will be more applicable in the very high enthalpy arc-jet operation region where heat transfer considerations would prevent probe measurement. The velocity measurements presented below were obtained from the probe measurements.

Referring to the electrical characteristics of this arc-jet (Fig. 3.17) it is seen that power increases at constant mass flow rate are effected mainly by arc current increases since the arc voltage curve is relatively flat. It is also noted that increasing the mass flow rate at constant power reduces the arc current. Thus, it appears that velocity distribution at the nozzle exit plane is most sensitive to changes in the arc current level.

The extrapolation of the velocity profiles to the nozzle exit diameter was made in a somewhat arbitrary manner so that estimates of the kinetic power flux could be calculated. No attempt was made to define the velocity profile in the boundary layer near the nozzle wall.

Velocity measurements on MAC–4 arc-jet

Figures 4.17 through 4.19 present the velocity profiles calculated by Eq. (5) for the MAC–4 arc-jet at the 12 operating conditions of this thrustor. The profiles all peak on or very near the exhaust centerline and decrease rapidly away from the centerline. Further, all the profiles tend to converge to a common velocity at a radial position between 0.40 and 0.50 inches. The effect of power increases for a constant mass flow is quite evident and results in a more sharply peaked velocity distribution over the central region of ± 0.4 inches radius.

Inspection of the profiles at constant power and varying mass flow rate reveals a slight but not significant change in the velocity distribution.

Velocity measurements on GSC–2 arc-jet

The velocity profile as calculated from the impact pressure and mass flux measurements taken on the GSC–2 arc-jet is presented in Fig. 4.20. The data are less peaked than the profiles obtained on the water-cooled arc-jet and are lower in magnitude. Although the velocities are lower in this jet, it is noted that approximately 80% of the mass is within a radius of ±0.5 inches while on the water-cooled arc-jet only 40 to 50% is in the high velocity arc region, which is reflected in the higher thrust efficiency of the GSC–2 arc-jet.

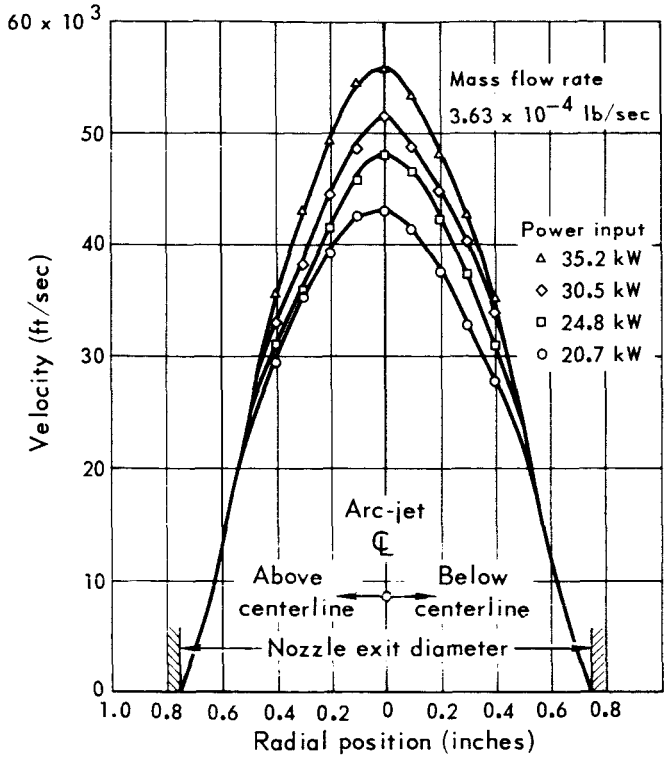

Fig. 4.17 Velocity profiles on MAC–4 water-cooled arc-jet

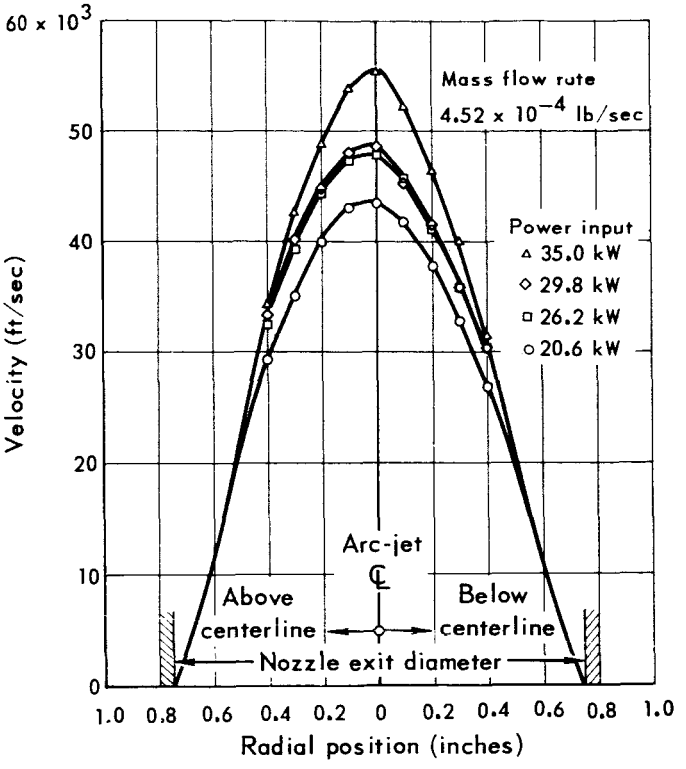

Fig. 4.19 Velocity profiles on MAC–4 water-cooled arc-jet

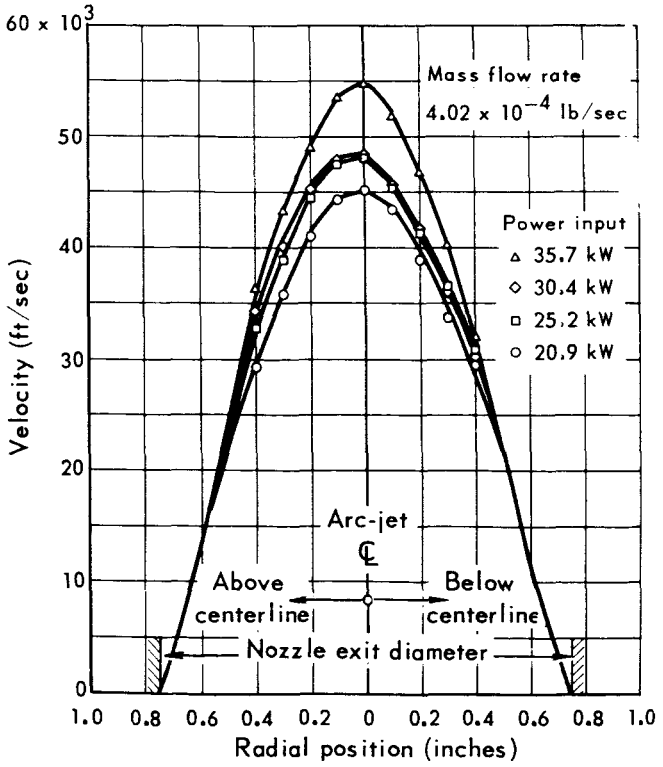

Fig. 4.18 Velocity profiles on MAC–4 water-cooled arc-jet

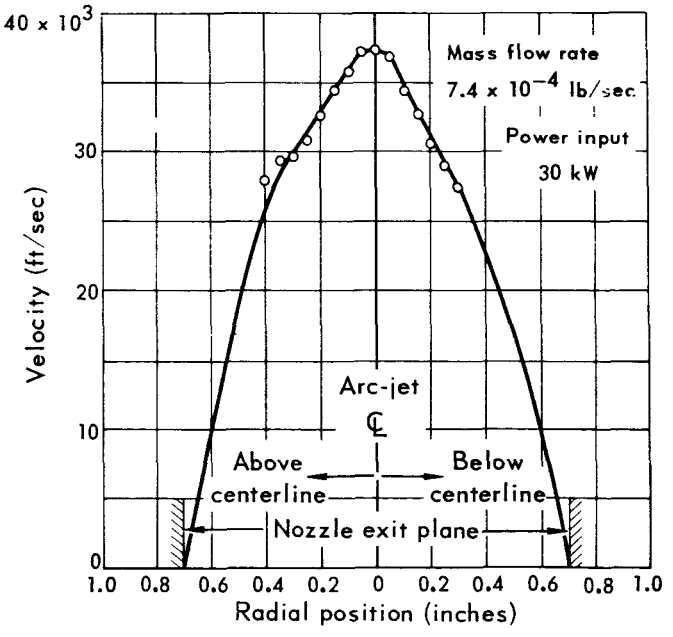

Fig. 4.20 Velocity profile on GSC–2 regeneratively cooled arc-jet

4.4 *Stagnation enthalpy profiles*

The stagnation enthalpy measurements were obtained with a water-cooled total enthalpy probe described in Appendix E. This probe is a calorimetric device which collects a sample of the exhaust stream, extracts its energy content by means of a heat exchanger, and exhausts the cooled sample through a sonic flow nozzle. Measurements of the cooling water flow rate and temperature rise allow a determination of the power extracted within the probe, and measurements of the gas temperature and pressure upstream of the sonic flow nozzle determine the mass flow rate of gas collected by the probe. These measurements are sufficient to define the total energy content or enthalpy of the collected sample.

Figure 4.21 is a photograph of the stagnation enthalpy probe located at the exit plane of the MAC–5 arc–jet operating on hydrogen at 20 kW.

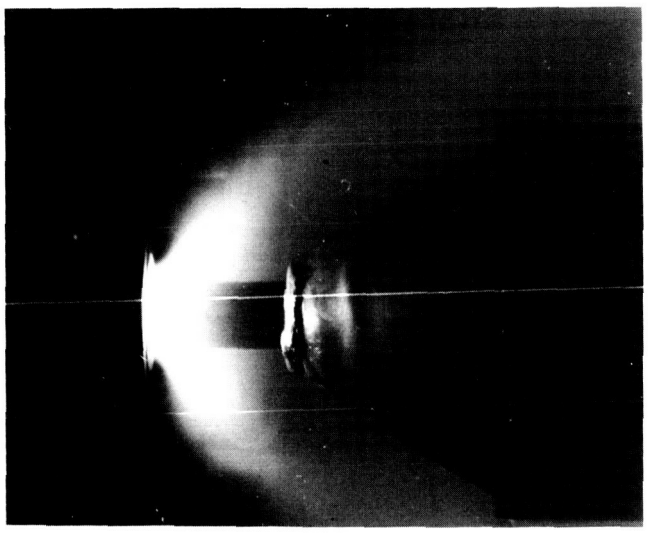

Fig. 4.21 Stagnation enthalpy probe in exhaust of MAC–5 arc-jet

Stagnation enthalpy measurements on MAC–5 arc-jet

Figures 4.22 through 4.24 show the stagnation enthalpy profiles measured at a distance of 0.030 inches (downstream) of the exit plane of the MAC–5 arc-jet. Inspection of the probe after the test at the highest enthalpy condition (35 kW – 3.6 x 10^{-4} lb/sec) revealed that the probe lip of the external shield had eroded slightly leaving a small area of

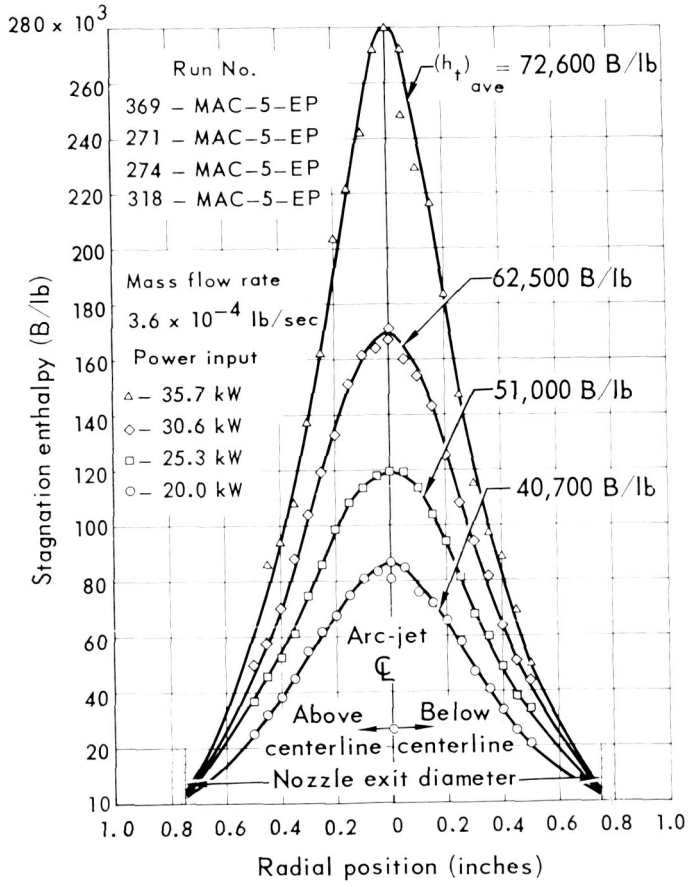

Fig. 4.22 Stagnation enthalpy profiles on MAC–5 water-cooled arc-jet

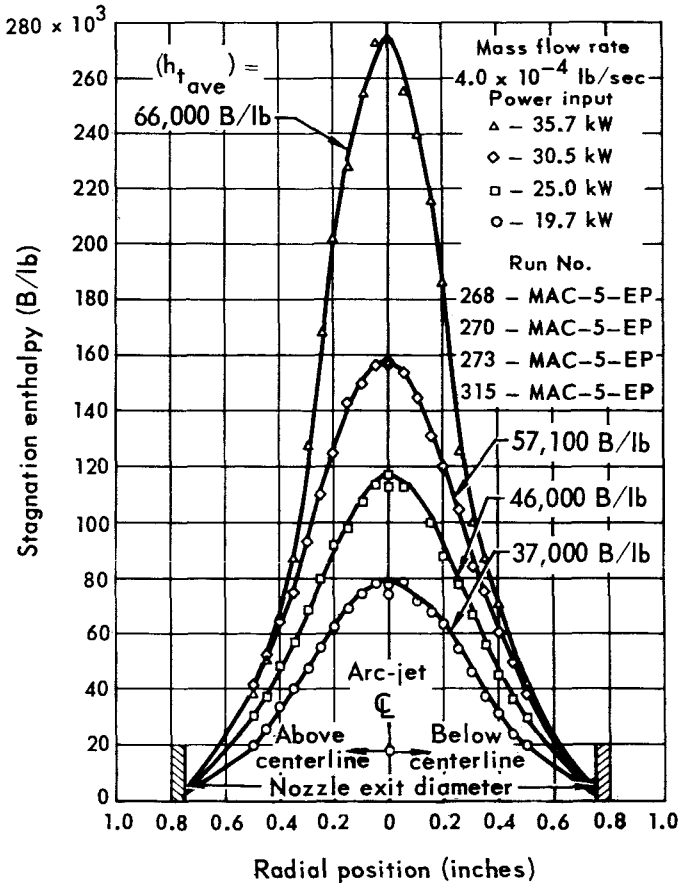

Fig. 4.23 Stagnation enthalpy profiles on MAC–5 water-cooled arc-jet

the internal probe lip exposed to the external exhaust flow. Figure 4.25 shows probe after the above test in which the normally enclosed internal lip is clearly visible. Thus, it is expected that the enthalpy values are slightly high for this operating condition.

The enthalpy profiles all peak on the jet centerline and are relatively symmetric about the centerline. The effect of raising the input-power is quite evident and results in an increase in enthalpy over the whole profile with the largest increase on the jet centerline.

The ratio of centerline enthalpy to the bulk exit enthalpy ranged between 2.1 to 4.1 for all tests. No functional relationship was detected, however, the ratio generally increased with increasing bulk exit enthalpy.

The extrapolation of the enthalpy data from a radius of 0.5 inches to the nozzle was made assuming the gas temperature at the wall was near 500°K and has an enthalpy of 3,000 B/lb.

Power flux profiles (MAC–4)

The stagnation enthalpy profile data were multiplied by the corresponding local mass flux values described in Section 4.1. The result of these calculations are presented in Figs. 4.26 through 4.28 and as such represent the total power flux profiles for the MAC–5 arc-jet. As shown, the power flux profiles have the same characteristic shape of the total enthalpy profiles.

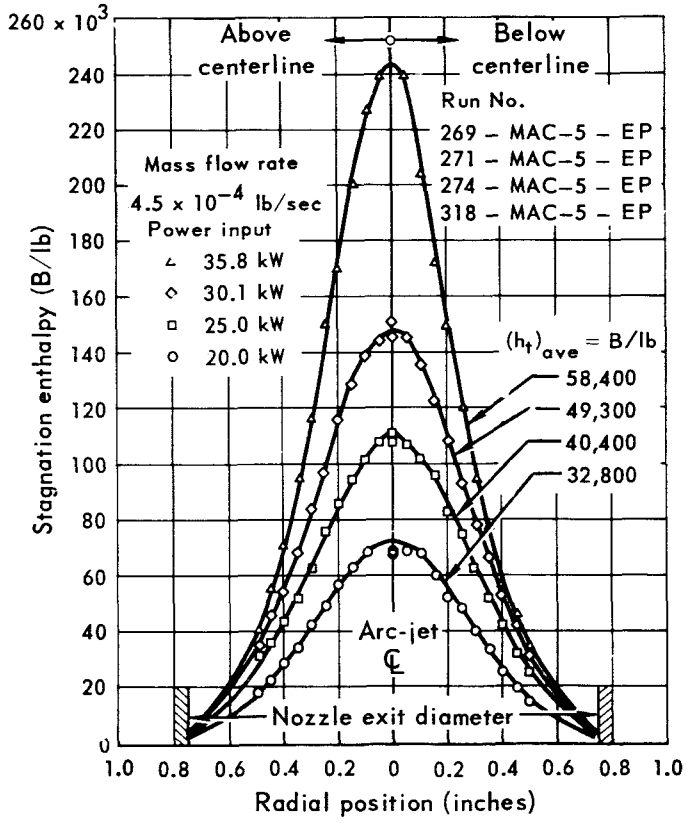

Fig. 4.24 Stagnation enthalpy profiles on MAC–5 water-cooled arc-jet

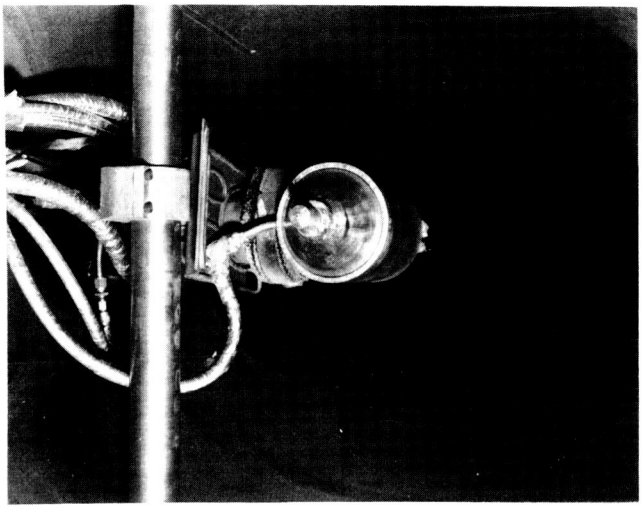

Fig. 4.25 Stagnation enthalpy probe lip after highest enthalpy test

The total power flux profiles can be integrated over the nozzle exit plane area and should satisfy the following relation, assuming cylindrical symmetry:

$$P_{in} - P_{loss} = 2\pi \int_{o}^{r_o} h_t \, \rho u \, r \, dr \qquad (8)$$

where P_{in} = power input

P_{loss} = power losses due to radiation and heat transfer to the nozzle wall

h_t = measured local stagnation enthalpy

ρu = local mass flux

r_o = nozzle exit radius

The profiles of Figs. 4.26 through 4.28 were graphically integrated over the nozzle exit plane area and the results are presented in Table 4.3.

The integrated exhaust power values are lower than the measured power input to the gas for all conditions except the 35 kW, 3.6 x 10^{-4} lb/sec condition during which the erosion of the probe lip (previously noted) occurred.

In light of the manner of obtaining the total power in the gas, (i.e. assumed cylindrical symmetry, extrapolation of the enthalpy profiles, constructed

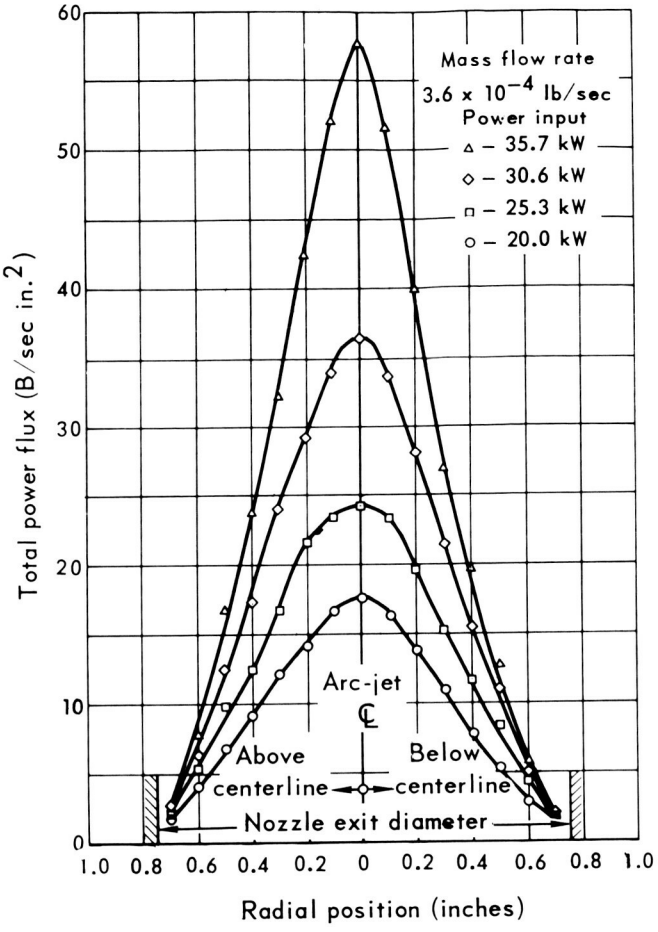

Fig. 4.26 Total power flux profiles on MAC–5 water-cooled arc-jet

mass flux values at the outer regions of the exhaust) the agreement between the two power measurements is considered quite satisfactory. The trend of better agreement as the power is increased is presently being investigated for possible systematic errors.

Stagnation enthalpy measurements on the GSC–2 arc-jet

Figure 4.29 depicts the stagnation enthalpy profile obtained on the GSC–2 arc-jet at a location of 0.010 inches from the exit plane. The GSC–2 arc-jet was operated at a power input of 30.6 kW and a hy-

drogen mass flow rate of 7.35 x 10^{-4} lb/sec. The profile is symmetrical and is peaked on the exhaust centerline at 72,800 B/lb. Some data scatter is observed at radii greater than 0.45 inches. This might be expected since the small flow rates and small temperature differentials encountered in this region, may cause large experimental errors. This region (radii greater than 0.5 inches) was not probed on the MAC–5 arc-jet tests described above due to the large scatter encountered. A smooth curve was drawn through the data and extrapolated to the nozzle wall which was assumed to be at 1500°K. The data of Fig. 4.29 were multiplied by the local mass flux

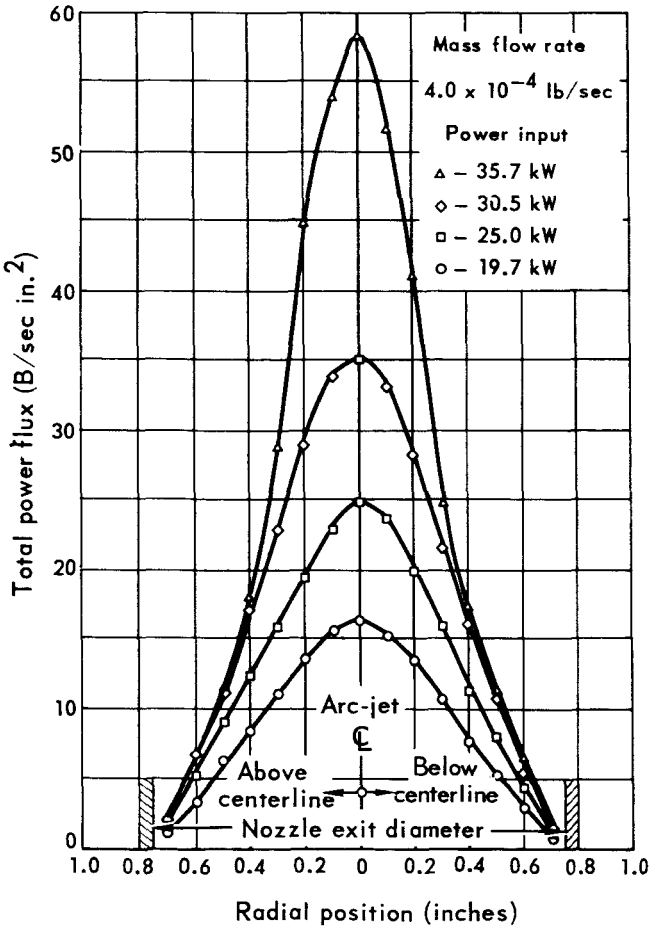

Fig. 4.27 Total power flux profiles on MAC–5 water-cooled arc-jet

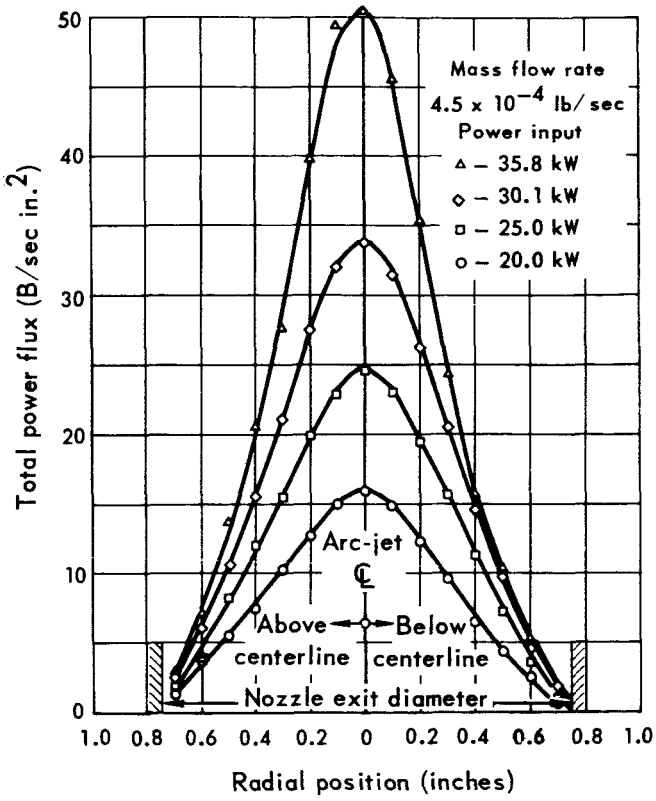

Fig. 4.28 Total power flux profiles on MAC–5 water-cooled arc-jet

at each radial position (Fig. 4.8) and the resulting total power flux profile is shown in Fig. 4.30.

Power flux profiles (GSC–2)

The GSC–2 power flux profile is relatively flat across a diameter of 0.4 inches and again is in contrast to the MAC–5 arc-jet which was strongly peaked on the centerline. The profile of Fig. 4.30 was integrated over the nozzle exit plane and yielded a value of 24.7 kW. The power input was 30.6 kW. Thus, the integrated power in the gas was 80.8% of the total input power. This value is somewhat lower than expected since the radiated power loss is estimated to be near 11% requiring the exhaust power to be approximately 89%. Some of this deviation can be attributed to the mass flux values used since the integrated mass flux profile was 3% lower than the metered flow rate.

Table 4.3 Exhaust power comparisons on MAC–5 arc-jet

Mass flow rate (lb/sec)	Power input (kW)	Power losses (kW)	$P_{in} - P_{loss}$ (kW)	Integrated power flux profile (kW)	$\frac{\text{Integrated power}}{P_{in} - P_{loss}}$ (percent)
3.6×10^{-4}	20.0	4.53	15.5	12.7	82.3
3.6×10^{-4}	25.0	5.66	19.3	17.9	92.7
3.6×10^{-4}	30.6	6.87	23.8	23.8	100.0
3.6×10^{-4}	35.7	8.10	27.6	30.6	111.0*
4.0×10^{-4}	19.7	4.54	15.2	11.2	74.4
4.0×10^{-4}	25.0	5.47	19.4	17.8	91.8
4.0×10^{-4}	30.5	6.35	24.1	23.2	96.2
4.0×10^{-4}	35.7	7.80	27.9	27.2	97.5
4.5×10^{-4}	20.0	4.45	15.6	11.4	74.5
4.5×10^{-4}	25.0	5.81	19.2	16.3	85.0
4.5×10^{-4}	30.1	6.92	23.4	21.3	91.0
4.5×10^{-4}	35.8	8.10	27.7	27.9	100.1

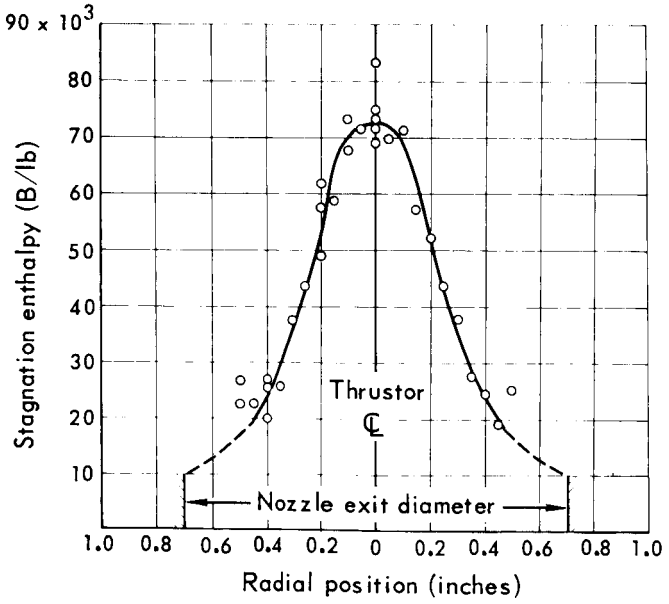

Fig. 4.29 Stagnation enthalpy profile on GSC–2 reregeneratively cooled arc-jet

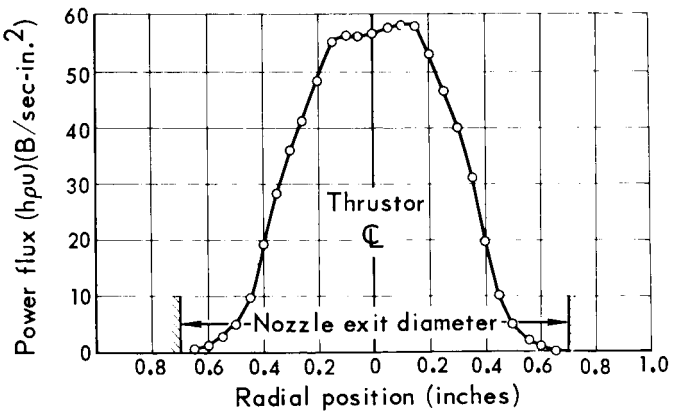

Fig. 4.30 Total power flux profile on GSC–2 regeneratively cooled arc-jet

4.5 Excitation temperature profiles

Excitation temperature profile measurements were obtained at the exit plane of the MAC–5 and GSC–2 arc-jets using a spectrograph and the method of relative line intensities. The theory, experimental apparatus, and technique of operation are described in Appendix F.

For an optically thin plasma in which the excited state population obeys Boltzmann's distribution law, the excitation temperature is related to the spectral line intensities by the equation:

$$\log_{10} \frac{I_{nm} \lambda^3_{nm}}{f_{nm}} = \text{Constant} - \frac{5040}{T} E_n \qquad (9)$$

where I_{nm} = intensity of spectral line
λnm = wavelength of emitted radiation
f_{nm} = absorption oscillator strength
E_n = transition energy between state n and m
T = excitation temperature

Since the quantities I_{nm}, λ_{mn}, f_{nm} are known, a knowledge of the local spectral line intensities at a given radial position in the plasma will allow a determination of the excitation temperature. This is obtained by measuring the slope of the line obtained by plotting $\log_{10} \frac{I_{nm} \lambda^3_{nm}}{f_{nm}}$ versus E_n.

The radial spectral line intensities are obtained from the measured average "side on" intensities through the use of the Abel transformation (See Appendix F).

Excitation temperature measurements on MAC–5 arc-jet

Figures 4.31 through 4.33 present the excitation temperature profiles obtained at the exit plane of the MAC–5 arc-jet. These measurements were made approximately 0.080 inch downstream of the nozzle exit plane. The temperature profiles exhibit considerable data scatter over the operating conditions tested and do not possess a characteristic shape or distribution. The error bars attached to the data points represent the temperatures which could be obtained by drawing the two extreme lines on the Boltzmann plots; that is, the extreme lines that are consistent with the data.

It is felt that the uncertainties in the experimental data do not permit a quantitative determination of the excitation temperature profiles; however, the distributions are all relatively flat and increase as the bulk stagnation enthalpy increases.

It should be noted that the error bars shown do not represent the total error in a given temperature value. The total error should take into account the following sources of error:

- relative line intensity measurement,
- Abel inversion procedure,
- fluctuations in exhaust plasma
- oscillator strengths used in calculations.

Of these four sources of error the last two may be considered negligible since the oscillator strengths have an estimated accuracy of 1% and the measurements were taken over a long period of time with respect to any fluctuation in the plasma.

The error to be expected in the measurement of the relative line intensities is approximately 10 percent. This will produce a corresponding error of approximately 10 percent in the temperatures computed from a Boltzmann plot of these measured quantities, that is the average temperature along a chord of the exit plane cross section. Therefore, the radial temperatures can at best be in error 10 percent.

The amount of error introduced by the Abel inversion procedure is quite difficult to determine since a particular value of the radial intensity depends upon the shape of the curve fitted to all the measured data points. This occurs because of the integration involved in the Abel inversion. In order to construct error bars for the inverted data it would be necessary to determine the curves, consistent

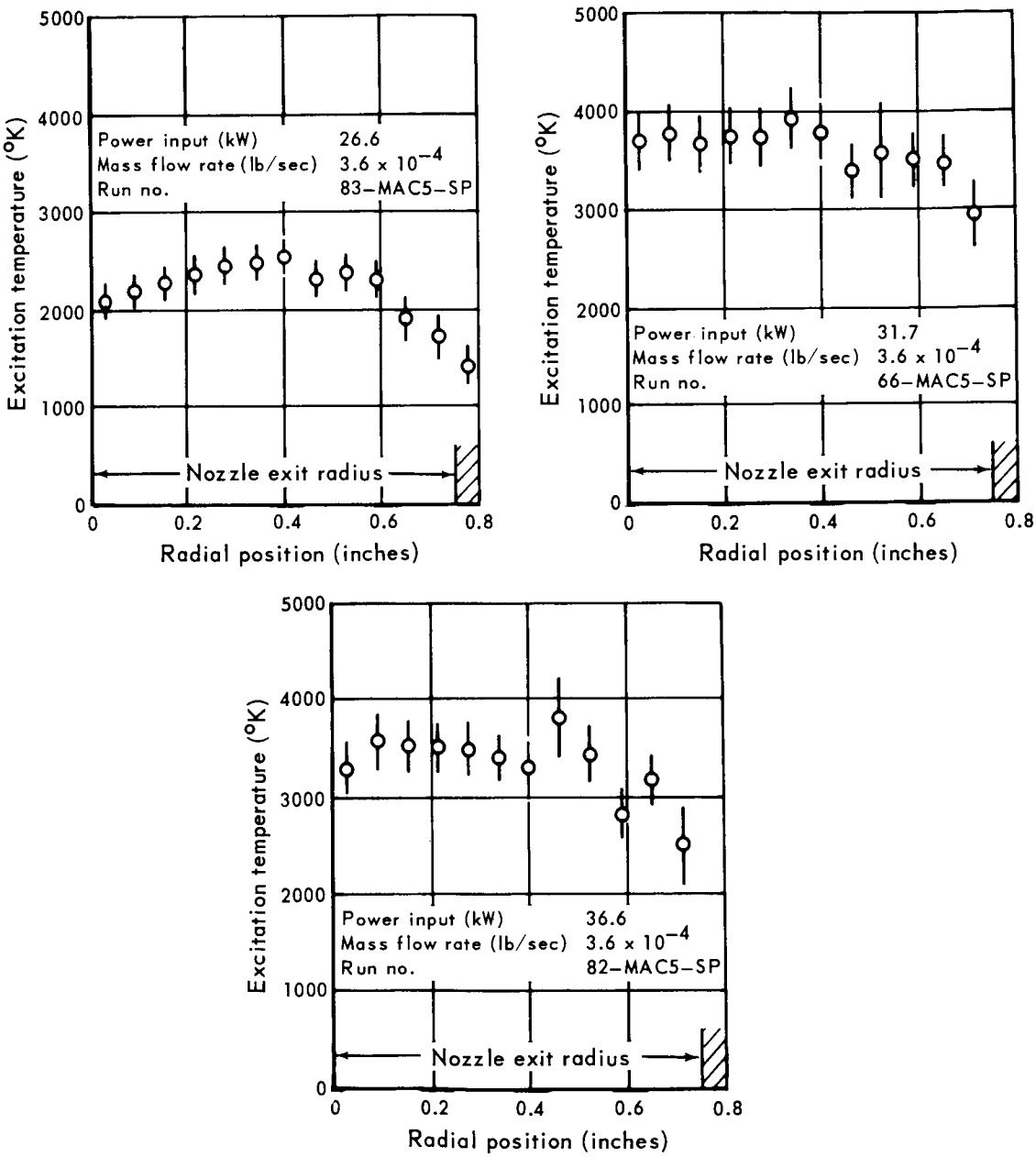

Fig. 4.31 Excitation temperature profiles on MAC–5 water-cooled arc-jet

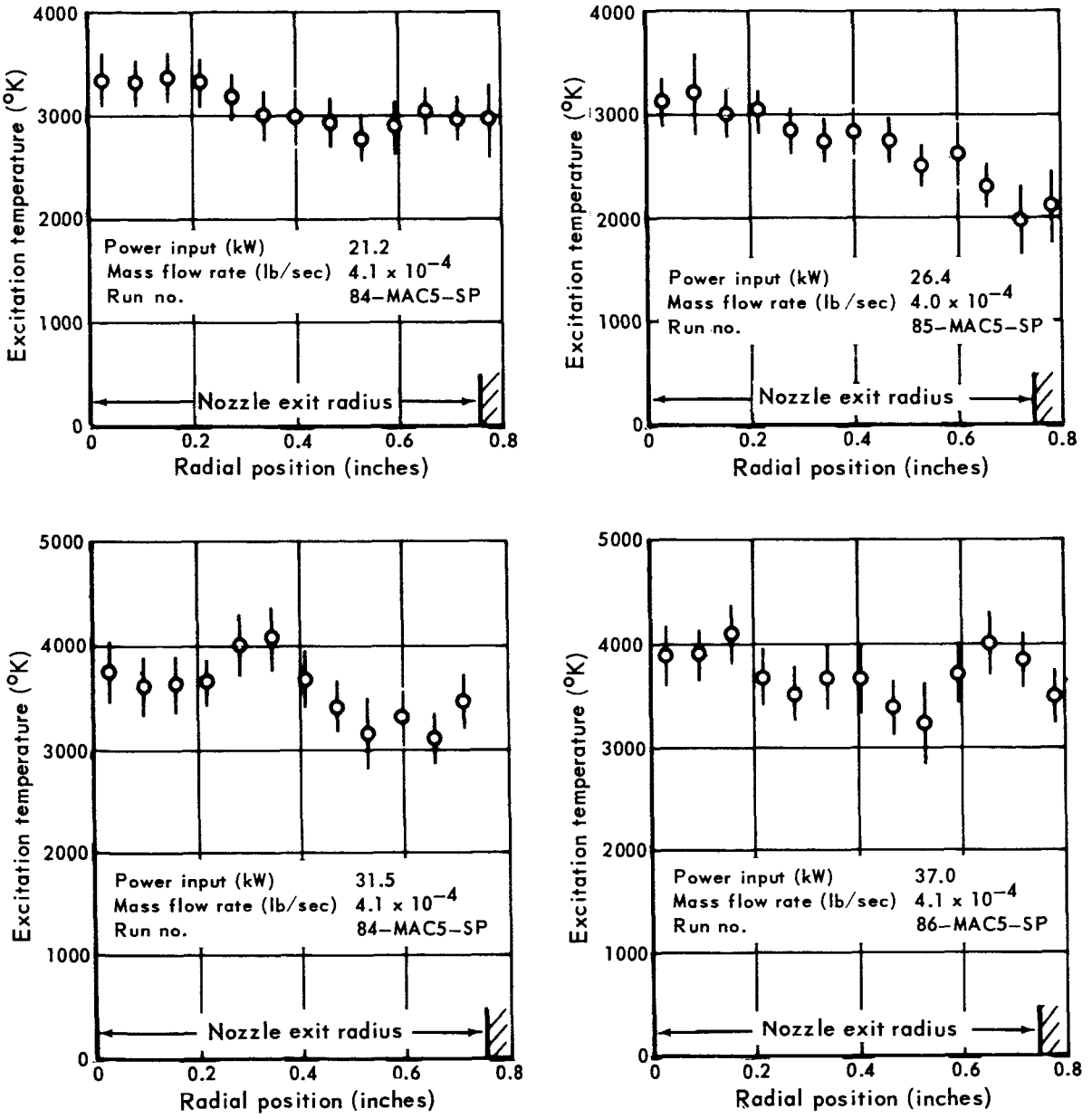

Fig. 4.32 Excitation temperature profiles on MAC–5 water-cooled arc-jet

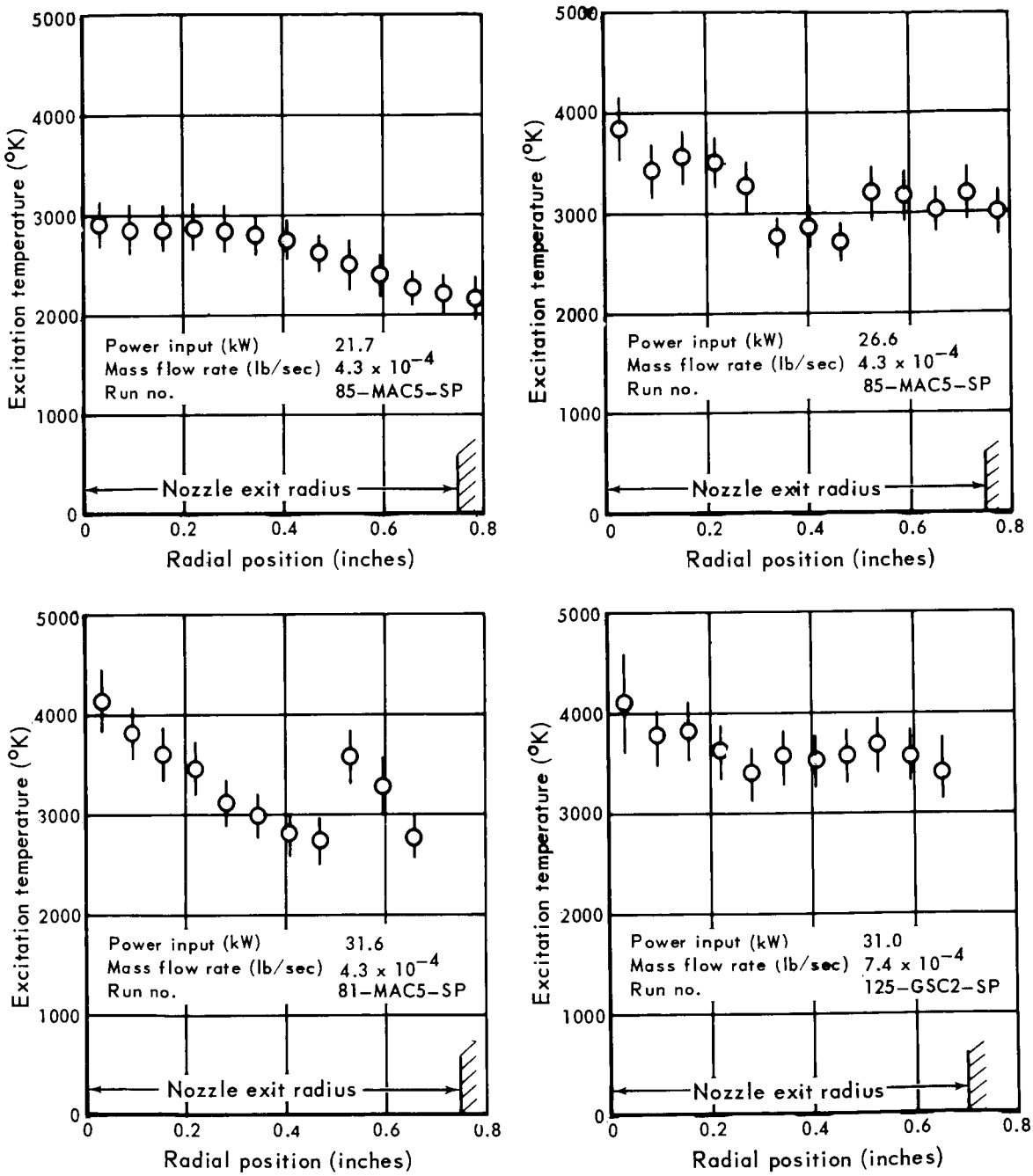

Fig. 4.33 Excitation temperature profiles on MAC–5 and GSC–2 arc-jets

with the data which would produce a minimum and maximum for each point of the inverted data. Due to the large number of curves required this was not attempted.

In view of the above it will be assumed that the measured temperatures are correct to within 15 to 20 percent.

Excitation temperature measurements on GSC–2 arc-jet

The excitation temperature profile obtained on the GSC–2 arc-jet is shown in Fig. 4.33 and is similar in nature within that obtained on the MAC–5 arc-jet. These results are somewhat higher than those obtained during the development of this arc-jet (Ref. 3).

4.6 *Electron density measurements*

Measurements of the electron concentration in the exhaust of the water-cooled arc-jet were obtained by means of Langmuir probe and spectroscopic techniques. The Langmuir probe apparatus, theory and technique of operation are described in Appendix G, and the method by which the electron concentration is inferred from the spectroscopic measurements is presented in Appendix F. The electron densities determined by these techniques are qualitative in nature and are probably accurate to within a factor of 3, however, these measurements are useful in establishing to what extent the exhaust stream is in a state of frozen flow.

Figure 4.34 presents the electron density measurements obtained with the Langmuir probe on the MAC–7 arc-jet at a position of 0.5 inches downstream of the nozzle exit plane. Measurements were attempted at positions close to the nozzle exit plane; however, difficulties were encountered due to incomplete isolation of the probe circuit from the arc discharge. The curve drawn through the experimental points at the 30.3 kW condition represents a possible fit of the data; however, care should be exercised in interpretation of this data due to the qualitative nature of the measurements. The several experimental measurements at the power input level of 19.3 kW resulted in lower electron densities by a rough factor of two thirds.

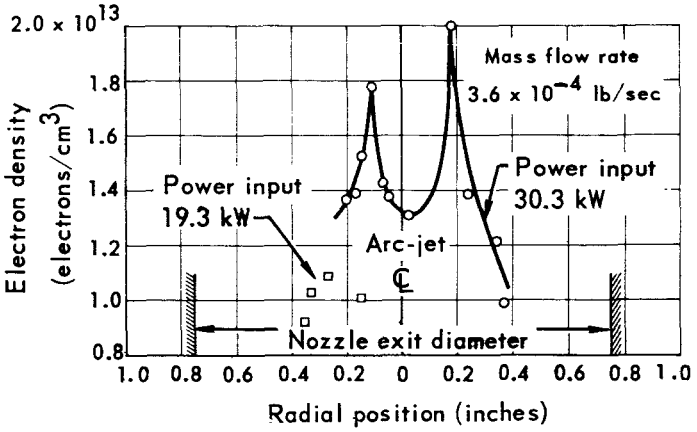

Fig. 4.34 Electron density profile on MAC–7 water-cooled arc-jet

Figure 4.35 shows the average electron density along a diameter of the MAC–5 arc-jet exhaust at a position of approximately 0.30 inches from the nozzle exit plane. The data were obtained by a measurement of the spectral line broadening due to the Stark effect. The Balmer β and δ lines were used to determine the electron density at the various power levels. The data plotted on Fig. 4.35 represent the average of data obtained from the β and δ lines which differed by approximately 20% of each other.

The electron density at the 35 kW, 3.6×10^{-4} lb/sec condition was also estimated by the Teller-Inglis rule (Appendix F). This technique requires

a measurement of the number of distinguishable spectral lines above the continuum and yielded an electron density of 3.2×10^{14} electrons/cm^3.

The results of the various measurements indicate that the electron concentration at the exit plane of the water-cooled arc-jets MAC–5 and MAC–7 is within the range of 1×10^{13} to 3×10^{14} electrons/cm^3, and that the effect increasing the power input from 20 to 35 kW raises the electron concentration by approximately a factor of two.

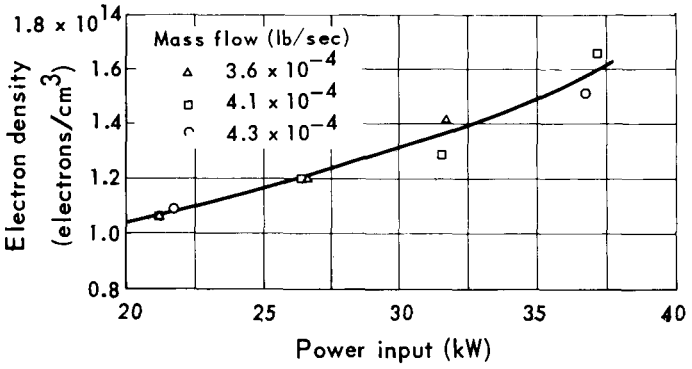

Fig. 4.35 Average electron density across exit plane diameter of MAC–5 water-cooled arc-jet

4.7 *Nozzle static pressure measurements*

Measurements of the static pressure were made at the nozzle exit plane of the water-cooled arc-jet (MAC–7) and the regeneratively-cooled arc-jet (GSC–2).

The exit plane static pressure is required in the calculation of the exit plane energy balance which is presented in the following section of this report.

Additional measurements were obtained of the static pressure distribution in the nozzle of the MAC–7 arc-jet from the end of the constrictor throat to a position 1.107 inches downstream of the throat.

Static pressure measurements on MAC–7 arc-jet

The nozzle of the MAC–7 arc-jet was instrumentated with a series of static pressure taps as shown in Fig. 4.36. The pressures were recorded with three Wallace and Tiernan pressure gauges, a 0 to 400 torr gauge, a 0–50 torr gauge, and a 0–20 torr gauge.

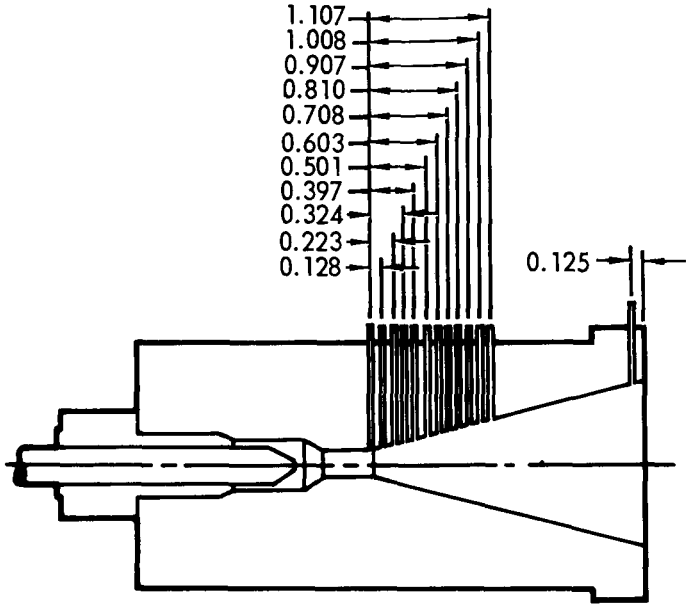

Note: All dimensions in inches

Fig. 4.36 Location of pressure taps on MAC–7 water-cooled arc-jet

Data was obtained for twelve operating conditions of this arc-jet and the results are plotted in Figs. 4.37 through 4.39. The static pressure drops rapidly immediately downstream of the constrictor exit for all flow rates and power levels. The pressure level recorded at tap number 4 did not assume a constant value but fluctuated between values slightly above the dashed curve and a value almost equal to the throat pressure. This behavior is most probably due to intermittent attachment of the arc discharge at this tap location and suggests

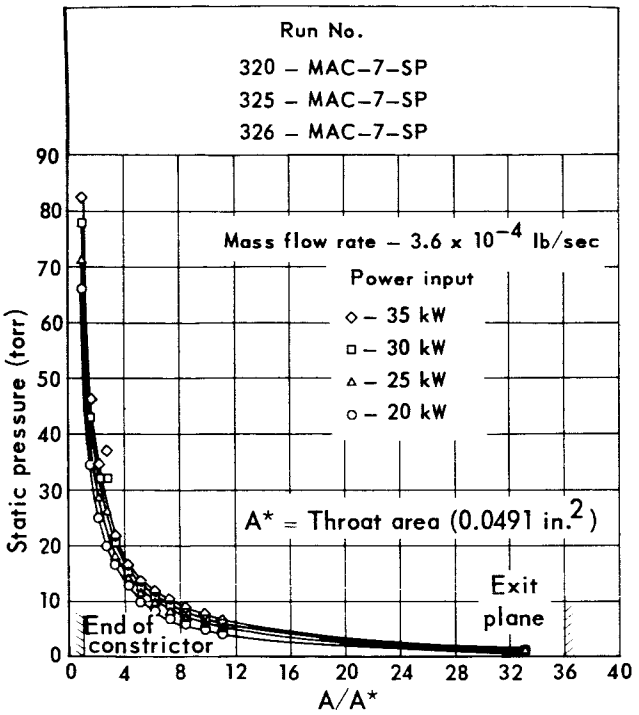

Fig. 4.37 Static pressure distribution on MAC–7 water-cooled arc-jet

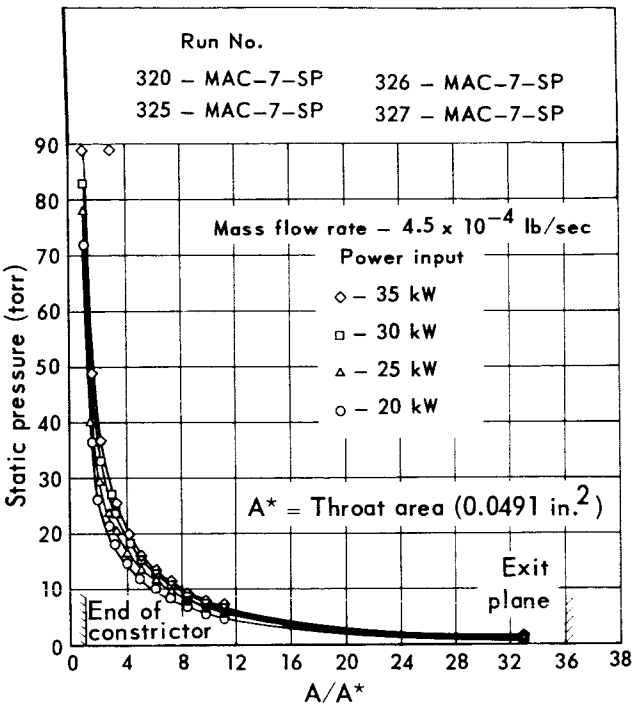

Fig. 4.39 Static pressure distribution on MAC–7 water-cooled arc-jet

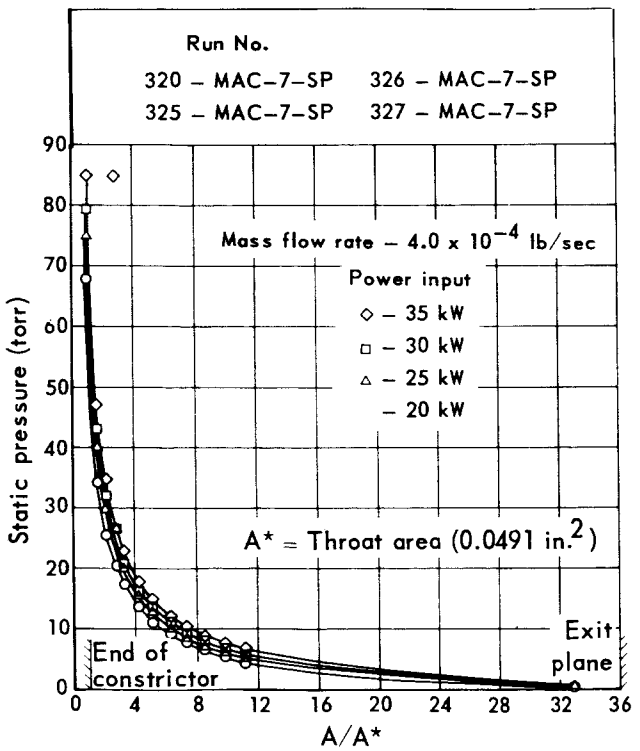

Fig. 4.38 Static pressure distribution on MAC–8 water-cooled arc-jet

that the axial arc attachment region is within a distance of 0.250 inches since taps 3 and 5 did not exhibit this characteristic.

Static pressure measurement on GSC–2

The static pressure on the regeneratively-cooled arc-jet was obtained by placing a small diameter tungsten tube adjacent to the nozzle exit plane. The end of this tube was ground to match the nozzle contour. This technique was used in lieu of machining a pressure port through the regeneratively-cooled nozzle and introduces an uncertainty into the measurement because of flow effects around the tube.

A pressure of 0.75 torr was recorded for a power input of 30 kW and a mass flow rate of 7.35×10^{-4} lb/sec.

5 Power balance at nozzle exit plane

Past experimental analysis of the arc-jet nozzle flow indicated that non-equilibrium is to be anticipated in the nozzle exhaust. The non-equilibrium conditions occur because the time for recombination of dissociated and ionized species is greater than the residence time within the nozzle. This phenomena is referred to as frozen flow and results in a power loss since the dissociation and ionization energy is not converted to kinetic energy. Hence, it is of interest to ascertain experimentally, if possible, the degree to which the nozzle flow is frozen.

If it is assumed that all the constituents of the nozzle flow have the same velocity at a given radial position of the flow, then a power balance for the flow at the exit plane is given by

$$\rho u\, h_t = \frac{\rho u^3}{2} + N_H \frac{Au}{2} + N_e\, Bu + \rho u \sum_i C_i\, h_i \qquad (1)$$

where h_t = stagnation enthalpy of stream
h_i = enthalpy of specie i
C_i = mass concentration of specie i
ρ = gas density
u = gas velocity
A = dissociation energy
B = ionization energy
N_H = atomic number concentration
N_e = electron number concentration.

The term on the left hand side of Eq. 1 represents the total energy passing through a unit area of the exit plane per second. The first term on the right hand side of Eq. 1 represents the kinetic power flux, the second and third terms account for the energy invested respectively in dissociation and ionization, and the last term containing the summation represents the energy contained in random thermal motion.

The nozzle exit plane measurements described in Section 4 can be used to calculate some of the terms of Eq. 1 directly and – with some assumptions – the other terms may be estimated.

5.1 Total power flux

The total power flux – the product of the local mass flux and the local stagnation enthalpy – was computed in Section 4.4 for the comparison of the measured power in the gas to the integrated power flux profiles.

The profiles of exit plane total power flux for the MAC–5 arc-jet are shown in Figs. 4.26 through 4.28 and the GSC–2 profile is shown in Fig. 4.30.

5.2 Kinetic power flux

The exit plane velocity profiles derived in Section 4.3 were combined with the mass flux profiles described in Section 4.1 to yield the kinetic power flux profiles.

Figures 5.1 through 5.3 show the kinetic power flux profiles on the water-cooled constricted arc-jet for the twelve operation conditions measured. The total kinetic power of the exhaust assuming cylindrical symmetry is obtained by

$$P_{KE} = 2\pi \int_{o}^{r_o} (\rho u) \frac{u^2}{2} r \, dr \qquad (2)$$

where P_{KE} = total kinetic power
r_o = nozzle exit radius.

The profiles shown in Figs. 5.1 through 5.3 were graphically integrated over the exit plane area and the results are presented in Table 5.1. Also shown in Table 5.1 is the thrust power as calculated from

$$P_T = \frac{T^2}{2\dot{m}} \qquad (3)$$

where P_T = thrust power
T = measured thrust
$\dot{m}$ = mass flow rate.

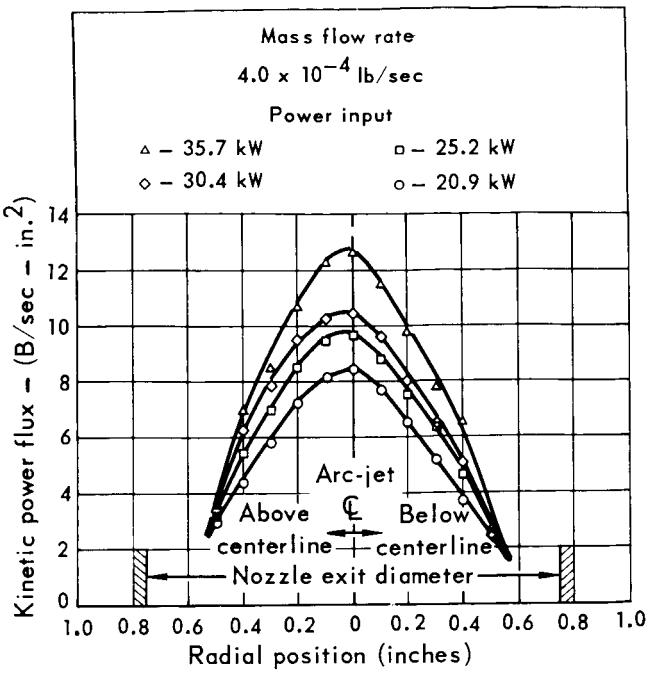

Fig. 5.2 Kinetic power flux profile on water-cooled arc-jet

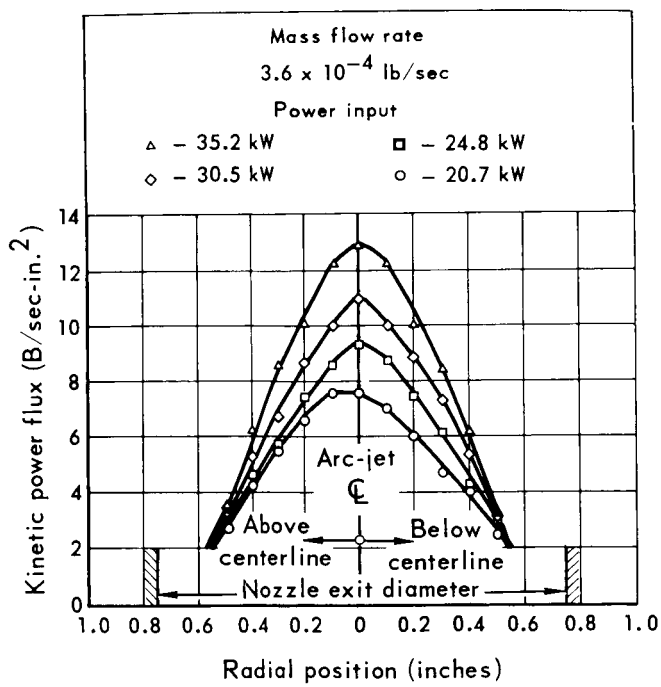

Fig. 5.1 Kinetic power flux profile on water-cooled arc-jet

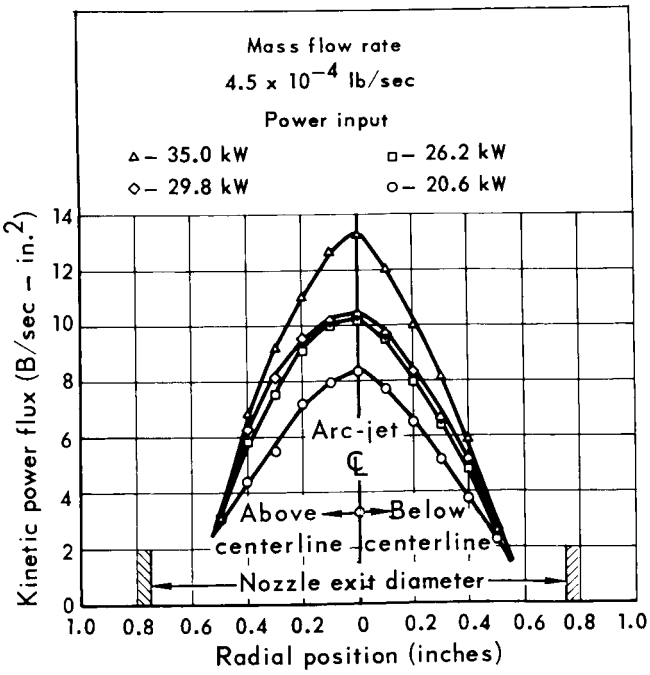

Fig. 5.3 Kinetic power flux profile on water-cooled arc-jet

Table 5.1 Measured total kinetic power on water-cooled arc-jet

Power input (kW)	Mass flow rate (lb/sec) x 10^{-4}	Kinetic power (kW)	Thrust power (kW)
20.7	3.63	5.3	5.3
24.8	3.63	6.4	6.2
30.5	3.63	6.8	7.4
35.2	3.63	7.8	7.4
20.9	4.02	5.9	4.9
25.2	4.02	6.7	5.9
30.4	4.02	7.2	7.1
35.7	4.02	8.0	8.2
20.6	4.50	6.0	4.9
26.2	4.50	6.9	6.2
29.8	4.50	7.0	6.9
35.0	4.50	7.9	7.7

The total kinetic power should be greater than the thrust power by an amount equal to the non-uniform flow loss or profile loss. As shown in Table 5.1 the kinetic power is above the thrust power for eight of the twelve conditions and below for the remaining conditions. Since negative profile losses are not physically reasonable, the discrepancy no doubt lies in the experimentally measured velocities. This is not completely unexpected, since the impact pressure from which the velocities are obtained is somewhat less than the momentum flux. For the Mach numbers encountered at the nozzle exit plane, the error in equating the impact pressure to the momentum flux is estimated at approximately 5 percent. Thus, the kinetic power would be estimated 10% low due to this effect.

Assuming the uncertainty of the kinetic power is ±15% and the uncertainty in the thrust power is estimated in Appendix A to be ±4%, then the maximum difference would be 20% of the nominal measured values. Thus, it is estimated that the profile losses for the water-cooled arc-jet are less than 4% of the input power.

It might also be pointed out that the uncertainty in the mass flux profiles (as well as extrapolations in velocity) for radii greater than 0.40 inches will contribute to uncertainties in kinetic power.

Figure 5.4 depicts the kinetic power flux profile for the GSC–2 regeneratively-cooled arc-jet. This profile was integrated over the exit plane area with a resulting total kinetic power of 14.2 kW. The thrust power measured at the 30 kW, 7.35 x 10^{-4} lb/sec operating condition was 15.6 kW. Thus, as for some of the water-cooled arc-jet tests, the kinetic power is less than the thrust power. If a 15 percent uncertainty in the kinetic power is assumed, then the kinetic power could be as much as 16.4 kW, and the thrust power could be as low as 15.0 kW assuming an uncertainty of 4 percent. Thus, the profile loss is estimated to less than 1.4 kW which is 4.7 percent of the input power. The above calculation

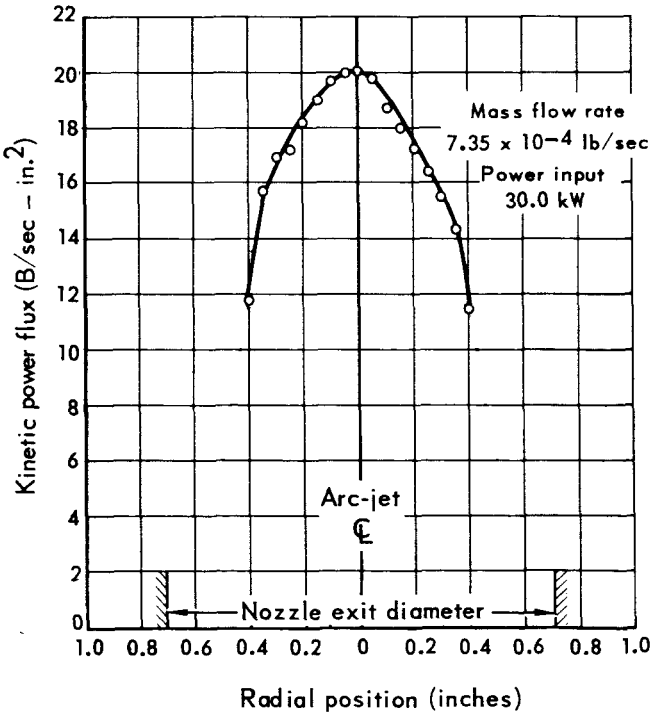

Fig. 5.4 Kinetic power flux profile on GSC–2 regeneratively-cooled arc-jet

represents the estimated maximum profile loss and is approximately the same for both arc-jets in terms of the input power; however, if we refer the profile loss to the kinetic power in the gas the profile loss for the GSC–2 arc-jet is approximately one half that of the water-cooled arc-jet. This is seen qualitatively in the GSC–2 velocity profile (Fig. 4.20) which is more uniform than the water-cooled arc-jet profiles (Figs. 4.17 to 4.19).

5.3 Frozen flow and thermal power flux

Referring to the local power balance (Eq. 1) at the nozzle exit plane and rearranging terms, we obtain;

$$\rho u h_t - \frac{\rho u^3}{2} = N_H \frac{Au}{2} + N_e Bu + \rho u \sum_i C_i h_i \qquad (4)$$

Since local measurements of the total power flux ($\rho u h_t$) and the kinetic power flux ($\rho u^3/2$) have been obtained, a subtraction of these two quantities will yield by Eq. 4 the local distribution of the sum of frozen flow and thermal power fluxes.

This subtraction was made for all the operation conditions on the water-cooled arc-jet and the results are shown in Figs. 5.5 through 5.7. Figure 5.8 presents similar data for the GSC–2 arc-jet.

It is noted that the total power invested in ionization and dissociation (frozen flow) and thermal modes can be obtained from gross measurements as soon as the kinetic power is specified; however, the significance of Figs. 5.5 through 5.8 is the manner in which this power loss is distributed throughout the flow. The results indicate the distribution for the water-cooled constricted arc-jet is peaked on the jet centerline and the peak becomes more pronounced as the power increased. The profile data also indicate that increases in power are reflected throughout the profile in roughly a proportionate manner. For example, at a flow rate of 3.6×10^{-4} lb/sec incremental power increases of 5 kW produce a change of centerline values by a factor of roughly 1.6 while the values at a radius of 0.4 inch increased by a factor of roughly 1.4.

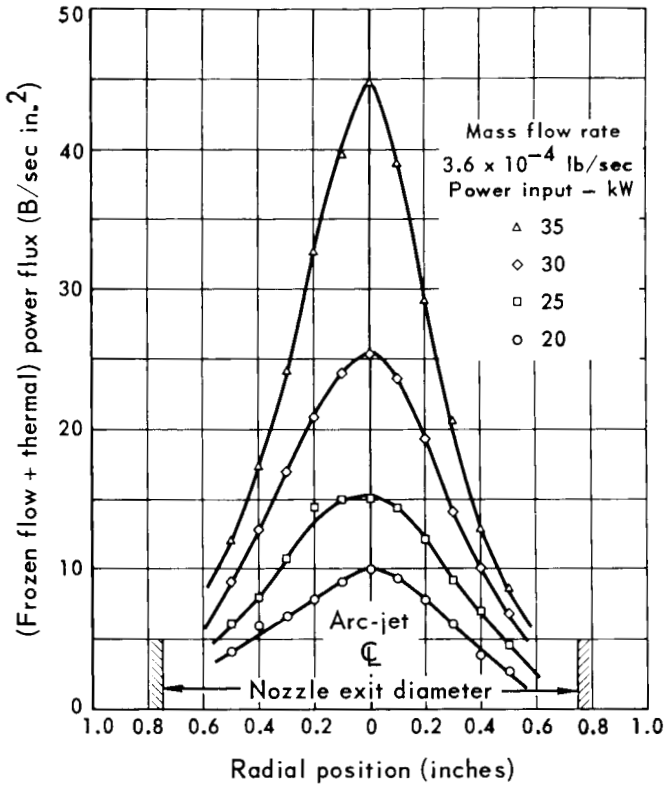

Fig. 5.5 Frozen and thermal power flux profiles on water-cooled arc-jet

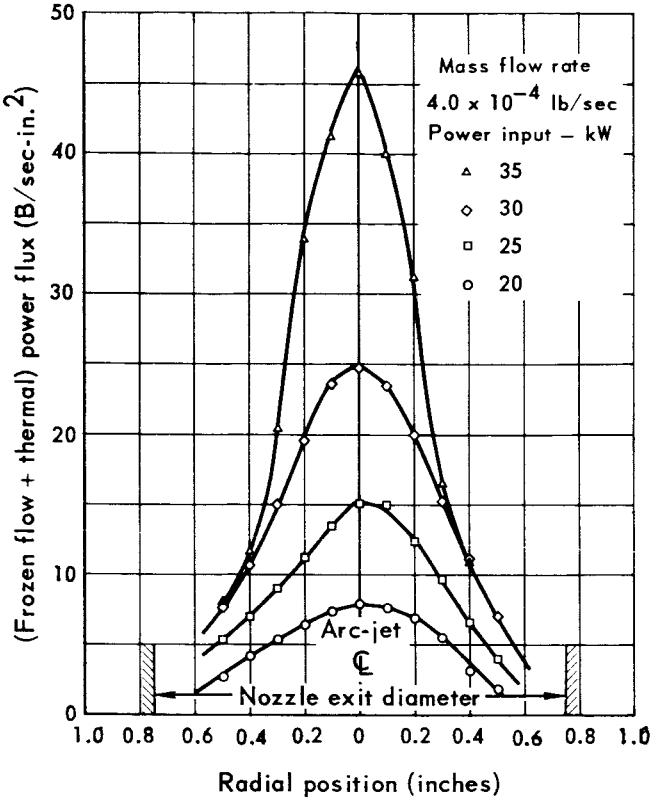

Fig. 5.6 Frozen and thermal power flux profiles on water cooled arc-jet

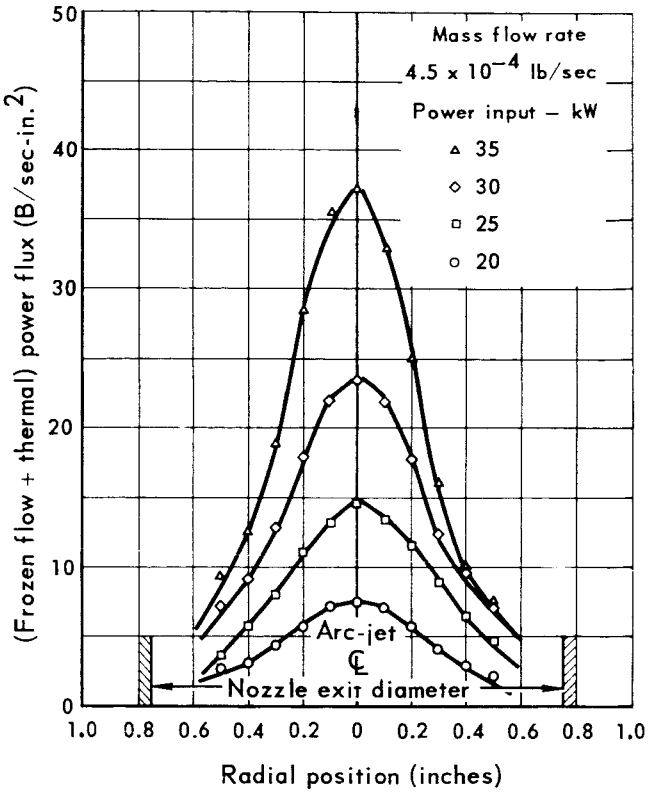

Fig. 5.7 Frozen and thermal power flux profiles on water-cooled arc-jet

5.4 Thermal power flux

An estimate of the thermal power can be obtained if it is assumed that the measured excitation temperature is the electron temperature and that the heavy particles (i.e., atoms, molecules, and ions) are in a state of equilibrium at a different, but common temperature.

Thus, the mass density is

$$\rho = M_H \left(N_H + 2N_{H_2} + N_e + N_e \frac{M_e}{M_H}\right) \qquad (5)$$

where M_H = mass of atomic hydrogen
M_e = mass of electron
N_{H_2} = molecular number concentration.

And the condition of charge neutrality ($N_e = N_+$) has been assumed. The last term of Eq. 5 can be neglected since M_e is much less than M_H, therefore

$$\rho = M_H (N_H + 2N_{H_2} + N_e) \qquad (6)$$

If we assume further that the static pressure as measured at the nozzle exit is constant over the exit plane area then the perfect gas relation gives

$$p_s/k = (N_H + N_{H_2} + N_e) T_a + N_e T_e \qquad (7)$$

where p_s = static pressure at exit plane
k = Boltzmann's constant
T_a = heavy particle temperature
T_e = electron temperature.

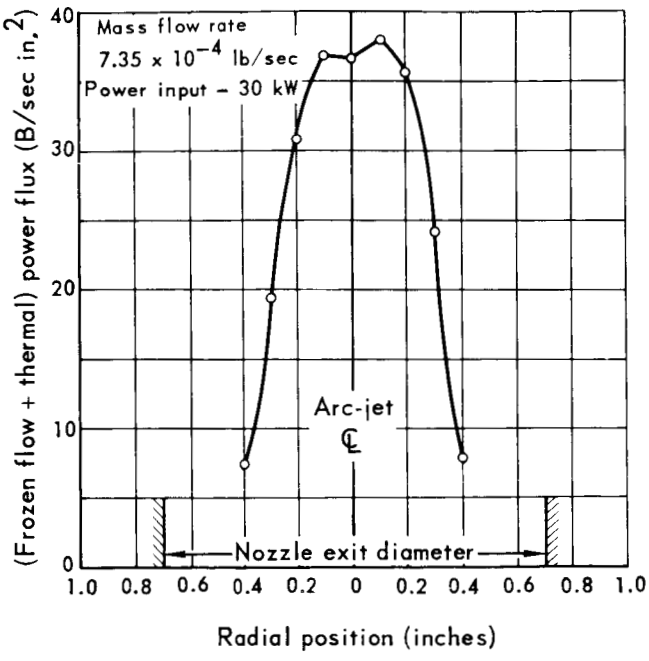

Fig. 5.8 Frozen and thermal power flux profiles on regeneratively-cooled arc-jet

Noting that

$$C_i = \frac{\rho_i}{\rho}$$

and $h_t = 5/2\ k\ T_a$

$h_e = 5/2\ k\ T_e$

Equation 1 can be rewritten as

$$(h_t - \frac{u^2}{2})\ \rho = N_H\ (\frac{A}{2} + M_H\ h_H) + 2N_{H_2}\ M_H\ h_{H_2} + N_e\ [B + 5/2k\ (T_a + T_e)] \qquad (8)$$

where h_H = enthalpy of atomic hydrogen

h_{H_2} = enthalpy of molecular hydrogen

The quantities h_H and h_{H_2} are functions of the heavy particle temperature and can be represented by the expressions (Ref. 4)

$$h_H = C\ T_a + f \qquad (9)$$

$$h_{H_2} = p\ T_a^2 + q\ T_a + r \qquad (10)$$

where $C = 2.062 \times 10^8$ ergs/g ^oK

$f = -6.146 \times 10^{10}$ ergs/g

$p = 0.883 \times 10^4$ ergs/$^oK^2$

$q = 1.142 \times 10^8$ ergs/g ^oK

$r = -1.890 \times 10^{10}$ ergs/g

Equations 6 and 7 can be solved for N_H and N_{H_2} as

$$N_H = \frac{2\ p_s}{kT_a} - \frac{\rho}{M_H} - N_e\ (2\ \frac{T_e}{T_a} + 1) \qquad (11)$$

and

$$N_{H_2} = \frac{\rho}{M_H} - \frac{p_s}{KT_a} + N_e\ \frac{T_e}{T_a} \qquad (12)$$

Substitution of Eqs. 9, 10, 11, and 12 into Eq. 8 results in a cubic equation in T_a

$$\{2p\ \rho\}\ T_a^3 + \{2M_H\ p\ (N_e\ T_e - \frac{p_s}{k}) + \rho\ (2q - c) + N_e\ [5/2k - C\ M_H]\}\ T_a^2 + \{N_e\ (B - \frac{A}{2} - M_H\ f) + N_eT_e\ [5/2k - 2M_H\ (c - q)] + (2r - \frac{A}{2M_H} - f - h_t + \frac{u^2}{2})\ \rho + p_s\ [2M_H\ \frac{(c - q)}{k}]\}\ T_a + \{2[\frac{A}{2} + M_H\ (f - r)]\ \frac{p_s}{k} - N_eT_e)\} = 0 \qquad (13)$$

The coefficients of the powers of T_a in Eq. 13 may be calculated from the experimental measurements described in Section 4, thus permitting the roots of Eq. 13 to be computed. Upon obtaining the value of T_a from Eq. 13 the values of N_H and N_{H_2} may thus be determined. The specification of T_a, N_H, and N_{H_2} permit the determination of the thermal power flux.

Although Eqs. 10, 11, and 12 will define N_H, N_{H_2}, and T_a once the values of p_s, ρ, h_t, T_e, U_s and N_e are given, an additional restriction which must be satisfied is that N_H and N_{H_2} be non-negative. If we assume that the experimental

measurements of p_s, ρ, h_t, T_e, and u are quantitatively correct then this condition will impose an upper and lower bound on the values of N_e. This argument could also be applied to any of the measured quantities.

The experimental measurements obtained on the water-cooled arc-jet at the 35 kW, 3.6×10^{-4} lb/sec operating condition were used to calculate T_a by Eq. 13. The electron density used in this calculation was 1.1×10^{14} electron/cm^3 which was the average of the Langmuir probe and spectroscopic line broadening data. Substitution of the calculated value of T_a into Eq. 12 resulted in N_{H_2} being negative.

Since the electron density measurements are considered the least accurate, it was assumed that the measured electron density was low. An electron density value of 1.1×10^{16} electron/cm^3 yielded a negative value for the atomic number concentration. The heavy particle temperatures for these two cases were 1050°K and 1600°K, respectively, thus the electron density used in the solution of Eq. 13 does not produce a strong effect on T_a and the correct value of N_e should be between the above N_e values.

The heavy particle temperature profiles were calculated for the water-cooled arc-jet operating conditions of 35 kW; 3.6×10^{-4} lb/sec and the 30 kW, 4.0×10^{-4} lb/sec. The electron density profiles used in these calculations were assumed to peak on the centerline at 1.1×10^{15} electron/cm^3 and 0.9×10^{15} electron/cm^3, respectively.

Figure 5.9 is a plot of the heavy temperature profiles obtained by the above procedure for the two operating conditions.

The thermal power was calculated using each of the profiles of Fig. 5.9 and resulted in values of 2.4 kW for the 35 kW condition and 2.1 kW for the 30 kW. Thus, the thermal power loss represents 6.9% and 7% of the input power for the two conditions.

It is noted that the individual specie concentration used in the above calculation may possess certain errors due to the manner in which the electron densities were chosen. However, it is expected the effects of these errors should not significantly affect the calculated thermal power since the thermal power term as expressed in Eq. 1 contains all of the number densities and the values of h_H and h_{H_2} are roughly the same.

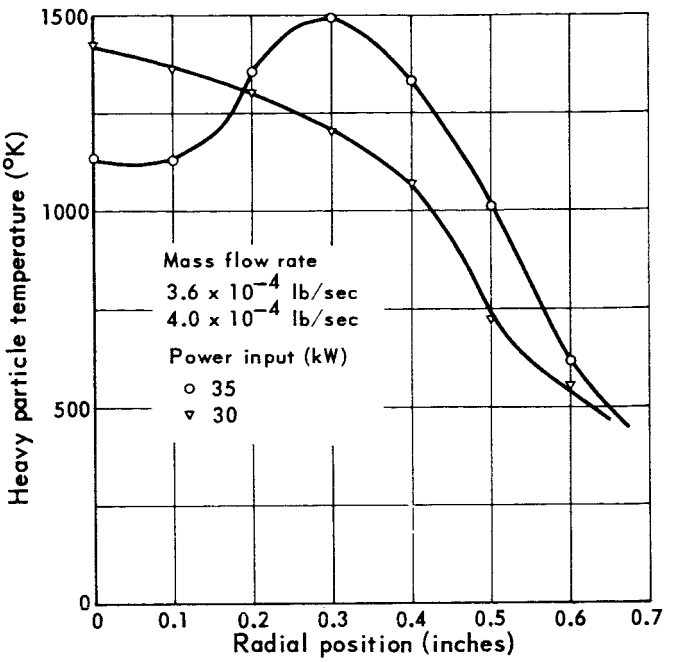

Fig. 5.9 Calculated gas temperature profiles on water-cooled arc-jet

5.5 Frozen flow power

Although errors in the values of N_e and N_H do not change the thermal power estimate greatly, they do have a significant effect on the frozen flow power as calculated by Eq. 1. Consequently, estimates of the frozen flow power flux based upon the calculated number densities are not considered valid.

Subtraction of the estimated thermal power from the sum of thermal and frozen flow powers described in Section 5.3 for the 35 kW, 3.6×10^{-4} and 30 kW, 4.0×10^{-4} lb/sec condition yields a frozen flow power of 17.4 kW and 14.8 kW, respectively, for these two conditions. The frozen flow loss for these two conditions represents 50% and 49%, respectively, of the power input.

6 Arc region flow properties

The preceding sections have described the experimental measurements of thrustor performance and nozzle exit plane measurements. This section is concerned with a correlation of the flow properties at the nozzle exit plane with those in the arc discharge region.

6.1 Constricted arc thrustor

Arc geometry – All the 30 kW arc-jets (other than the GSC–2 arc-jet) were of the constricted arc configuration. In this design the arc discharge extends from the conical cathode tip through the constant diameter region or constrictor and attaches to the anode nozzle in the divergent expansion region. The ratio of constrictor diameter to constrictor length was one half for all thrustors tested.

Experiments performed in this and other laboratories have shown that the arc discharge through the constrictor is located on the thrustor centerline, is constant in diameter over the length of the constrictor, and possesses a radius approximately equal to one-half of the constrictor radius. The attachment of the arc to the anode nozzle occurs at a position slightly downstream of the constrictor exit. The static pressure measurements on the MAC–7 (Section 4) arc-jet indicated that the attachment region is approximately 0.4 inch from the constrictor exit and distributed over an axial length of less than 0.2 inch.

The hydrogen propellant is introduced into the arc chamber through tangential ports behind the cathode and helps stabilize the arc column along the thrustor centerline. A small portion of the propellant passes through the arc and is heated to very high temperatures while the majority of the propellant flows around the arc column and is heated by radial conduction from the column.

Arc flow properties – Since diagnostic measurements in the constrictor region are quite difficult to perform due to the high temperature environment, analytical methods will be used to estimate the flow properties in the arc region.

The initial step required to calculate the gas dynamic properties at the nozzle throat is the description of the static temperature profile at that location. The most desirable means of establishing the temperature distribution would be through solutions of the continuity, momentum and energy equations for the arc discharge. These solutions would relate the local properties (i.e., temperature, velocity, density, etc.) in the arc column to the gross measurements of arc current, arc voltage, mass flow rate and the constrictor geometry. Obtaining the solutions to the conservation equations is a formidable task and to date has not been accomplished. Solutions to the energy equations have been obtained by some investigators after making simplifying assumptions which normally uncouple the momentum equation from the energy equation.

Solutions for the temperature distribution in the arc column region of a constricted arc device

have been generated from an energy balance which equates the ohmic heating rate to the rate of heat conducted radially out of the column. The solution of this model (Heller-Elenbaas) was obtained in Ref. 5 and in general, correctly predicted the main features of the energy transfer between the arc column and the gas. However, for detailed calculations of the power within the arc region, this solution was inadequate.

The Stine and Watson (Ref. 6) theory of the arc column also predicts the temperature or enthalpy distribution within the column region. This theory takes into account an axial convection term in addition to the radial conduction and ohmic heating terms. A closed form solution of the energy balance equation is obtained upon a linearization of the transport properties. This linearization procedure results in a good approximation for an air arc column for which the theory was originally applied; however, this is not the case for hydrogen in the range of enthalpies considered. In addition, measurements of the voltage gradient (Ref. 7) in the hydrogen vortex stabilized arc suggest that the applicable region of the Stine and Watson theory is near the cathode region.

A qualitative estimate of the flow conditions at the end of the constrictor can be obtained by a measurement of the static pressure at the throat (Section 4) and several assumptions concerning the flow.

- the constrictor flow is in a state of thermodynamic equilibrium,
- the static pressure is constant across the constrictor diameter,
- the flow is sonic at the end of the constrictor.

An initial temperature profile at the end of the constrictor is then chosen. This profile is selected such that the temperature peaks in the centerline, passes through a value of 6000°K at the edge of the arc column chosen to be roughly 0.6 of the constrictor diameter, and decreases to 500°K at the constrictor wall. The selection of the above profile is made consistent with the approximate temperature solutions described above.

This temperature profile is not completely arbitrary since the total mass flow, power input, and thrust of the arc-jet must be consistent with this chosen temperature profile.

The density profile $\rho(r)$ across the constrictor can be specified with the aid of the equilibrium tables once the temperature profile and static pressure are given.

Since the flow is sonic, the gas velocity is given by

$$u(r) = \left(\frac{\gamma p}{\rho(r)}\right)^{1/2} \qquad (1)$$

where $u(r)$ = gas velocity at radius (r)
γ = ratio of specific heats
$\rho(r)$ = gas density at radius (r)
p = static pressure at end of constrictor.

Thus, the mass flux profile is specified after the temperature profile and static pressure are prescribed. The mass flow rate condition can then be checked by

$$\dot{m} = 2\pi \int_0^{r_o} \rho\, u r dr \qquad (2)$$

where $\dot{m}$ = total mass flow rate
r_o = constrictor radius.

For the temperatures encountered in the arc column region it is found that the majority of the mass flux is located outside of the arc column region and consequently the temperature profile in this region (i.e., from the edge of the arc to the wall) determines if Eq. 2 is satisfied. It was found that raising the temperature in the central arc region by a factor of 3 produced only a slight effect on the mass flow relation.

The power flux profile is next determined by

$$\rho u h_t = \rho u \left(\frac{u^2}{2} + h_s\right) \qquad (3)$$

where h_t = stagnation enthalpy
h_s = static enthalpy at temperature T

The static enthalpy is obtained from the equilibrium tables at the static pressure and temperature for each radial position. The power in the gas up to the throat which should be approximately 85–90 percent of the input power is given by

$$P_{in} = 2\pi \int_{o}^{r_o} \rho\, uh_t\, r\, dr \qquad (4)$$

where P_{in} = power input.

Calculations of the power flux profile indicated the majority of the power flux is located within the arc column region and therefore, the power input condition is satisfied by the temperature distribution within the arc region.

The momentum flux at the throat must satisfy the following relation

$$T = 2\pi \int_{o}^{r_o} (\rho u^2 + p)\, r dr + \int_{A_T}^{A_{ex}} p_x dA \qquad (5)$$

where T = thrust

p_x = nozzle static pressure distribution

A_T = throat area

A_{ex} = nozzle exit area.

Figure 6.1 presents the temperature profile, mass flux profile, and total enthalpy profile which were calculated for the MAC–7 measured operating condition.

As shown in Fig. 6.1, extremely high temperatures are estimated in the arc column region. The high temperatures are a consequence of the condition that only a small fraction of the power is carried in the high mass flux region around the arc column and that the flow is in thermal equilibrium. For pressures near 0.1 atmosphere, it is expected that equilibrium should exist in a static arc without an external gas flow. The pressure at which departure from equilibrium conditions is anticipated for a static arc is approximately 10 to 20 torr. It is uncertain whether the same criteria apply to the constricted arc column exhausting into a vacuum.

It is noted that estimated profiles at the throat are based upon a number of assumptions which may not be fully satisfied in the actual situation. The assumption of thermodynamic equilibrium is probably the most suspect and would alter the profiles markedly if not fulfilled. The arc temperatures are considered somewhat unrealistic since radiation losses (neglected in the analysis) would prevent the attainment of such high temperature values.

Although the estimated profiles are open to some question, it is felt that they provide a qualitative picture of the flow conditions at the throat provided thermodynamic equilibrium exists in the constrictor flow.

Comparison of throat properties with exit measurements – Comparison of the profiles at the throat with the experimentally measured exit plane profiles (Section 4) indicate that nozzle expansion is quite removed from that of a conical isentropic expansion. The centerline stagnation enthalpy decreases by approximately an order of magnitude from the throat to the exit plane and the concentration of mass flow shifts from an approximate annular distribution at the throat to a relatively uniform distribution at the exit plane. An additional consequence of the high temperature at the throat is the attendant high centerline velocity which is greater than the exit plane velocity by roughly a factor of 2.5.

It is apparent that a rapid mixing of flow must occur within the nozzle expansion in order that the estimated throat profiles be consistent with the measured exit plane profiles. Given the profiles at the throat, mixing of the high temperature centerline flow with the cooler outer flow must occur by diffusion since there are large concentration and temperature gradients in the radial direction. Thus, conditions which would promote mixing exist in the estimated throat profiles; however, the question arises of whether the residence time of the gas within the nozzle is long enough to allow for the mixing required to make the pro-

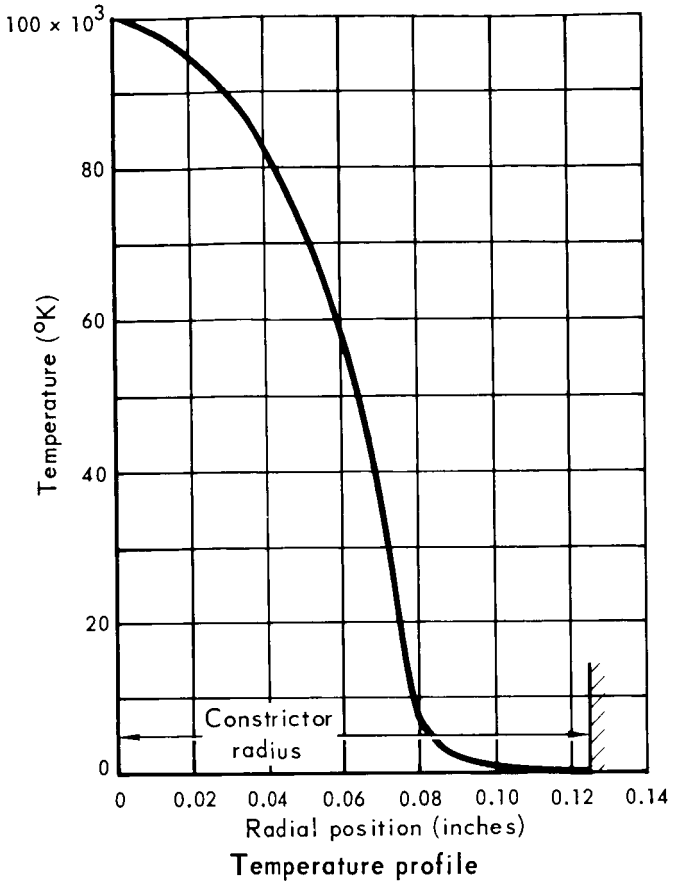

Temperature profile

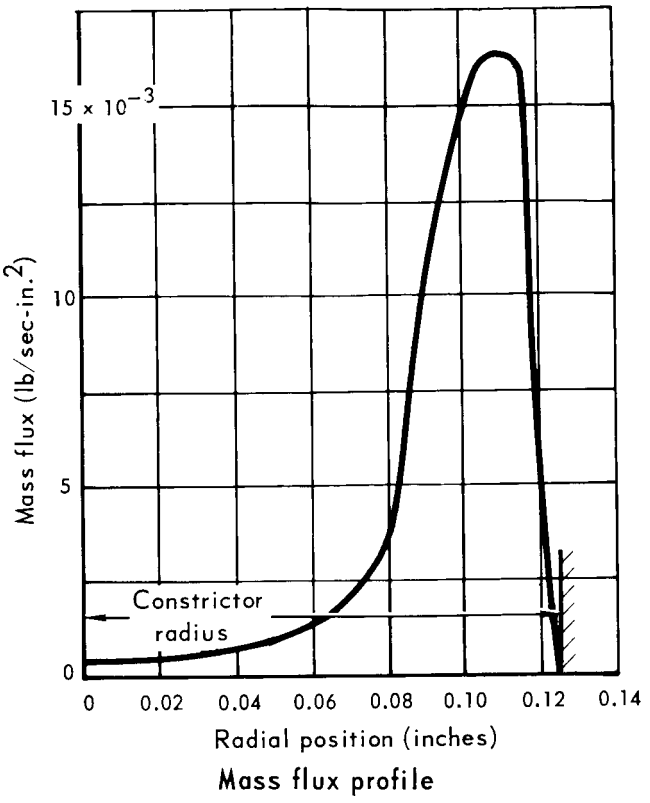

Mass flux profile

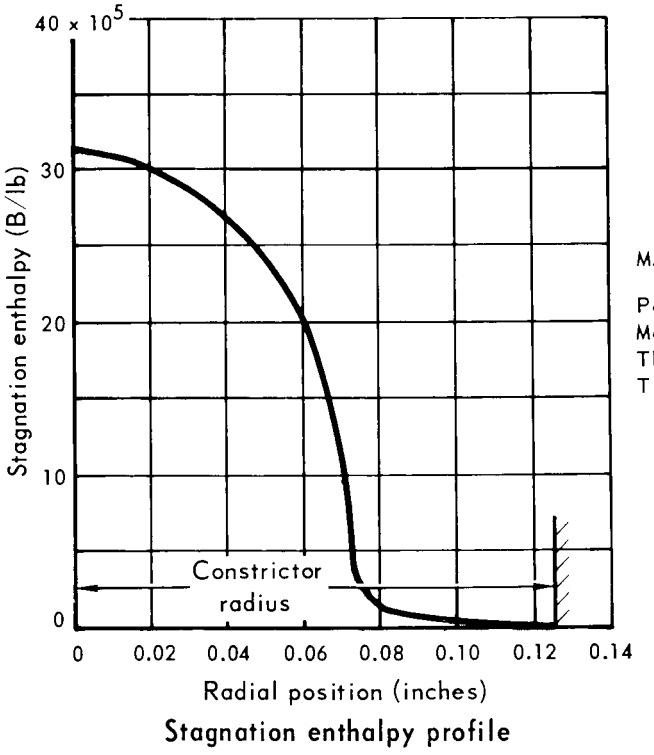

Stagnation enthalpy profile

MAC–7 arc-jet

Power input – 35.0 kW
Mass flow rate – 3.6×10^{-4} lb/sec
Thrust – 0.368 lb
Throat static pressure – 83 torr.

Fig. 6.1 Calculated profiles at constrictor throat of arc-jet

files at the two stations consistent.

A knowledge of the turbulent exchange coefficients for the flow would allow a determination of the possible decay in velocity and stagnation enthalpy as the flow proceeds through the nozzle; however, these quantities are not available for a supersonic hydrogen flow.

Resolution of the question could be attained through detailed experimental measurements of the flow conditions at the throat of the constricted arc-jet.

Discussion of results – Arc-jet operation in the constricted arc mode results in a device which is less susceptible to anode electrode damage since the anode attachment region is located in the divergent nozzle region which serves to effectively diffuse the anode spot. However, there are significant losses inherent in this mode of arc operation due to non-uniformity, frozen flow, and thermal effects which are a result of the large temperature gradients in the throat region. It has been suggested that operation in the constricted arc mode would result in a very high temperature core flow having a high specific impulse level, and a cooler outer flow of moderate specific impulse with the net result that higher frozen flow efficiency associated with the central core region would offset the increased profile losses. The experimental results obtained at the exit plane suggest that this is not the case. As the power level was increased at a constant flow rate, thus effectively increasing the central core temperature, the sum of the frozen flow and thermal power fluxes increased instead of decreasing as suggested. It is most likely that the majority of the energy increase given to the central core flow in the constrictor is not converted into directed kinetic energy but is transferred to the cooler outer flow by mixing in the nozzle.

For arc-jet operation at high current levels where the heat transfer due to electron condensation at the anode becomes the critical factor, the constricted arc mode is probably the most desirable arc-jet configuration, while at lower current levels a device which operates with the anode attachment upstream of the nozzle throat will produce a more efficient device.

6.2 Semi-constricted arc thrustor

The GSC–2 regeneratively-cooled arc-jet (Fig. 2.5) incorporates what is denoted as a semi-constricted arc configuration. In this design the arc discharge extends from the conical cathode tip through a short constrictor and attaches to the slightly larger diameter arc chamber wall which is situated upstream of the nozzle throat.

The propellant enters the thrustor behind the cathode through tangential ports as in the case of the constricted arc design. The propellant is heated as it passes through the arc discharge and then is mixed to some extent in the arc chamber before it passes through the nozzle throat and the divergent expansion region.

The results of the exit plane measurements on this arc-jet indicate that the profiles of velocity, total enthalpy, total power flux and sum of frozen flow and thermal power flux possess a higher degree of uniformity than the constricted arc configuration.

The overall thrust efficiency of this arc-jet at a power input level of 30 kW and a specific impulse level of 1000 sec was measured at 55% (Ref. 3). A thrust efficiency of 43% was obtained on a radiation-cooled version of this arc-jet (Ref. 3). While a comparison of the water-cooled constricted arc-jet performance is not applicable, data reported in Ref. 10 resulted in a thrust efficiency of 40% for a radiation-cooled constricted arc thrustor operating at the same power input and specific impulse.

In view of the exit plane measurements, it is suggested that the higher performance of the semi-constricted arc thrustor is a result of a lower non-uniform profile loss. The increase in uniformity is most likely accomplished in the arc chamber mixing region upstream of the throat.

Attachment of the arc anode spot in the high pressure arc chamber region of an arc-jet is usually accompanied by high erosion rates and a high probability of chamber wall failure due to the concentration of the anode attachment to a small surface area. The GSC–2 arc-jet configuration suffered from neither of these problems. The results of the velocity meter experiments indicate that there are acoustic type resonances associated with this arc-jet which are generated in the arc chamber. Further investigation of this phenomena is required. However, there is a strong indication that the resonance conditions are causing or are a result of the movement of the arc anode attachment within the arc chamber.

7 Conclusions

7.1 Thrust measurement

The single pendulum thrust stand gives reliable thrust measurements for radiation and water-cooled thermal arc-jets operating in the range of 30 kW. The accuracy of the thrust measurements was ± 2%.

The combined measurements of thrust, mass flow rate, and power input give specific impulse, and thrust efficiency values within an estimated error of 2.5 and 4% respectively.

The thrust measurements on the MPD arc-jet are considered preliminary due to the large tare forces associated with the interaction of the applied magnetic field and the steel vacuum chamber.

7.2 Mass flux measurement

The local mass flux distribution can be measured in the exhaust of a hydrogen arc-jet with a water-cooled copper probe under local stagnation enthalpy levels up to 280,000 B/lb without physical damage to the probe.

The local mass flux measurements obtained with the mass flux probe and the volume collection technique have an estimated accuracy of 2.5%.

Comparisons of the metered total mass flow rate with the integrated mass flux profile yielded good agreement for all tests. The best agreement is obtained at the high mass flow rates and when the nozzle boundary layer is small.

7.3 Impact pressure measurement

The local impact pressure distribution can be measured in the exhaust of a hydrogen arc-jet with a water-cooled copper probe under local stagnation enthalpy levels above 300,000 B/lb without physical damage to the probe.

The impact pressure probe measurements have an estimated accuracy of ± 2%.

Comparisons of the measured thrust and the integrated impact pressure profiles resulted in good agreement for all conditions tested.

7.4 Velocity measurement

Arc-jet exit plane velocity profiles can be obtained by a combination of local mass flux and impact pressure measurements.

The accuracy of the velocity measurements determined by the probe technique is estimated at 10%. Approximately one half of the velocity uncertainty is the result of equating the impact pressure to the local momentum flux.

The inherent light fluctuations in the arc-jet exhaust propagate at a velocity dependent upon the thrustor geometry. The propagation velocity was close to the exhaust velocity for the constricted arc thrustor. For the semi-constricted arc thrustor the propagation velocity was greater than the exhaust velocity by an amount approximately equal to the local sonic speed.

The measurement of exhaust velocities by the photometric velocity meter technique results in a lower than actual velocity profile when the propagation velocity is equal to the exhaust velocity. The exhaust centerline velocities are approximately 20 to 30% lower than the actual velocities. This result is inherent in the experimental technique since "side on" observation made through the total exhaust region serve to average the measurements over the observation region.

7.5 Stagnation enthalpy measurement

The local stagnation enthalpy can be measured in the exhaust of a hydrogen arc-jet using a water-cooled calorimeter probe under local stagnation enthalpy levels up to 275,000 B/lb without physical damage to the probe.

The stagnation enthalpy profiles measured were reproducible and had an estimated accuracy of 5%.

Comparisons of the measured power to the exhaust flow and the integrated power flux profiles resulted in a range of agreement between 75 and 100% for all conditions tested. The majority of the comparisons were within 90 to 100 percent agreement.

Improvement in maximum operating level of this probe could be accomplished by increasing the sampling diameter of the probe.

7.6 Excitation temperature measurement

Qualitative measurements of the excitation temperature profiles at the arc-jet exit plane can be obtained by the method of relative line intensities applied to the hydrogen Balmerelines.

An undetermined uncertainty is introduced in the excitation temperature profiles by the Abel inversion of the measured "side on" line intensities to radial intensities.

7.7 Electron density measurement

Qualitative determinations of the electron density in the exhaust plasma can be obtained through the use of Langmuir probe and spectral line broadening techniques.

The uncertainty in the Langmuir probe data was largely due to insufficient isolation of the probe from the arc discharge.

The electron densities determined from the spectral line broadening possess a large uncertainty because the Stark broadening effect is not large at the measured densities and also because the integrated line shape was used rather than the inverted radial line shape.

A need exists for a more accurate determination of local electron concentrations which could be combined with the density, velocity, enthalpy and electron temperature to give the neutral particle concentrations within the exhaust.

7.8 Exhaust properties of constricted, water-cooled arc-jets - MAC-4, MAC-5, MAC-7

The alignment and machining of the tangential propellant injection ports is an important factor concerning exit plane flow symmetry.

The exit plane profile of impact pressure, velocity, and stagnation enthalpy peak of the exhaust centerline. The profile of velocity and stagnation enthalpy possess strong radial gradients which become more pronounced as the power input is increased.

The profiles of mass flux and density at the exhaust exit plane exhibit dips (minimums) on the thrustor center line.

The profiles of excitation temperatures are relatively flat over the exit plane diameter. The centerline temperatures ranged from 4200° to 2900°K with the edge temperature approximately 1000°K lower in magnitude. The excitation temperature profiles in general increased with increased bulk stagnation enthalpy.

The profile of kinetic power flux peaked on the exhaust centerline and exhibited a strong radial gradient. The non-uniform profile loss was estimated at approximately 5% of the input power.

The profiles of frozen flow and thermal power flux peaked on the exhaust centerline and the radial gradient increased as the input power increased.

A calculated profile of heavy particle temperature which peaked on the centerline indicated the ratio of excitation temperature to heavy particles temperature was approximately 3.

If thermodynamic equilibrium exists in the region of the constrictor then a rapid mixing of the flow through the arc and flow around the arc column occurs within the expansion nozzle.

7.9 Exhaust properties of semi-constricted, regeneratively-cooled arc-jet, GSC-2

The profiles of mass flux, density, and impact pressure possessed a dip or minimum on the exhaust centerline. The impact pressure profile was in contrast to the profiles on the constricted arc thrustor which peaked on the centerline.

The profiles of velocity and stagnation enthalpy peaked on the centerline however, the radial gradients were not as large as for the constricted arc thrustor.

The excitation temperature profile was relatively uniform with a centerline temperature of 4100°K and an edge temperature of 3400°K.

The total power flux, the kinetic power flux and the sum of frozen flow plus thermal power flux possessed a flat or uniform distribution over the central flow region which contrasted with the profile of the constricted arc thrustor which peaked sharply on centerline.

The difference in performance of the 30kW radiation-cooled version of the semi-constricted arc-jet and the radiation-cooled constricted arc thrustor can be attributed to lower profile losses associated with the former arc-jet.

8 Appendices

Appendix A Thrust stand

Two thrust stands were utilized in this program. The thrust levels of the two 30 kW radiation-cooled arc-jets (NAS–1, MAC–2) were measured with a double pendulum thrust stand developed under a previous contract, NAS3–3562. A single pendulum thrust stand designed and fabricated during this program was used to measure the thrust of the 30 kW water-cooled arc-jet (MAC–5), the 30 kW regeneratively-cooled arc-jet (GSC–2), and the water-cooled MPD arc-jet.

Experimental apparatus

A description of the double pendulum thrust stand is presented in Ref. 9. Two modifications of this thrust stand were made during the program which reduced the zero shift to approximately 0.015 lb over a test duration of 1 hr. The modifications were the replacement of steel support rods with Kovar rods, and incorporating a cooling jacket around the force transducer.

Figure A–1 is a sketch of the single pendulum thrust stand. This thrust stand was designed for the arc-jet operation up to 200 kW, the anticipated range of operation considered for the MPD hydrogen arc-jet. This system is basically a single pendulum suspension system. A horizontal arc-jet mounting plate is suspended by four Kovar flexures. Displacement of the mounting plate is limited by the characteristics of a variable inductance force transducer which produces an electrical signal directly proportional to the arc-jet thrust. A double-walled water-cooled oil container maintains the flexures and force transducer at a constant temperature. The entire system is mounted on a 3 ft. diameter vertical vacuum system blank-off plate and carriage assembly which provides easy access for adjustment, calibration, and thrustor mounting.

Electrical power is supplied to the arc-jet through the use of copper bus bars which are terminated in mercury cups. Coolant water is supplied to the arc-jet through flexible Tygon tubing.

The possibility of arcing external to the arc-jet is reduced by insulating all components that were above ground potential. The mercury surfaces are covered with silicone fluid to prevent arcing.

Instrumentation of the system is provided for measurements of thrust, arc chamber pressure, vacuum chamber pressure, arc voltage, arc current, propellant flow rate, and structural temperatures at several points on the arc-jet and thrust stand. All of the parameters are recorded continuously during a test by a direct readout oscillograph.

Calibration of the thrust stand is accomplished by means of a thin wire which is connected to the force transducer at the arc-jet centerline and

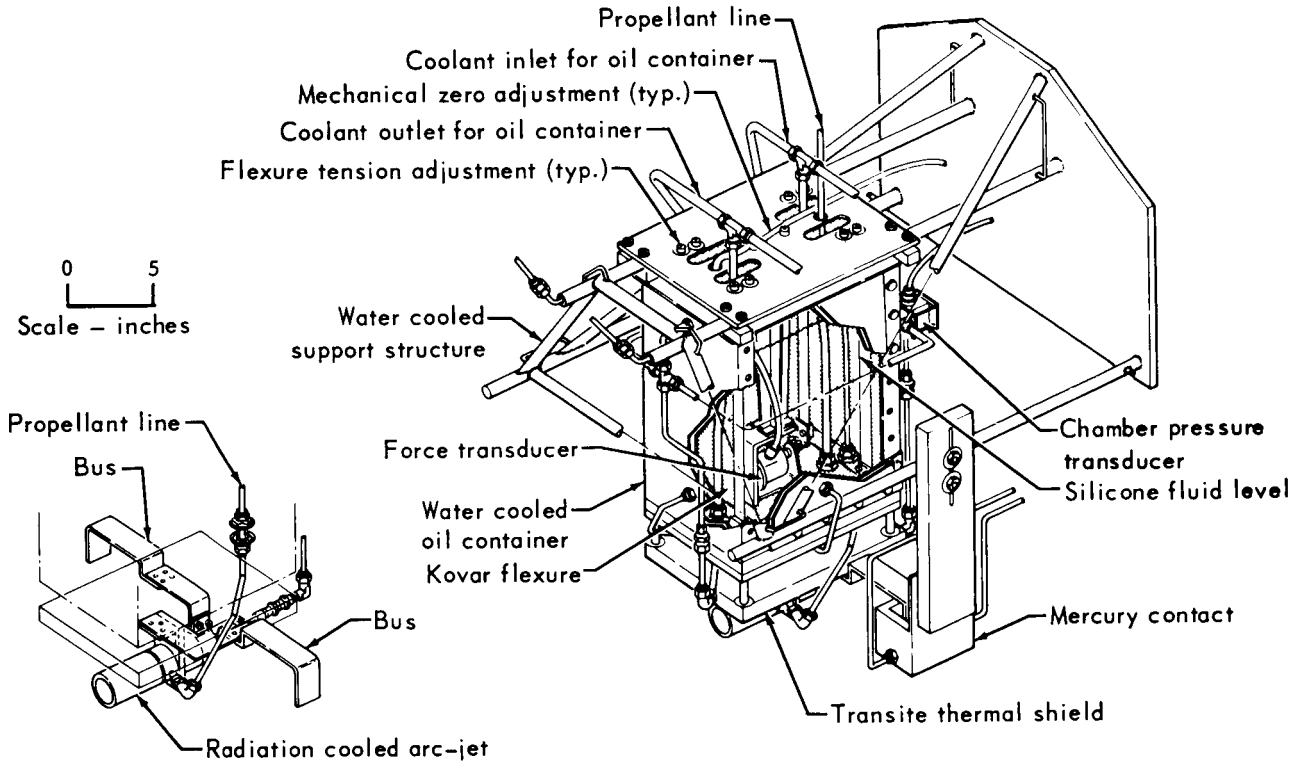

Fig. A–1 Arc-jet single pendulum thrust stand

passes through the blank-off plate and over a precision pulley. The addition of a standard weight to the wire simulates a known thrust.

Experimental procedure

Thrust measurements were obtained utilizing the following sequence:

- Prior to installation in the vacuum system the force transducer is removed from the thrust stand and calibrated.
- After installation of the transducer, instrumentation, and cooling lines the entire system is calibrated in the atmosphere. The calibration curves are compared to determine if the tare loading of the system is acceptably small and if the response of the transducer is linear.
- The system is then installed in the vacuum tank and the tank is evacuated. Another calibration is made with the system evacuated and the coolant flowing through the thrust stand. The arc-jet was then started. The starting procedure is described in Section 2.6.
- Periodically during the test, a calibration weight is added which simulates a known increase in thrust. This check determines any change in sensitivity which may have occurred due to thermal loads or changes in water pressure.
- After arc-jet shutdown, another calibration is made under vacuum conditions and compared with the calibration which preceded the test.

The thrust characteristics of the various arc-jets are presented in Section 3. For all of the 30 kW

arc-jet tests the thrust measurements were reproducible within ± 2%. The thrust measurements on the MPD arc-jet resulted in some data scatter and most likely was due to instabilities in the arc mode.

Error analysis

The uncertainty in the 30kW thrust measurements is considered to be ± 2%. The total propellant mass flow rate is measured by a sonic nozzle flowmeter. The pressure and temperature upstream of the flowmeter are used to calculate the flow rate from the relation

$$\dot{m} = C \frac{P}{\sqrt{T}} \qquad (A-1)$$

where $\dot{m}$ = mass flow rate

P = upstream pressure – accuracy of 0.5%

T = upstream temperature – accuracy of 1%

C = calibration constant – accuracy of 1%

Thus, the uncertainty in m is

$$\frac{\Delta \dot{m}}{\dot{m}} = \left[\left(\frac{\Delta C}{C}\right)^2 + \left(\frac{\Delta P}{P}\right)^2 + \frac{1}{2}\left(\frac{\Delta T}{T}\right)^2 \right]^{1/2}$$

$$= \sqrt{1.50 \times 10^{-4}} = 1.25 \times 10^{-2} = 1.25\%$$

The power input is the product of the arc voltage and arc current. The current and voltage are measured with a precision Weston voltmeter and ammeter with accuracy 1%. However, the power supply has a small ripple which increases the uncertainty in the power input to ± 2.5%.

The specific impulse is calculated by Eq. 1

$$I_{sp} = \frac{T}{\dot{m}}$$

The uncertainty in I_{sp} is

$$\frac{\Delta I_{sp}}{I_{sp}} = \left[\left(\frac{\Delta T}{T}\right)^2 + \left(\frac{\Delta \dot{m}}{\dot{m}}\right)^2 \right]^{1/2}$$

$$= \sqrt{5.5 \times 10^{-4}} = 2.35 \times 10^{-2} \text{ or } 2.5\%$$

The thrust efficiency is calculated by Eq. 2

$$\eta_{thrust} = 0.0218 \frac{T^2}{P_{in}\,\dot{m}}$$

The uncertainty in η_{thrust} is

$$\frac{\Delta \eta}{\eta} = \left[2\left(\frac{\Delta T}{T}\right)^2 + \left(\frac{\Delta m}{m}\right)^2 + \left(\frac{\Delta P_{in}}{P_{in}}\right)^2 \right]^{1/2}$$

$$= \sqrt{15.7 \times 10^{-4}} = 3.97 \times 10^{-2} \text{ or } 4\%.$$

Appendix B Mass flux probe

A mass flux probe was developed for measuring mass flux profiles at the nozzle exit plane of an arc-jet. The design chosen to accomplish these measurements was a hollow tube device having a normal shock inlet. A sharp conical lip was used so that an undisturbed streamline of the supersonic exhaust equal to the probe inlet area would be captured. A measurement of the gas flow rate through the probe with the normal shock swallowed allows the product of the stream velocity and density to be computed.

Apparatus

The mass flux probe (Fig. B–1) consists of a water-cooled inlet tube, a probe body, and a water-cooled shield to deflect the exhaust away

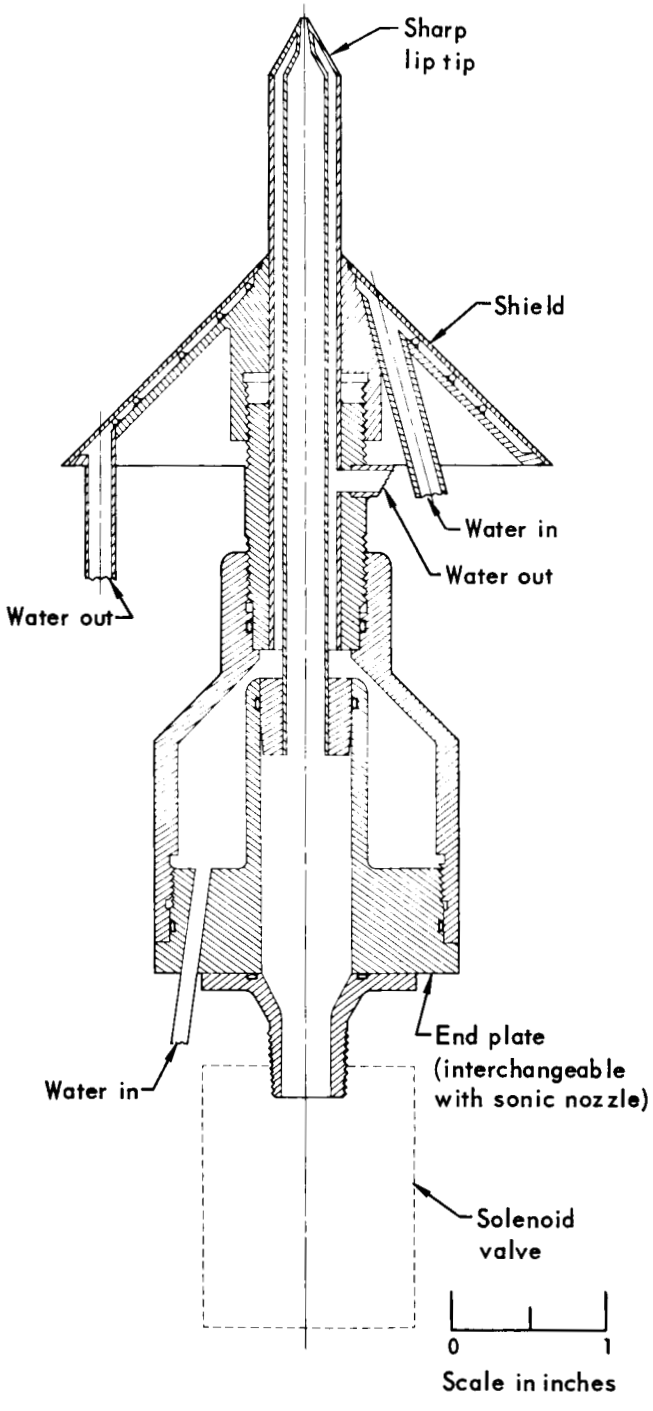

Fig. B–1 Water-cooled mass flux probe

the probe body. The inlet tube is composed of two concentric copper tubes which are brazed to the copper inlet lip. The outside diameter of the inlet tube is 0.750 inch. Water is directed to the inlet lip by means of wire flow dividers located between the concentric tubes.

Several inlet lip geometries were tested during the experimental program. The lip configuration shown in Fig. B–2(a) was used to measure the mass flux profile on the GSC–2 arc-jet and performed satisfactorily in that the integrated mass flow was 97 percent of the metered flow. Measurements with this lip on the MAC–4 arc-jet resulted in 70% agreement with the metered flow rate.

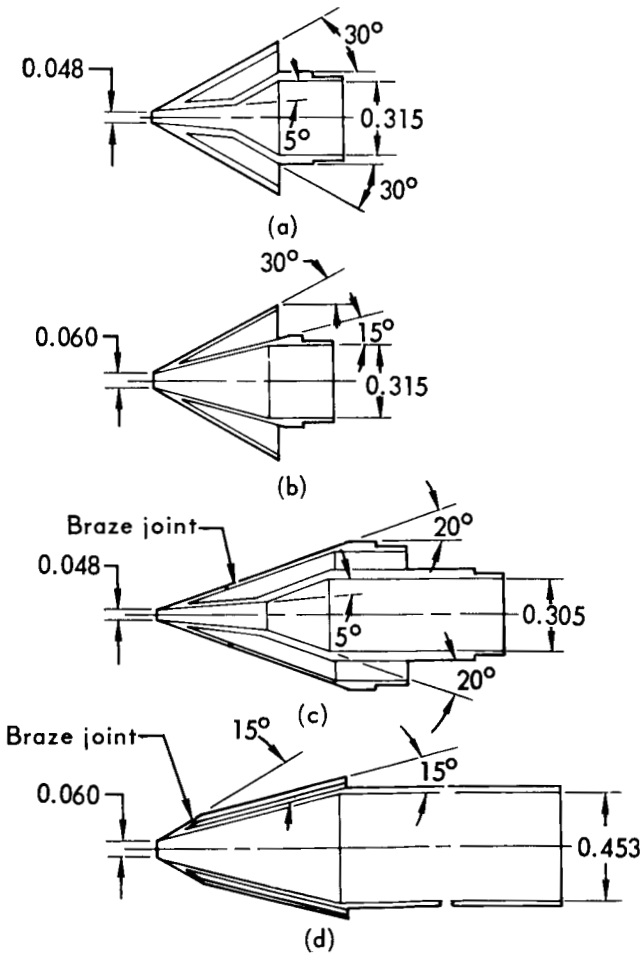

Note – All dimensions are in inches

Fig. B–2 Inlet lip configurations for mass flux probe

It was thought that external and internal lip angles were possibly preventing complete capture of the normal shock, consequently the lips shown in Figs. B–2(b) and (c) were fabricated. The internal angle was increased to 15 degrees for the lip shown in Fig. B–2(b) and the external angle was reduced to 20 degrees for the lip shown in Fig. B–2(c). No improvement in the amount of flow captured was realized with either of these configuration changes.

Possible boundary layer development within the inlet flow tube was next investigated. The flow tube was shortened approximately one inch and the inlet diameter was increased to 0.453 inch. This lip is shown in Fig. B–2(d). This modification resulted in a profile which integrated to 86% of the metered flow on the MAC–4 arc-jet. Since there is a large boundary layer near the arc-jet nozzle wall which is probably subsonic, it was concluded that the percentage agreement was near the maximum that could be obtained with the probe. Visual observations of the normal shock during the measurement in the core region of the jet indicated that the shock was captured. Thus, the MAC–4 mass flux measurements were obtained with the lip shown in Fig. 2–B–d.

Two methods were used to measure the mass flux captured by the probe. The first makes use of a sonic flow nozzle at the exit end of the probe as a flowmeter. The second method makes use of a volume collection system in which a sample is collected for a measured length of time.

Determination of the probe mass flow rate by means of a sonic flow nozzle requires a measurement of pressure and temperature before the choked nozzle. The initial mass flux measurements were made with a sonic flowmeter located at the end of the flow tube. This technique worked well in the core region of the exhaust; however, measurements could not be obtained at radii near the arc-jet nozzle wall due to an insufficient pressure ratio across the nozzle. For this reason, the collection method described below was used for all the measurement reported.

Figure B–3 is a sketch of the volume collection system. This system consists of a solenoid valve adjacent to the mass flux probe which allows flow into an 876.3 cubic inch collection tank for a given length of time recorded by a digital counter. A 4 inch diameter, air operated, solenoid controlled valve was used between the collection tank and diffusion pump. The volume collection tank is evacuated by a 4 inch oil diffusion pump and a small mechanical vacuum pump.

Since the temperature of the gas entering the collection tank is approximately at room temperature and is constant during the collection, one can obtain from the universal gas law ($pV = mRT$) by differentiating with respect to time

$$\frac{dp}{dt} = \frac{RT}{V}\frac{dm}{dt} \qquad \text{(B–1)}$$

where p = tank pressure
T = temperature of collection gas
V = volume of collection tank
R = gas constant
m = mass of gas collected
t = time

or that the mass flow rate ($\dot{m}$) into the probe is

$$\dot{m} = \frac{V}{RT}\frac{dp}{dt} \qquad \text{(B–2)}$$

where

$$\dot{m} = \frac{dm}{dt}$$

Therefore, the mass flow is a direct function of the pressure slope.

Figure B–4 is a typical plot of the pressure rise in the collection tank as a function of time. The immediate sharp rise in the pressure upon initiation of the collection is due to the mass that accumulates in the probe at the impact pressure of the stream before the solenoid valve is opened. It is important that the collection time be long compared to the initial rise time. For the flow

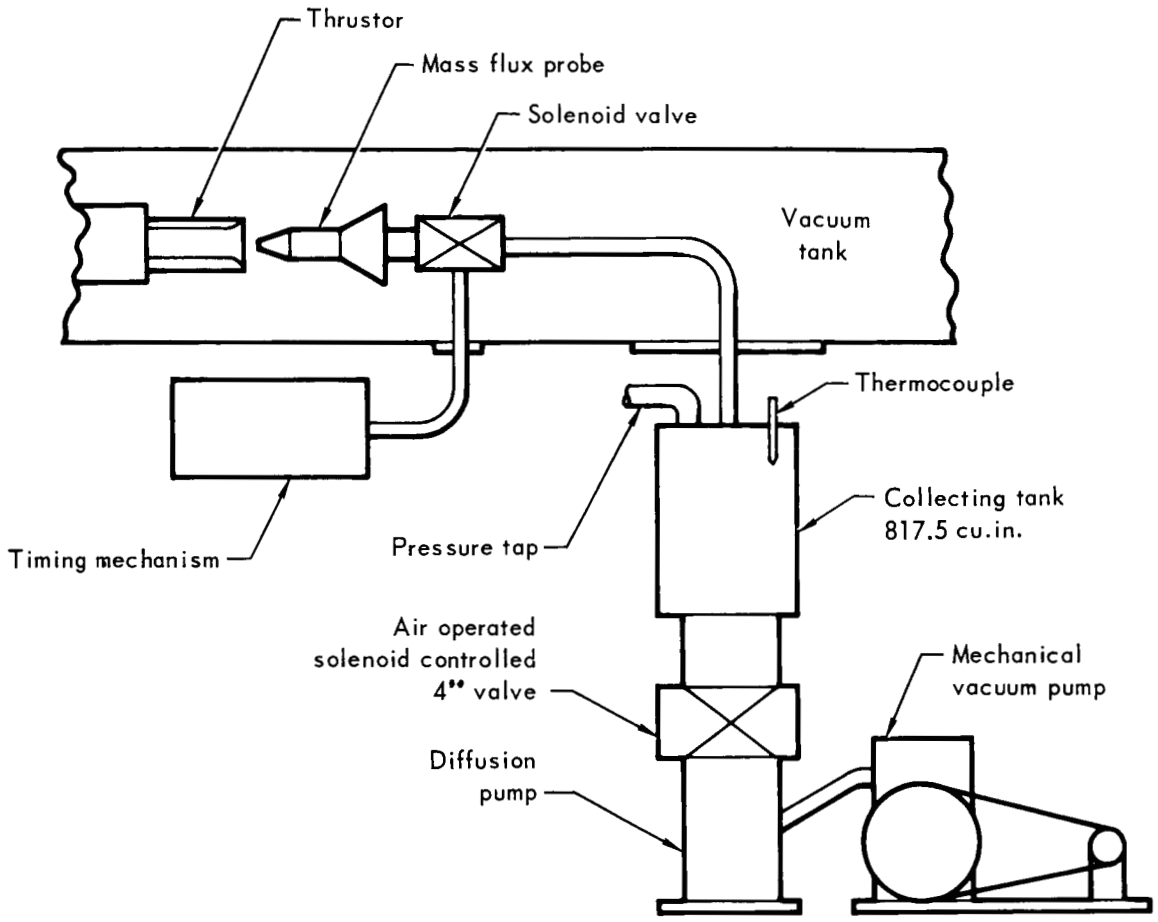

Fig. B–3 Mass flux volume collection apparatus

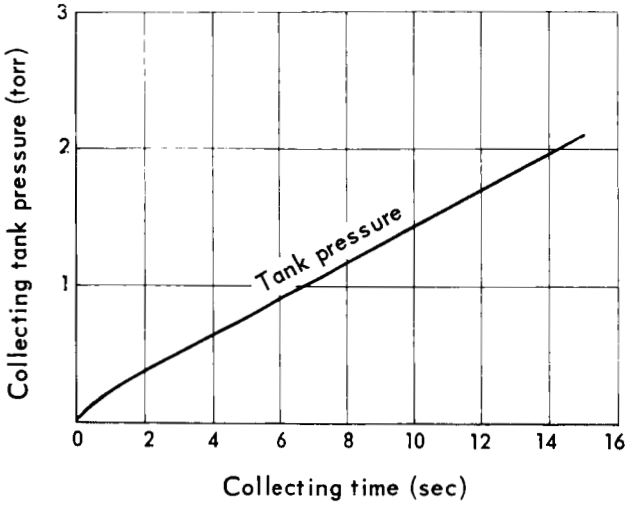

Fig. B–4 Volume collection tank pressure rise

rates encountered in the MAC–4 exhaust, a collection time of approximately 20 seconds reduced the error due to the initial rise to approximately 2%.

The probe was attached to a water-cooled power driven rod which allowed an accurate positioning of the probe at the exit plane and movement across a diameter of the exhaust.

Technique of operation

The following procedure was utilized for the mass flux profile measurements.

- The probe was positioned on the centerline of the arc-jet at approximately 0.020 inch

downstream of the nozzle exit plane by means of a centering plug fitted to the nozzle contour and the probe inlet lip. The centerline position was then recorded on the probe actuator after which the probe was moved out of the exhaust region.

- The test chamber was then sealed, evacuated and the arc-jet started. All instrumentation was monitored to ascertain when a steady state condition of the operating parameters prevailed.
- The probe was then moved into the exhaust region to the position where a mass flux measurement was desired. With the solenoid valve adjacent to the probe closed, the collection tank was evacuated to the 0.5 to 2 micron pressure range. The 4 inch vacuum valve adjacent to the diffusion pump was then closed and the solenoid valve just downstream of the probe opened by means of the digital counting timer. The timing mechanism held the valve open for a predetermined length of time to collect a sample of the flow. The collection time was controlled such that the pressure in the collection tank did not exceed approximately one-third of the impact pressure at any particular position. If the pressure ratio across the probe inlet were not sufficient, then the shock would not be swallowed.
- After the mass sample was taken, the collection time, pressure and temperature are recorded.
- The probe was then moved in increments of 0.05 inch across the exit plane and the procedure repeated. The residence time at each radial position was approximately 3 minutes.

The mass flow through the probe at each radial position was then calculated by Eq. B–2.

Consider a data point 0.3 inch above the arc-jet centerline obtained during a run with a propellant flow rate of 4.0×10^{-4} lb/sec and power input of 30 kW. The temperature in the 876.3 $in.^3$ collection system was $542^{\circ}R$ and the pressure increased 4.07 mmHg in 15.485 seconds. For these dimensional units the mass flow relation may be written as

$$\dot{m} = 2.103 \times 10^{-6} \frac{V\ (in.^3)}{T\ ^{\circ}R} \times \frac{P\ (mmHg)}{t\ (sec)}$$

Then the mass flow for the above data point is

$$\dot{m} = 2.103 \times 10^{-6} \frac{876.3}{542} \times \frac{4.07}{15.485} = 8.936 \times 10^{-7} \text{ lb/sec.}$$

where the initial tank pressure is considered zero.

The mass flux is the mass flow rate ($\dot{m}$) through the probe divided by the inlet area of the probe which was 0.00363 $in.^2$ when the above data was taken. Therefore, the mass flux is 2.46×10^{-4} lb/sec $in.^2$

Results

The results of the mass flux experiments on both GSC–2 and the MAC–4 arc-jet are presented in Section 4.1 of this report.

Error analysis

The mass flux is calculated by

$$\rho u = \frac{m_p}{A_p} = \frac{4K\,V}{\pi\, d_{in}^2\, T} \frac{P}{t} \qquad \text{(B–3)}$$

The estimated uncertainty in each of the measured quantities is as follows.

V = volume of collection tank ± 0.1%
p = tank pressure at end of collection ± 2%
T = temperature of collected sample ± 0.2%
d_{in} = probe inlet diameter ± 1%
t = collection time ± 0.01%

Thus, the total uncertainty in the mass flux measurement is given by:

$$\frac{\Delta\rho u}{\rho u}=\left\{\left(\frac{\Delta V}{V}\right)^2+\left(\frac{\Delta P}{P}\right)^2+2\left(\frac{\Delta d_{in}}{d_{in}}\right)^2+\left(\frac{\Delta T}{T}\right)^2+\left(\frac{\Delta t}{t}\right)^2\right\}^{1/2} \quad \text{(B-4)}$$

and substituting the individual uncertainties into Eq. B–4 results in

$$\frac{\Delta\rho u}{\rho u} = \sqrt{5.05 \times 10^{-4}} = 2.25 \times 10^{-2} \text{ or } 2.5\%.$$

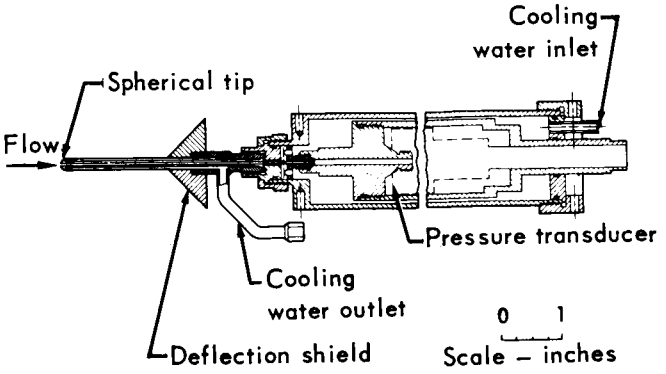

Fig. C–1 Sketch of impact pressure probe

Appendix C Impact pressure probe

A water-cooled impact pressure probe was designed and fabricated for obtaining arc-jet impact pressure profiles at the nozzle exit plane. For high Mach number flows, it can be shown that the impact pressure is approximately equal to the momentum flux of the flow. Thus, the integral of the impact pressure over the nozzle exit plane should compare closely to the measured thrust.

Apparatus

An impact pressure probe (Fig. C–1) was designed and fabricated with two interchangeable tips. One tip is spherical and the other is flat faced. Both tips have a 0.250 inch outside diameter and a 0.048 inch inlet diameter. The tips were machined from solid copper stock and the first braze joint is about a half inch from the nose tip. The probe is completely water-cooled. A pressure transducer enclosed within the probe assembly was used to measure the impact pressure of the MAC–4 and MAC–5 arc-jets. A pressure gauge was used outside of the vacuum tank in place of the transducer when impact pressures were obtained for the GSC–2 arc-jet.

The probe was moved across the arc-jet nozzle exit plane by a motor driven screw actuator. It may be stopped at any position. A slide wire position indicator was incorporated so that the probe position and pressure could be recorded on an oscillograph trace.

Technique of operation

The probe was mounted on the actuator so that its tip was approximately 0.020 inch from the nozzle exit plane. Initially, the impact pressure profiles were obtained by taking data points at 0.010 inch increments. In order to obtain finer detail near the nozzle walls, the slide wire position indicator was added and a continuous sweep was made across the nozzle exit plane. A stop was required at each data point for the GSC–2 arc-jet pressure profile because of the slow response of the pressure gauge.

Results

The impact pressure profiles obtained with the flat faced tip on both the water-cooled MAC–4 and GSC–2 arc-jets are presented in Section 4.2 of this report. A number of profiles were obtained with the spherical tip which essentially duplicated the flat faced tip measurements. Figure C–2 presents a typical comparison of the data obtained with the two probe tips. The change of slope of the pressure distribution near the wall is more pronounced with the flat faced tip and is probably due to the "cornering" of the flow as the outer diameter of the probe nears the nozzle wall. This effect should be reduced with a spherically tipped probe.

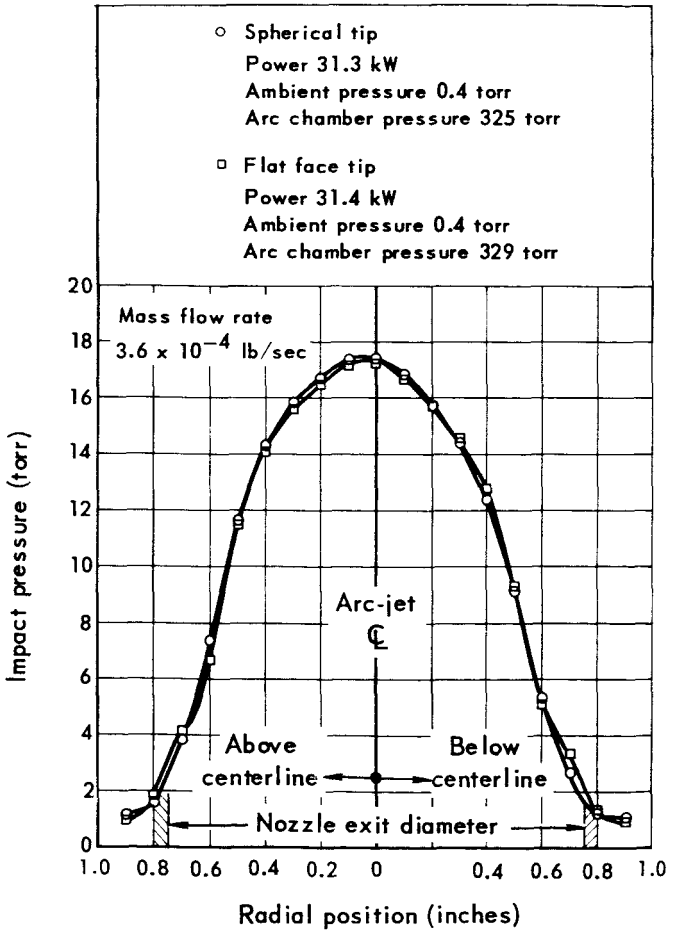

Fig. C–2 Effect of probe tip on impact pressure profile (MAC–4 arc-jet)

Error analysis

The uncertainty in the impact pressure measurements is just the uncertainty in the pressure transducer or pressure gauge. The uncertainty in the 0–50 torr pressure gauge used for the GSC–2 arc-jet measurements was ±0.5% since the pressures were near the full scale reading. The uncertainty in the 0–1 psia pressure transducer used for the MAC–4 arc-jet measurements was ±2%.

Appendix D Photometric velocity meter

The objective of this study was the investigation of the feasibility of determining the exhaust gas velocity profile of a hydrogen arc-jet by photometrically sensing the light fluctuations inherent in the luminous plasma flow.

A general characteristic exhibited by all arc-generated plasma streams observed in this laboratory is the existence of random fluctuations in the intensity of the light emitted from the plasma. This characteristic has been observed in the arc and exhaust regions of hydrogen, argon, nitrogen, and air plasmas generated by a variety of arc-jets and arc-heaters. The frequency spectrum of the fluctuations consists of a large component at 360 cycles/sec which is due to the characteristic power supply ripple and a continuous spectrum from near kc/sec to approximately 120kc/sec. The relative magnitude of the continuous component decreases with frequency in a nearly exponential manner.

The generation mechanism for the high frequency fluctuations is not presently understood; however, if the fluctuations propagate at the speed of the gas stream, then a measurement of the propagation velocity would be indicative of the exhaust stream velocity. The propagation velocity is determined by sensing the fluctuations at two fixed stations in the arc-jet exhaust and determining the

time required for the fluctuation to traverse the known distance between stations. The significant feature of this technique is that the plasma stream is not physically disturbed by the measurement.

Experimental apparatus

A diagram of the velocity meter test arrangement is shown in Fig. D–1. The apparatus is composed of two systems; an optical system, and a signal correlation system. The optical system converts the light fluctuations into an electrical signal and consists of the following:

- Two identical collimating tubes, 2 inches in diameter and 48 inches long.
- Three apertures and a lens are located in each collimating tube. Aperture 1 determines the size of the plasma sample, aperture 2 reduces stray radiation incident through aperture 1, and aperture 3 provides a light source for the lens which distributes the light over the photosensitive cathode of the photomultipliers.
- Two photomultiplier tubes, which are located at the end of the collimating tubes. The photomultiplier tubes have a response range of 3000 to 7500 angstrons with a maximum radiant sensitivity of 0.6 amp/μwatt at 4200 angstroms.

The signal correlation system consists of two identical channels which receive the photomultiplier output signals. The two signals are filtered and amplified and then applied to an analog signal

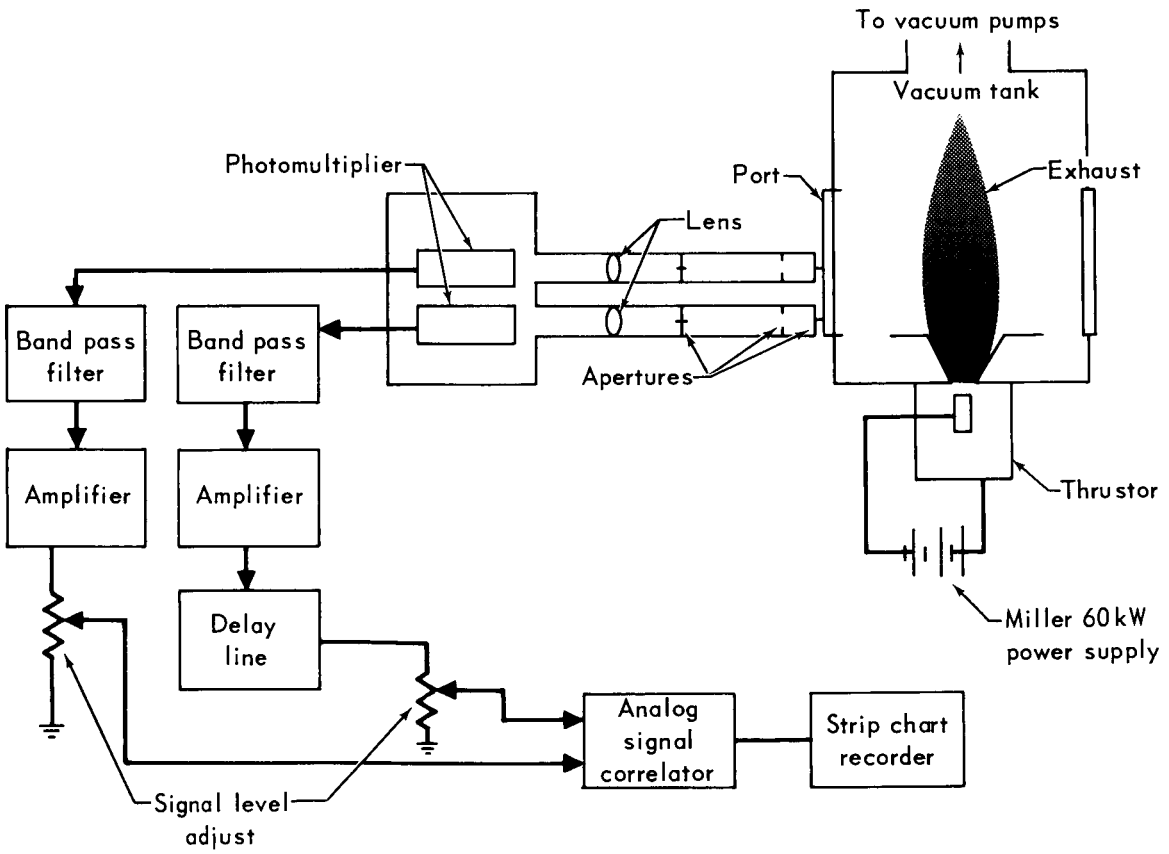

Fig. D–1 Velocity meter experimental apparatus

correlator. The correlation system consists of the following components;

- Two continuously variable pandpass filters with frequency response of 20 cycles/sec to 200 kc/sec. The upper and lower cutoffs are independently adjustable. These filters have matched phase characteristics.
- Two amplifiers with closed loop gain of approximately 40 with AGC circuits. These AGC circuits compensate for input variations to give a constant rms output signal level.
- A continuously variable delay line of 0 to 12 microseconds with 0.1 microsecond resolution.
- A true root-mean-square voltmeter for monitoring signal strength.
- An analog signal correlator with frequency response of 5 to 100 kc/sec, This unit may be operated in a Cos θ, cross correlate, or auto-correlate mode.
- A pen recorder for recording the correlator output.

A photograph of the test equipment is shown in Fig. D–2. The optical system is mounted on an adjustable platform which permits vertical translation for viewing different regions of the arc-jet exhaust. An angular adjustment of the downstream collimating tube is also provided for sighting along expanding streamlines.

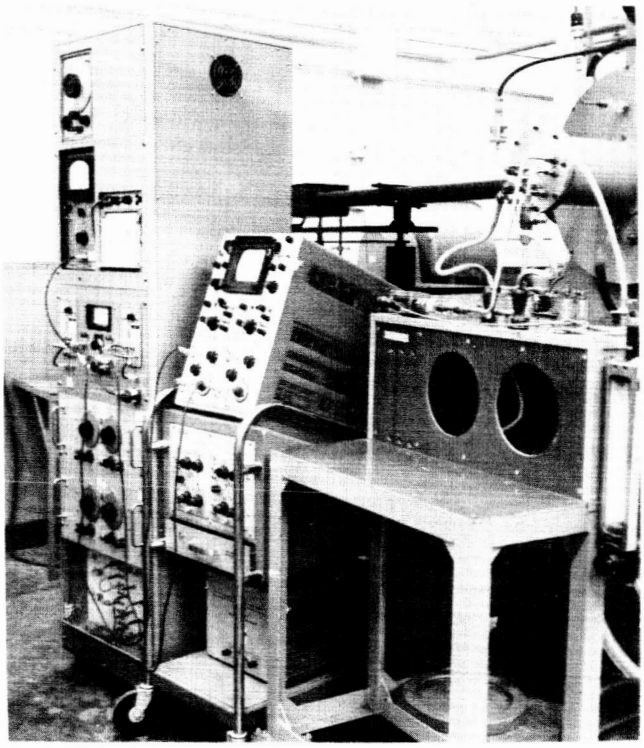

Fig. D–2 Velocity meter apparatus

Technique of operation

Prior to operation the velocity meter is located perpendicular to the exhaust stream and the upstream collimating tube is sighted across a diameter approximately 0.1 inches downstream of the arc-jet nozzle exit. The separation distance between viewing stations is determined by moving a small dc lamp along the centerline of the exhaust region past the viewing area of the collimators by means of a precision cross slide milling table. This procedure accurately defines the viewing area of each tube at the centerline and also the separation between viewing stations.

In operation, the frequencies between 20 and 100 kc/sec are divided into bands. The selection of these bands are made by means of the variable band pass filters. With the arc-jet operating and the correlator operating in a cross correlate mode, the RMS level of each photomultiplier output through the band pass filter is adjusted so that the signal strengths applied to the correlator inputs are equal. The delay line is varied in the phase leading input until the correlator output passes th through a maximum. This procedure will define a cross correlation curve which mathematically may be expressed as (Ref. 11):

$$R_{xy}(\tau) = \frac{1}{2T}\int_{-T}^{T} x(t)\, y(t+\tau)\, dt \qquad (D-1)$$

where $R_{xy}(\tau)$ = cross correlation function

$x(t)$ = signal input A

$y(t)$ = signal input B

τ = magnitude of time delay

The period $-T$ to $+T$ is the correlator integration time (approximately three seconds), and τ, the delay time, is varied in the range of 0 to 12 microseconds. A typical curve defined by this process will be

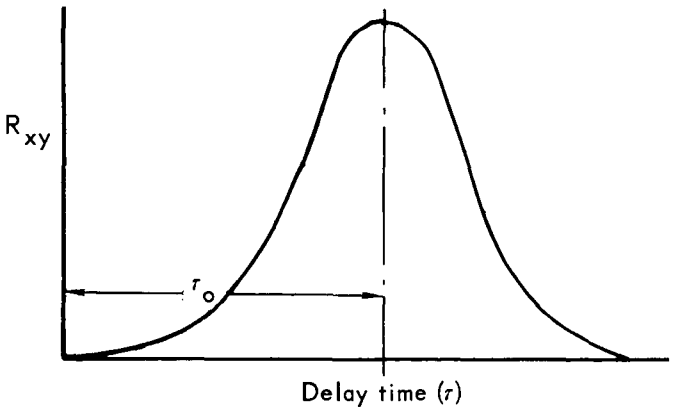

As the two signals are brought "in phase" by varying τ, $R_{xy}(\tau)$ will pass through a maximum. This value is designated τ_o. on the figure. This procedure is repeated for all frequency bands in which the fluctuation power spectral density is sufficient to give at least a minimum signal strength at the correlator inputs.

Signal auto-correlation is achieved with a single (upstream) photomultiplier output. The auto correlation is performed in the same frequency bands at which the cross correlation output was performed. This function, mathematically expressed is:

$$R_{xx}(\tau) = \frac{1}{2T}\int_{-T}^{T} x(t)\, x(t+\tau)\, dt \qquad (D-2)$$

where $R_{xx}(\tau)$ = auto correlation function
$x(t)$ = signal input A applied to both correlation inputs
τ = magnitude of time delay

A typical curve defined by this process will be:

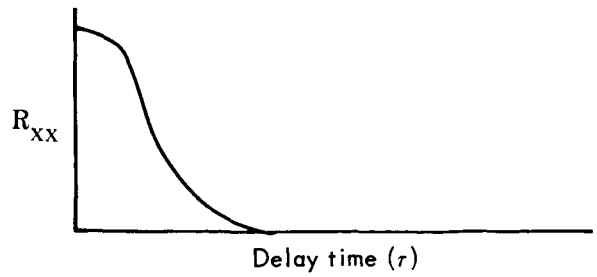

When auto correlating, the signals are "in phase" at $\tau = 0$ and therefore, $Rxx(\tau)$ is maximum at $\tau = 0$.

The above auto-correlation cross-correlation procedure is usually repeated for the frequency bands in which the fluctuation power spectral density is sufficient to give at least a minimum signal strength into the correlator. The cross correlation functions are then plotted on a graph versus time delay to determine the peak of the curve.

The velocity of propagation of the light intensity fluctuations which is assumed to be the stream velocity is computed from the equation

$$u = d/\tau_o \qquad (D-3)$$

where u = velocity (ft/second)
d = aperture gap separation (feet)
τ_o = time delay at maximum cross correlate output (μsec)

Together the auto-correlation and cross-correlation functions define an index of signal similarity at each frequency band. This index of signal similarity is defined by

$$I = \frac{R_{xy}(\tau = \tau_o)}{R_{xx}(\tau = 0)} \qquad (D-4)$$

System Calibration

The experimental determination of the traversal time (τ_o) requires that the two signals received at the correlator input correctly describe the variation of light intensity with time. Thus

it is imperative for meaningful results that the two channels composed of photomultipliers, filter and amplifiers do not time shift the signals.

A calibration of the velocity meter apparatus was obtained utilizing a Kerr Cell to provide a 10 to 60 kc light source. The arrangement for the Kerr Cell bench tests is shown in Fig. D–3. A single light source was passed through the Kerr Cell to both velocity meter channels thus supplying an "in-phase" lifht signal to each photomultiplier. Cross-correlation and signal similarity data were then measured to determine phase shift and signal degradation characteristics of the equipment.

The results of this investigation indicated that for certain gain settings and tube supply voltages the photomultiplier tubes were overdriven causing a relative phase shift of the signals. In addition, noise generated in the phototubes caused some signal degradation. This signal degradation was variable and dependent upon the amount of light striking the photomultiplier cathode.

This investigation established the operating envelope of the apparatus over which the relative phase shift of the two channels was zero.

Velocity measurements

Propagation velocity measurements were obtained on a 30 kW radiation arc-jet (MAC–3), a water-cooled arc-jet (MAC–4) and the regeneratively-cooled arc-jet (GSC–2).

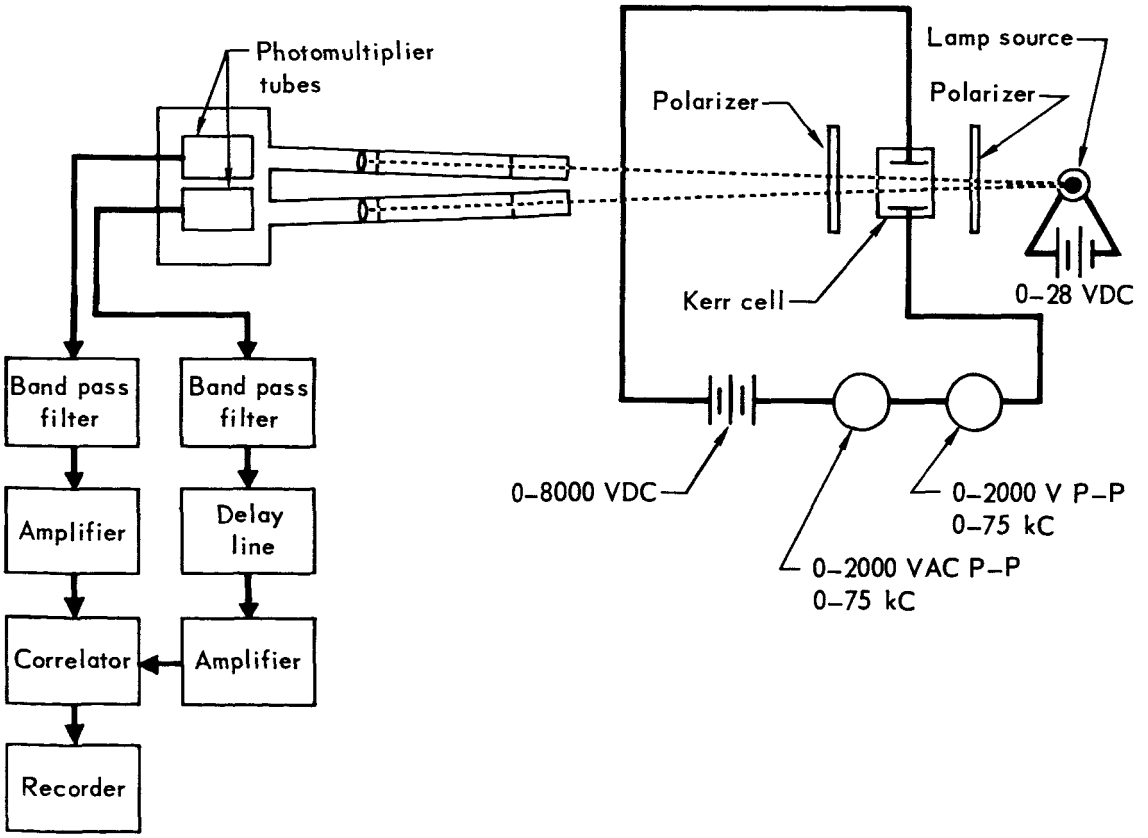

Fig. D–3 Experimental arrangement for Kerr-cell calibration

MAC–3 Arc-jet

Five centerline velocity measurements were obtained on this arc-jet which are presented in Table D–1.

Table D–1 Velocity meter data on MAC–3 arc-jet

Exit bulk stagnation enthalpy (B/lb)	Band pass (kc/sec)	Index of signal similarity I_{xy} (dimensionless)	Delay time at max, R_{xy} (τ_o) (microseconds)	Calculated centerline (ft/sec)
51,000	39–49	0.78	3.15	43,000
51,000	61–75	0.83	3.40	40,000
51,000	75–95	0.83	3.38	39,900
64,000	39–49	0.65	2.60	52,500
64,000	61–75	0.74	2.70	50,400

The cross correlation function versus delay time had a well defined maximum and allowed a determination of τ_o to the nearest 0.02 microsecond. The index of signal similarity determines how accurate the value of τ_o can be ascertained.

MAC–4 arc-jet

Figures D–4 through D–8 depict velocity profile data on the MAC–4 arc-jet for power levels of 21.4, 21.0, 26.6, 31.4, and 36.5 kW at flow rates of 4.0×10^{-4} and 4.5×10^{-4} lb/sec. Calculated velocity profiles obtained from measurements of the mass flux and momentum flux profiles (Sect. 4.3) are also plotted on Figs. D–4 through D–8 for comparison purposes. The velocity meter data is generally lower on the centerline and exhibits greater scatter than the probe data.

The data scatter is attributable to the low index of signal similarity measured on this arc-jet. Figure D–9 is a plot of index of signal similarity for various arc powers and mass flow rates. Velocity data could not be obtained at conditions where

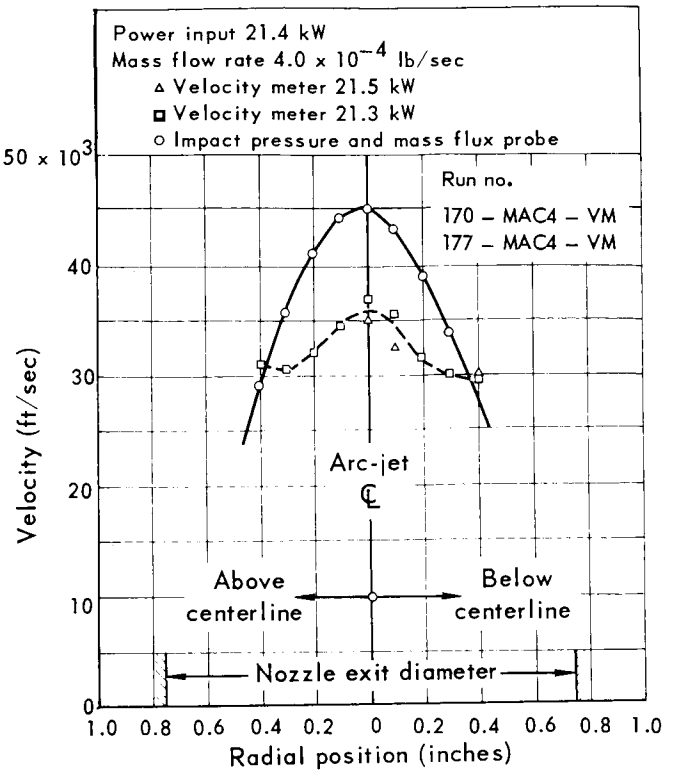

Fig. D–4 Velocity profile on MAC–4 water-cooled arc-jet

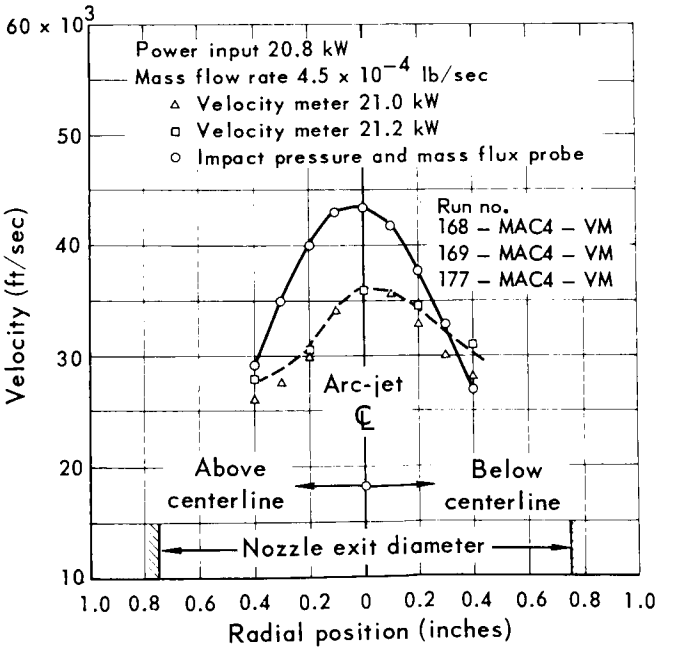

Fig. D–5 Velocity profile on MAC–4 water-cooled arc-jet

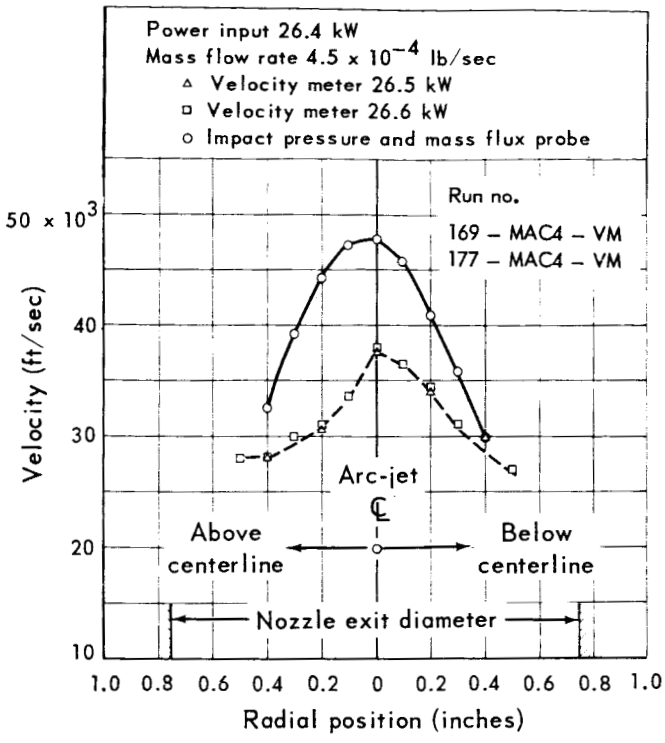

Fig. D–6 Velocity profile on MAC–4 water-cooled arc-jet

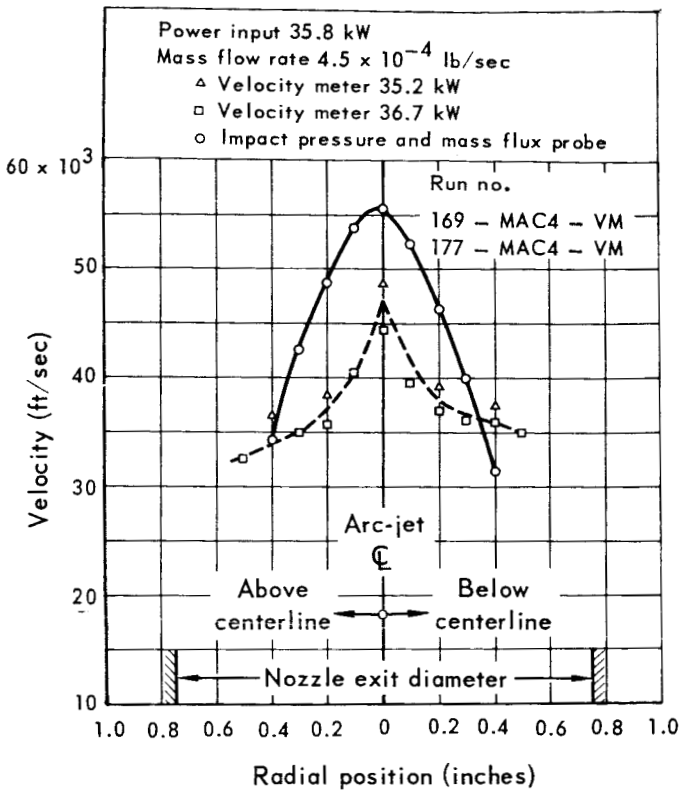

Fig. D–8 Velocity profile on MAC–4 water-cooled arc-jet

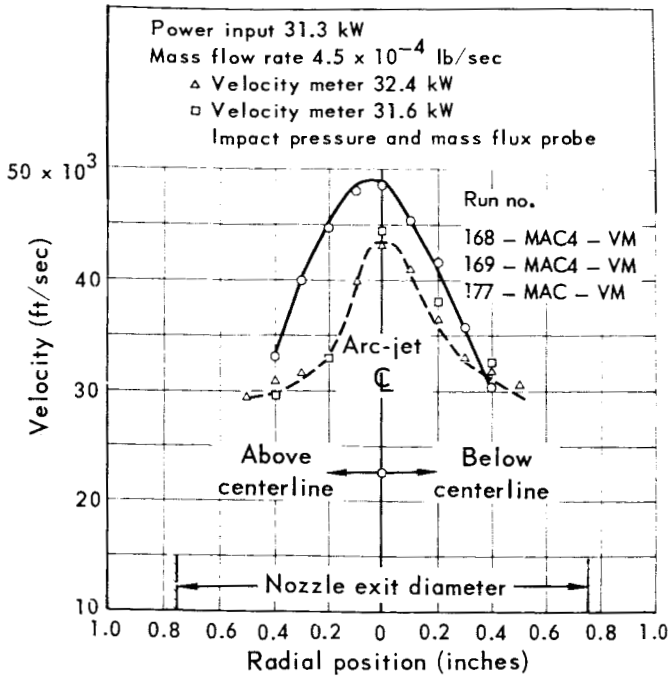

Fig. D–7 Velocity profile on MAC–4 water-cooled arc-jet

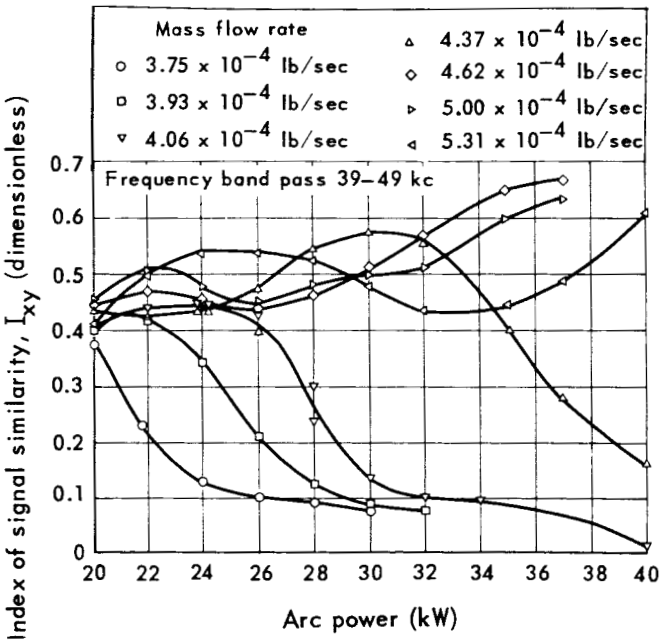

Fig. D–9 I_{xy} vs arc power on MAC–4 water-cooled arc-jet

I_{xy} was less than 0.4 since the cross-correlation functions did not maximize sharply. It is noted that low values of I_{xy} are in some part due to degradation caused by photomultiplier noise however, I_{xy} is very sensitive to the arc-jet operating parameters.

GSC–2 arc-jet

Figures D–10 and D–11 present the velocity profiles obtained on the GSC–2 arc-jet for power levels 28.3 and 31.3 kW respectively at a mass flow rate of 7.4 x 10^{-4} lb/sec. The centerline velocities for 28.3 kW power level range from 46,000 to 51,700 ft/sec giving a mean percentage deviation of ±5.2%. The centerline velocities for the 31.3 kW power level range from 47,100 to 51,600 ft/sec giving a mean percentage of ±4.6% The average centerline velocities for the 28.3 and 31.3 kW power levels are 48,900 and 49,300 ft/sec respectively. This gives a velocity difference of 400 ft/sec between the two power levels According to specific impulse data, there should be an average velocity difference of 1000 ft/sec. The measured velocities therefore, show no significant dependence or power.

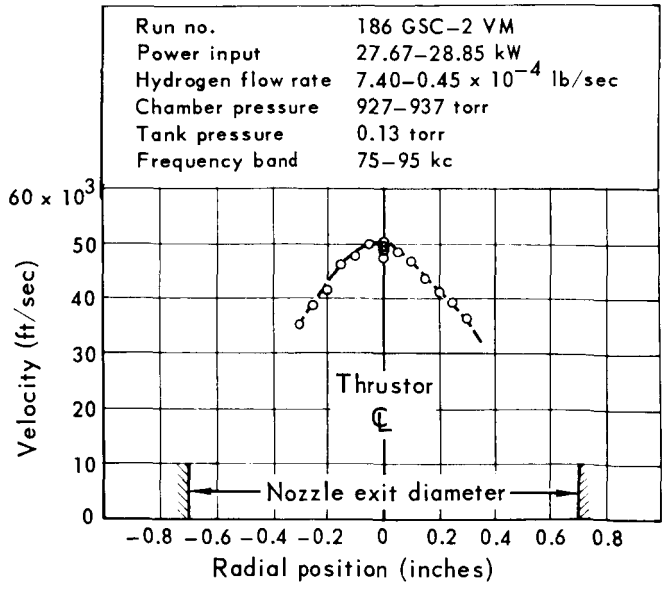

Fig. D–10 Velocity profile on GSC–2 arc-jet

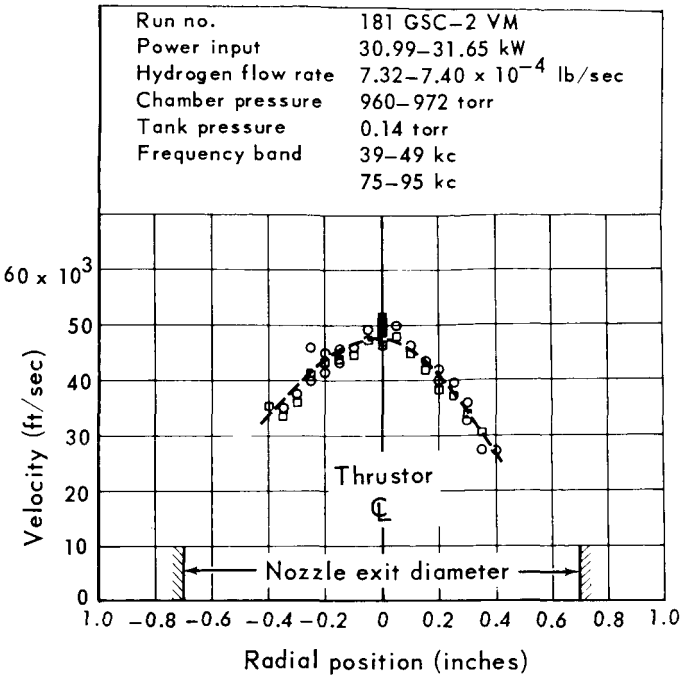

Fig. D–11 Velocity profile on GSC–2 arc-jet

The mass flux and momentum flux profiles measured on the GSC–2 arc-jet were combined to give a velocity profile. Figure D–12 shows this profile and also a smooth curve of the measured velocity meter data for the 31.3 kW operating condition. The velocity meter data is higher than calculated data by 10,500 ft/sec at the centerline and 5,200 at 0.4 inches off centerline. The vacuum specific impulse measured for this operating condition was 970 sec. Since the actual specific impulse may be from 2 to 4% lower than the vacuum specific impulse the average velocity of the exhaust should be between 30,600 and 30,000 ft/sec. The average velocity of each of the profiles presented in Fig. D–12 can obtained.

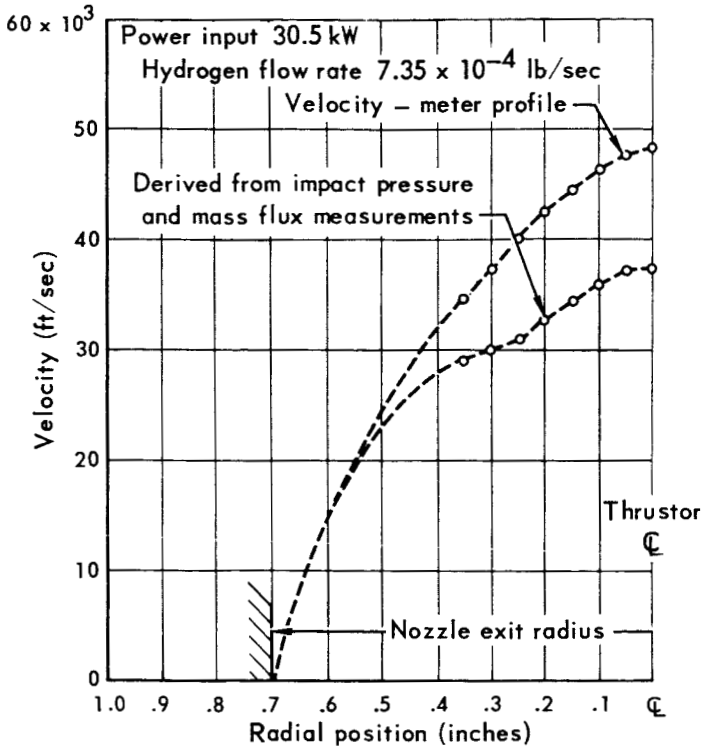

Fig. D–12 Calculated velocity profile on GSC–2 arc-jet

$$\bar{u} = \frac{2\pi \int_0^{r_o} (\rho u)\, u\, dr}{2\pi \int_0^{r_o} \rho u\, dr} \qquad (D-5)$$

where $\bar{u}$ = average velocity

u = local velocity

ρu = mass flux

r_o = nozzle exit radius

The average velocity was calculated by this relationship using the measured mass flux profile and extrapolating the two curves to zero at the nozzle radius as shown. The average velocity of the velocity meter profile was 34,800 ft/sec, and 29,300 ft/sec for the profile calculated from the probe data. Thus, it appears that the calculated profile satisfies the average velocity condition better than the velocity meter data.

The index of signal similarity for GSC–2 measurements were considerably higher than for the MAC–4 arc-jet ranging from 0.85 to 0.98.

Arc-jet light fluctuation frequency analysis

A series of power spectral density (PSD) measurements of the inherent light fluctuations emanating from the arc-jet exhaust were made to establish the relative magnitude of the various frequencies present. The data were obtained by recording the phototube signal output on tape and then performing a power spectral density analysis. The phototube was sighted at the intersection of the nozzle exit plane and the centerline axis of the exhaust. The range of frequencies recorded was 4 to 200 kc/sec.

MAC–4 arc-jet

Figure D–13 presents the (PSD) analysis obtained on the MAC–4 arc-jet for power inputs of 20, 25, 30, and 35 kW for a mass flow rate of 3.6 x 10^{-4} lb/sec. The relative magnitude of each frequency component decreases nearly exponentially as the frequency is increased and increases as the power level is increased. This plot is

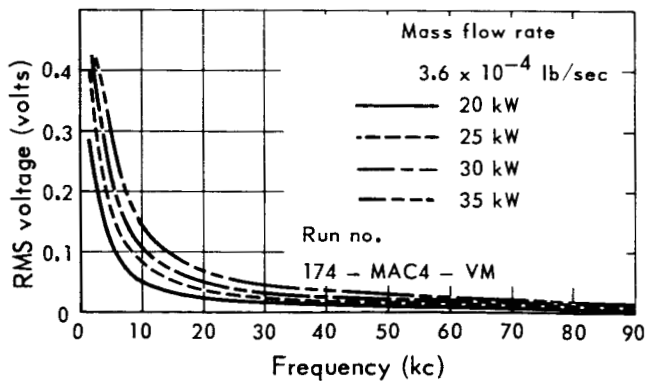

Fig. D–13 Centerline power spectral density analysis of MAC-4 arc-jet

representative of the (PSD) analyses obtained at different flow rates on the MAC–4 arc-jet. The characteristic shape is also typical of other arc-jet thrustors where the arc passes through the nozzle throat.

GSC–2 arc-jet

Figure D–14 presents the (PSD) analysis taken on the GSC–2 arc-jet for power inputs of 24.6, 27.6, and 31.4 kW respectively at a tank background pressure of 0.18 torr and a hydrogen flow rate of 7.4×10^{-4} lb/sec. As shown there are 3 peaks in the (PSD) curve that are integer multiples of the lower peak frequency and these peaks are shifted as a function of power input.

A (PSD) analysis of the signal after the filters also contain the peak components. To determine the effect of background pressure on the (PSD) analysis the background pressure was raised to 0.29 torr at a power input of 30.8 kW. Figure D–15 shows the effect of background. The slight shift is mostly due to thrustor warm-up since the lower background test was made just after "light-off" and the higher background test was made some 20 minutes later.

Several tests were made with argon, helium, and nitrogen as the propellant to discern the effect of molecular weight changes on the GSC–2 frequency spectrum. The operation times were held short (1 to 2 minutes) so that the thrustor would not be damaged due to the lower cooling capacities of these gases compared to hydrogen. The (PSD) analyses for argon and helium showed

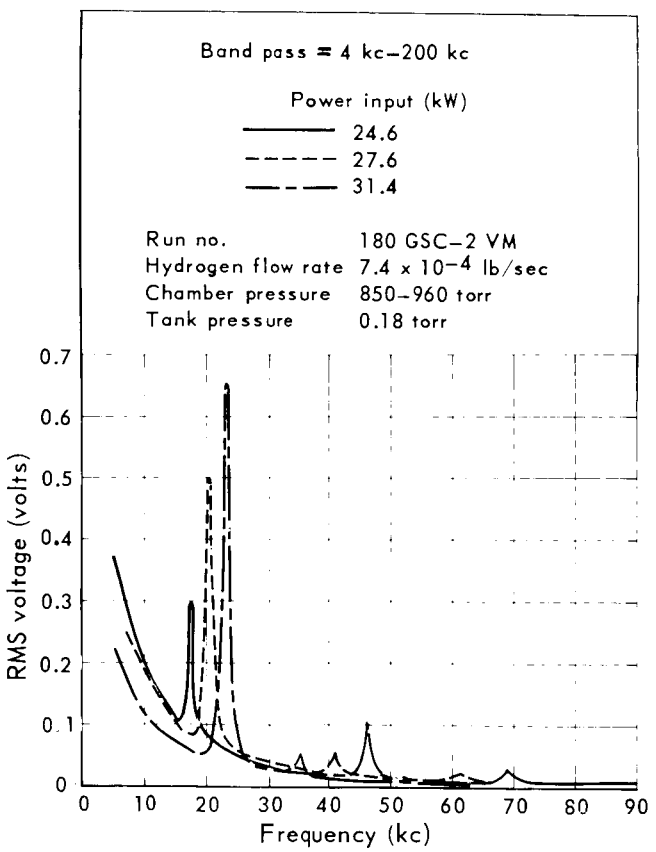

Fig. D–14 Centerline power spectral density analysis of GSC–2 hydrogen arc-jet

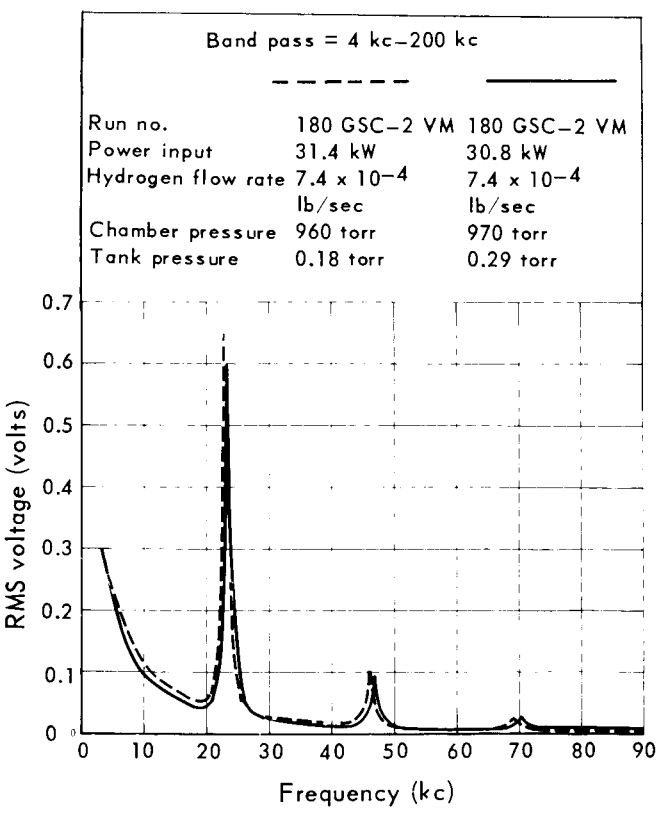

Fig. D–15 Centerline power spectral density analysis of GSC–2 hydrogen arc-jet

no peaks however, these peaks were observed during nitrogen operation as shown in Fig. D-16. The fundamental frequency occurred at 4.4 kc/sec and the harmonics were all integer multiples of the fundamental frequency.

The fluctuations in the arc voltage of the GSC–2 arc-jet were recorded with an oscilloscope (Fig. D-17) for power inputs of 23.9, 25.9, and 29.5 kW for a hydrogen flow rate of 7.4 x 10^{-4} lb/sec. The magnitude and frequency of the fluctuations are the same as observed on the PSD recordings. The magnitude of these fluctuations are large (200 volt peak to peak).

Analysis of the results of the GSC–2 experiments suggest that the peaks in the PSD analysis are a result of some acoustic-like disturbance in the arc chamber. The harmonics occurring at integer multiples of the fundamental frequency indicate that this acoustic disturbance is in the resonance in the arc chamber similar to a closed tube in resonance. The increase in fundamental frequency with increasing power supports the above argument since the speed of sound increases as the effective arc chamber temperature is raised due to a power increase. The fluctuations in arc voltage should be coupled in frequency to any acoustic disturbance in the arc chamber since the arc voltage is quite sensitive to the

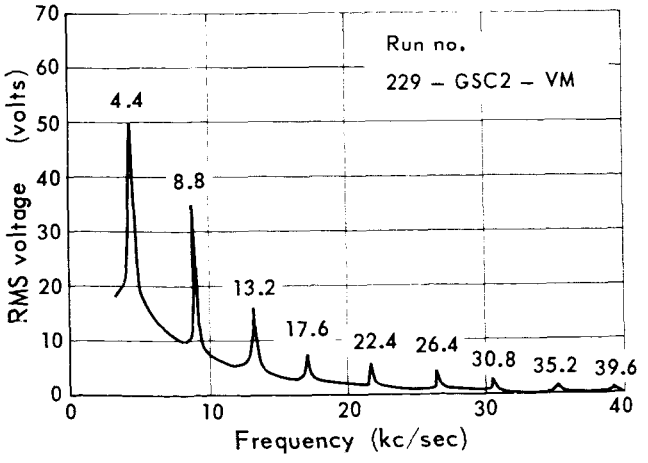

Fig. D–16 Centerline power spectral density analysis of GSC–2 nitrogen arc-jet

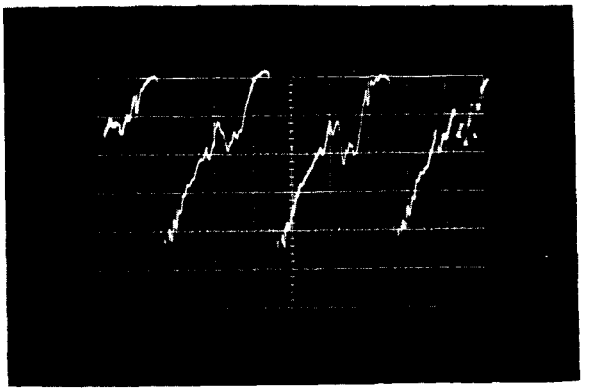

Power = 23.9 kW
50 volts/cm
20 μ sec/cm

Power = 25.9 kW
50 volts/cm
20 μ sec/cm

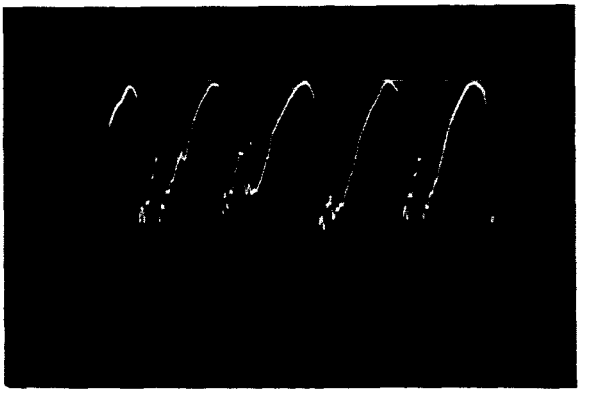

Power = 29.5 kW
50 volts/cm
20 μ sec/cm

Fig. D–17 Arc voltage fluctuations in the GSC–2 arc-jet

chamber pressure. The observations that the background pressure does not change the frequency of the peaks also suggests that the disturbances are occurring in the arc chamber. The effect of molecular weight is also consistent with acoustic resonance picture since an increase in molecular weight should decrease the fundamental frequency. The fundamental frequency observed during hydrogen operation was 17.5 kc/sec at 24.6 kW and if it assumed that the temperature in the arc chamber during the nitrogen and hydrogen test was the same, then hydrogen fundamental should be related to the nitrogen fundamental as:

$$f_{N_2} = \left(\frac{M_{H_2}}{M_{N_2}}\right)^{1/2} f_{H_2} \qquad \text{(D–6)}$$

where f_{N_2} = fundamental frequency of nitrogen

f_{H_2} = fundamental frequency of hydrogen

M_{N_2} = molecular weight of nitrogen

M_{H_2} = molecular weight of hydrogen

Assuming also that both gases are completely disassociated then:

$$f_{N_2} = \left(\frac{1}{14}\right)^{1/2} 17.5 = 4.7 \text{ kc/sec}$$

The measured nitrogen fundamental of 4.4 kc/sec is in good agreement in view of the assumptions made. The lack of the resonant phenomena for argon and helium is not presently understood; however, the existence of the resonant condition may depend on the total arc voltage which for hydrogen and nitrogen was above 150 volts but for argon and helium was between 50 and 70 volts.

Discussion of results

The results of the velocity meter measurements on the MAC–4 arc-jet indicate that for this thrustor the propagation velocity of the light fluctuations is the same as or close to the local jet velocity. The comparisons of the velocity meter profiles with the calculated profiles, which are considered the correct velocity profiles, were in relatively good agreement. The majority of the velocity meter data were within 20% of the calculated data. Some of the deviation is due to the fact that the velocity meter does not "see" a point in the plasma but rather a cross section. Thus, the velocity that is measured represents an "average" over the view region. It is most likely that this "average" is weighted with respect to the local light intensity over the section of plasma observed. Consequently, if the actual velocity profile is peaked on the centerline, the velocity meter profile should be less peaked because of the "averaging" process, as is the case.

The results of the velocity meter measurements on the GSC–2 arc-jet yielded a profile considerably above the calculated profile which agreed well with the specific impulse value and is considered quantitatively correct. The (PSD) analysis of the GSC –2 arc-jet revealed the existence of large resonant peaks, characteristic of an acoustic disturbance in resonance with the arc chamber. In view of the above, it is suggested that the propagation velocity of the light fluctuations as measured by the velocity meter is equal to the local jet velocity plus the local sonic speed. The major component of the signal received by the velocity meter phototubes was composed of the peak even after filtering and since the peaks are believed to be caused by acoustic disturbances then it is reasonable to suspect that the fluctuations are propagating at the acoustic speed with respect to the local gas velocity.

This argument explains the difference between the velocity meter profile and the calculated profile since a subtraction of the sonic velocity would bring the two profiles in close agreement.

Error analysis

The uncertainty in the propagation velocity due to inherent uncertainties of the measured traversal time and separation distance is

$$\frac{\Delta u}{u} = \left[\left(\frac{\Delta \tau_o}{\tau_o} \right)^2 + \left(\frac{\Delta d}{d} \right)^2 \right]^{1/2} \qquad (D-7)$$

The accuracy of the separation distance measured was ±1%. The accuracy of the traversal time measurement is a function of how well defined is the maximum of the cross-correlation function, which in turn is related to the index of signal similarity.

For the MAC–4 arc-jet the index of signal similarity was low ($0.40 < I_{xy} < 0.75$) which resulted in an estimated accuracy of the traversal time of ±7%. Thus, for the MAC–4 arc-jet

$$\frac{\Delta u}{u} = \sqrt{50 \times 10^{-4}} = 7.06 \times 10^{-2} \text{ or } 7\%$$

For the GSC–2 arc-jet, the range of I_{xy} was 0.85 to 0.98 which improved the accuracy of the traversal time to ± 2%.

Thus for the GSC–2 arc-jet,

$$\frac{\Delta u}{u} = \sqrt{5 \times 10^{-4}} = 2.24 \text{ or } 2\tfrac{1}{4}\%$$

Conclusions

The results of the photometric velocity experiments indicate:

(1) A measurement of the propagation velocity of the light fluctuations can be used to infer the gas exhaust velocity.

(2) The thrustor characteristics (most probably the arc chamber geometry) determine the relationship between gas exhaust velocity and propagation velocity.

(3) The propagation velocity is the same as or very close to the gas velocity for the water-cooled arc-jet of the constricted arc design (MAC–4). The velocity meter technique provided velocity profile measurements within 20% of the actual gas velocity profile.

(4) The propagation velocity is equal to the sum of the local jet velocity plus the local sonic speed, for the regeneratively-cooled arc-jet (GSC–2). The propagation velocity measured on this arc-jet is considered accurate to ±5%.

Appendix E Stagnation enthalpy probe

The purpose of this work was the development of a device capable of measuring the local stagnation enthalpy profile in the exhaust of a 30 kW hydrogen arc-jet.

A calorimetric device was chosen to accomplish these measurements which consists of a hollow tube probe through which a sample of the supersonic stream is collected. The sample is cooled within the probe to near room temperature and then passed out of the probe through a sonic flow nozzle. The total energy per unit time entering the probe is accounted for by measuring the temperature rise and flow rate of the probe cooling water and the total temperature of the exiting gas. The mass flow rate of gas collected by the probe is obtained through a measurement of the gas temperature and pressure upstream of the sonic flow nozzle.

A knowledge of the total energy per unit time and the gas flow rate is sufficient to define the stagnation enthalpy of the collected sample. The product of stagnation enthalpy and mass flux will define the total power flux of the flow and an integration of the local power flux profile over the nozzle exit plane areas will give the total power in the exhaust flow at the exit plane location.

A check of the enthalpy measurements can be obtained by comparing the integrated value of power in the exhaust flow with independent measurements of the power input and power losses to the thrustor. Assuming cylindrical symmetry, the following equation should be satisfied if the enthalpy measurements are correct.

$$P_{in} - P_{loss} = 2\pi \int_{o}^{r_o} \rho u\, h_t\, r\, dr \qquad (E-1)$$

where P_{in} = power input (B/sec)

P_{loss} = power losses (B/sec)

u = local mass flux at nozzle exit plane (lb/sec-in.^{2})

h_t = local stagnation enthalpy at nozzle exit plane (B/lb)

r_o = nozzle exit plane radius (in.)

Experimental apparatus

Figure E–1 is a drawing of the stagnation enthalpy probe. This probe design evolved from previous developmental work on an enthalpy probe carried out under NASA contract NAS3–3562 reported in Ref. 9. The probe consists of two cooling systems, an internal cooling system in which the captured gas is cooled and its energy content and mass flow rate are measured and, an external cooling system which shields the internal system from the exhaust environment.

The internal cooling system is composed of an inlet tube, a sonic flow nozzle and an internal probe body. The copper inlet tube is double-walled with water flow dividers leading to the conical lip. The inlet lip diameter is 0.075 inches and has an external half angle of 20° and an internal half angle of 5°. The sonic flow nozzle is fabricated from type 321 stainless steel and has a throat diameter of 0.060 inches. The sonic flow nozzle is instrumented with a pressure port and three chromelalumel thermocouples for measurement of the upstream pressure and temperature. Figure E–2 presents the mass flow calibration as a function upstream pressure and temperature for the sonic flow nozzle. This calibration was performed by the McDonnell Calibration Laboratory and was obtained with a G.K. Porter 70 cc. positive displacement flowmeter. The estimated accuracy of mass flow calibration was ±3% of the mass flow. The internal probe body accepts both the inlet and outlet

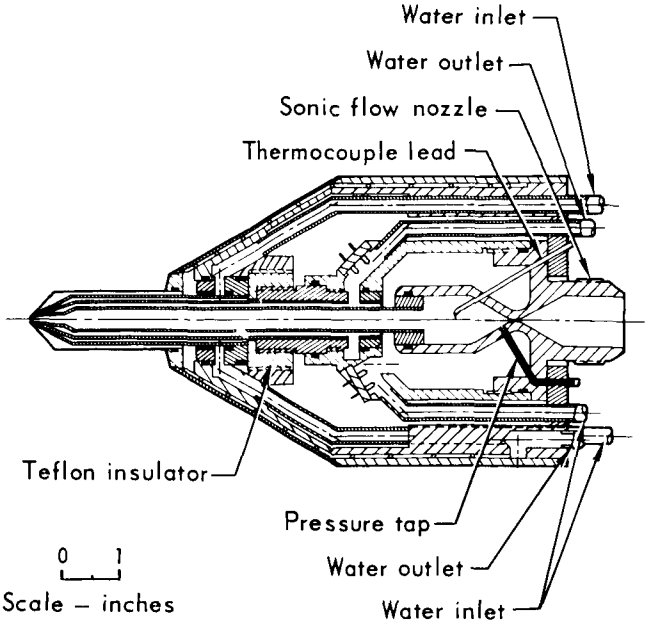

Fig. E–1 Total enthalpy probe

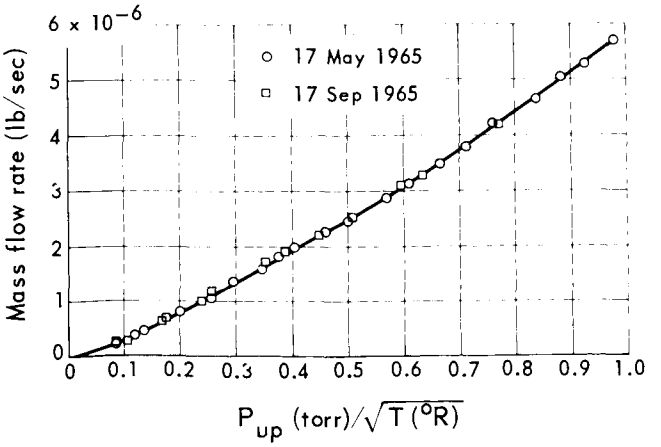

Fig. E–2 Calibration of the enthalpy probe nozzle meter

water and is instrumented with a three thermocouple junction in each water passage. The thermocouples are connected in series to form a thermopile and are used to obtain the rise in the cooling water temperature. The cooling water flow rates are recorded with conventional rotometer gauges located outside of the vacuum tank.

The external cooling system is connected to the internal system by means of a threaded teflon sleeve and completely surrounds the internal system. This system has a replaceable tip which consists of a double-walled cylinder with water flow dividers leading to the conical lip. The copper lip inlet diameter is 0.076 inches and has an external half angle of 45^{o} and an internal half angle of 30^{o}.

During assembly the internal system is threaded into the external system until electrical continuity is established. This occurs as the two inlet lips come in contact; the internal system is then withdrawn slowly until continuity is broken. This procedure ensures that there is no direct thermal conduction path between the two systems.

An actuator mechanism was designed and fabricated to accurately position the enthalpy probe in the arc-jet exhaust. This mechanism consists of a power driven, water-cooled shaft on which the enthalpy probe is mounted. The actuator shaft is positioned in the 3 ft. diameter test section through 0-ring seals in the top and bottom access ports and both probe and actuator are electrically isolated from the vacuum chamber.

Experimental procedure

The procedure used to perform the stagnation enthalpy measurements was as follows:

1. The probe was positioned on the centerline of the arc-jet at approximately 0.020 inches downstream of the nozzle exit plane by means of a centering plug fitted to the nozzle contour and the probe inlet lip. The centerline position was then recorded on the probe actuator.
2. The probe was then moved to a position approximately 6 inches off the arc-jet centerline and the cooling water systems were activated.
3. The test chamber was then sealed and evacuated and the arc-jet started. All instrumentation was then monitored to ascertain when a steady-state condition of the opening parameters prevailed.
4. The probe was then moved into the arc-jet exhaust to the centerline position. The water flow rate to the internal cooling system was adjusted until the temperature differential was approximately 15 to 20^{o}F. The pressure and temperature before the flow nozzle were then recorded after which the cooling water flow rates were recorded.
5. The probe was then moved across the exit plane in increments of 0.05 inches. At each position the procedure of 4 was repeated. The residence time at each position was approximately 5 minutes

The parameters which are measured at each radial position are: w, the cooling water flow rate to the internal cooling system, ΔT, the temperature rise of the internal system cooling water, T_{ex}, the temperature of the gas at the probe exit, p, the gas pressure upstream of the flow nozzle. The mass flow rate of gas through the probe $\dot{m}_p$, is obtained from the nozzle calibration curve (Fig. B–2) for the measured p and T_{ex} values. The stagnation enthalpy is then calculated by the following relation

$$h_t = \frac{w\,\Delta T + C_p\,T_{ex}}{\dot{m}_p\ (p,\ T_{ex})} \qquad \text{(E–2)}$$

Stagnation enthalpy measurements

Stagnation enthalpy profile measurements were

obtained on a regeneratively-cooled arc-jet (GSC-2) and a water-cooled arc-jet (MAC–5), both of which are described in Section 4.4 of this report. Also presented in Section 4 is a comparison of the integrated power flux profiles and the measured power in the gas.

The difference between integrated power flux profile and the measured power to the gas is greatest at the 20 kW power level and decreases with increasing bulk exit enthalpy. The cause of this trend is not presently understood. Although the difference is significant at the low power levels, the comparisons are considered in good agreement in light of past experimental measurements of stagnation enthalpy in arc-heated plasma streams. Furthermore, it is suggested that the profiles are quantitatively correct and that the difference between the integrated power flux profile and the measure power to the gas is due to an inaccuracy in the magnitude of the enthalpy values.

Error analysis

The stagnation enthalpy is calculated using Eq. (E–2)

$$h_t = \frac{w(T_{in}-T_{out}) + C_pT_{ex}}{\dot{m}_p} \qquad (E-3)$$

which consists of several measured quantities, each of which have independent errors. The estimated uncertainty in each of the measured quantities is as follows:

w = cooling water flow rate, accuracy ±2%

$T_{out}-T_{in}$ = cooling water temperature rise, rise, accuracy ±2%

T_{ex} = exit gas temperature, accuracy ±1%

$\dot{m}_p$ = gas mass flow rate, accuracy ±3%

The uncertainty in h_t in terms of the individual uncertainties is

$$\frac{\Delta h_t}{h_t} = \left\{ \left(\frac{\Delta [w\,(T_{in}-T_{out}) + C_pT_{ex}]}{w\,(T_{in}-T_{out}) + C_pT_{ex}} \right)^2 + \left(\frac{\Delta \dot{m}_p}{\dot{m}_p} \right)^2 \right\}^{1/2}$$

Now $C_pT_{ex} \ll w\,(T_{in}-T_{out})$

Thus,

$$\frac{\Delta w\ (T_{in}-T_{out}) + C_pT_{ex}}{w\ (T_{in}-T_{out}) + C_pT_{ex}} \simeq \frac{\Delta w\,(T_{in}-T_{out})}{w\ (T_{in}-T_{out})} + \frac{\Delta (C_pT_{ex})}{w\,(T_{in}-T_{out})}$$

and since $\Delta (C_pT_{ex}) > C_pT_{ex}$

$$\frac{\Delta\,[w\,(T_{in}-T_{out}) + C_pT_{ex}]}{w\,(T_{in}-T_{out}) + C_pT_{ex}} \simeq \frac{\Delta\,[w\,(T_{in}-T_{out})]}{w\,(T_{in}-T_{out})}$$

Therefore,

$$\frac{\Delta h_c}{h_t} = \left\{ \left(\frac{\Delta w}{w} \right)^2 + \left(\frac{\Delta (T_{in}-T_{out})}{T_{in}-T_{out})} \right) + \left(\frac{\Delta \dot{m}_p}{\dot{m}_p} \right)^2 \right\}^{1/2}$$

$$\frac{\Delta h_c}{h_t} = \sqrt{17 \times 10^{-4}} = 4.12 \times 10^{-2} \text{ or 5 percent.}$$

Appendix F Spectrophotometer

Spectrophotometric observations were made at the exit plane of the MAC–5 and GSC–2 arc-jet. The purpose of these measurements was the determination of the excitation temperature profiles. The method of relative spectral line intensities

was used to obtain the excitation temperatures.

Average electron densities were also inferred from the spectral line shapes and the number of distinguishable lines in the spectrum for the MAC–5 arc-jet.

Theoretical considerations

Excitation temperature – The method of relative line intensities is based on the assumption that the time averaged intensity of the radiation emitted at a particular wavelength from an optically thin plasma is given by

$$I_{nm} = N_n E_{nm} A_{nm} \qquad (F-1)$$

where I_{nm} = time averaged intensity
N_n = number of atoms in state n
E_{nm} = energy emitted as a result of the transition from state n to state m
A_{nm} = Einstein transition probability

Since E_{nm} equals hc/λ_{nm}, Eq. (F–1) can be written

$$I_{nm} = \frac{h_c N_n A_{nm}}{\lambda nm} \qquad (F-2)$$

where λ_{nm} = wave length of emitted radiation,
h = Planck constant
c = velocity of light.

If it is assumed that the population of excited states obeys Boltzmann's law (Ref. 12), then

$$N_n = N_o \frac{g_n}{U(T)} \exp(-En/kT_{ex}) \qquad (F-3)$$

where N_o = total atom density
g_n = statistical weight of state n
$U(T)$ = partition function
E_n = energy of state n
k = Boltzmann's constant
T_{ex} = excitation temperature

The transition probability A_{nm} can be written in terms of the oscillator strength for emission (Ref. 13) as

$$A_{nm} = \frac{8\pi^2 he^2}{M_e C \lambda^2_{nm}} f_{nm} \qquad (F-4)$$

where f_{nm} = emission oscillator strength
e = electron charge
M_e = electron mass

Combining Eqs. (F–2, F–3, and F–4) gives:

$$I_{nm} = \frac{8 N_o h\pi^2 e^2}{U(T) M_e} \frac{g_n f_{nm}}{\lambda^3_{nm}} \exp(-En/kT_{ex}) \qquad (F-5)$$

For the Balmer series, which was used for the temperature measurements in this work, it is more convenient to use the absorption oscillator strength instead of the emission oscillator strength because the statistical weight is then constant. Making this substitution and taking the logarithm of Eq. (F–5) to the base 10 gives

$$\log_{10} \frac{I_{nm} \lambda^3 nm}{f_{mn}} = \text{Constant} - \frac{5040}{T_{ex}} E_n \qquad (F-6)$$

where f_{mn} = absorption oscillator strength.
A plot of

$$\log_{10} \frac{I_{nm} \lambda^3 nm}{f_{mn}} \text{ versus } E_n$$

should therefore be a straight line, the slope of which is inversely proportional to the temperature. The existence of a straight line plot provides a partial check on the assumptions used in obtaining the above equations. These assumptions were:

- The plasma is optically thin;
- The population of excited states obeys Boltzmann's law, with a unique excitation temperature at each radial position exhaust;
- The oscillator strengths as calculated by non-relativistic quantum mechanics are

valid in the plasma environment.

It should be noted that it is possible to obtain a straight line plot even though thermodynamic equilibrium does not exist locally in the exhaust. In this case the temperature measured would be the excitation temperature of the exciting particles and would not be the only temperature of the plasma.

Since it is the purpose of this work to measure radial temperature profiles, it is necessary to know I_{nm} as a function of radial position in the exhaust. Observations are made normal to the axis of the exhaust as shown in Fig. F–1. Calling the intensity measurements made in this manner $F_{nm}(y)$, and assuming cylindrical symmetry, we can write

$$F_{nm}(y) = 2 \int_y^R \frac{r I_{nm}(r)}{(r^2-y^2)^{1/2}}\, dr \qquad (F-7)$$

This is the Abel equation for $I_{nm}(r)$ and has the solution (Ref. 14)

$$I_{nm}(r) = \frac{-1}{\pi} \int_r^R \frac{\frac{d}{dy} F_{nm}(y)}{(y^2-r^2)^{1/2}}\, dy \qquad (F-8)$$

which is the intensity required to compute radial temperature values. Since the $F_{nm}(y)$ data will not in general fit some easily recognizable function it is necessary to perform the integration in Eq. (F–8) numerically. A computer program No. 22–10 has been written by the MAC 1620 Computer Group which performs this integration.

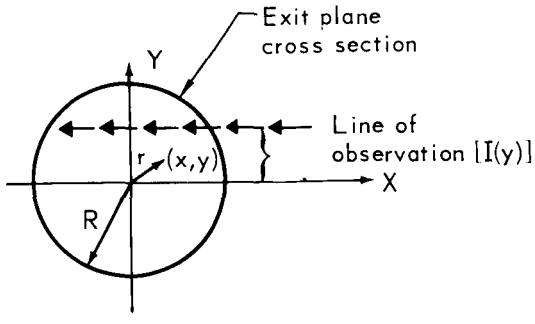

Fig. F–1 Sketch of observation geometry

Since only relative intensity measurements are required to determine the slope in Eq. (F-6), the intensity can be measured relative to a source of known spectral radiance. Intensity measurements were made with a photomultiplier tube calibrated with a tungsten strip lamp. In this case then

$$\frac{R_L}{R_S} = \frac{I_L}{I_S} \qquad (F-9)$$

where R_L and R_S are the responses of the photomultiplier tube to the spectrum line and the standard lamp respectively, and I_L and I_S are the intensities of the spectrum line and standard lamp respectively.

Electron density – The electron density of exhaust plasma can be calculated by determining the degree of spectral line broadening due to the Stark effect. Stark broadening arises from the effect of the ion and electron microfields on the energy levels of the atoms.

Griem, Kolb and Shen (Ref. 15) have calculated the Stark broadened profiles of the Balmer β and δ spectral lines of hydrogen for various electron densities. In this work the line profiles $S(\alpha)$ were described as a function of α, a reduced wavelength given by

$$\alpha = \frac{\lambda - \lambda_o}{1.253 \times 10^{-9}\, N_e^{2/3}} \qquad (F-10)$$

where α = reduced wave length

λ_o = wave length of unperturbed line

λ = wavelength

By noting the value of α at which S (α) is one half its maximum value, and designating this value $\alpha_{1/2}$ we can write

$$(\Delta\lambda)_{1/2} = 2\, \alpha_{1/2}\, 1.253 \times 10^{-9}\, N_e^{2/3} \qquad (F-11)$$

where $(\Delta\lambda)_{1/2}$ is the full width of the spectrum line at one half of its maximum value. The solution of

Eq. (F–11) has been obtained by Hill (Ref. 16) for a wide range of electron densities and electron temperatures and has published tables of electron densities as a function of $(\Delta\lambda)_{1/2}$ for various electron temperatures.

A second method by which electron densities may be determined is the Teller Inglis method (Ref. 12). This spectroscopic technique also utilizes the effect of Stark broadening applied to lines of the Balmer series; however, it is the number of resolvable spectral lines that are of interest rather than the individual line widths. The wave length at which the Stark broadened spectral lines converge into a continuum will be less than the wavelength for convergence of the unperturbed spectral since the line broadening increases with electron density.

In the Teller Inglis method the electron concentration is related to the principle quantum number of the state from which a transition to n = 2 state produces the last resolvable Balmer line by

$$\log_{10} 2\,N_e = 23.3 - 7.5 \log_{10} n_{max}$$

where N_e = electron density

n_{max} = quantum number of last resolvable Balmer line.

Experimental apparatus

The spectrophotometer used was a Baird Atomic three-meter concave-grating spectrometer, having a modified Eagle mount design. The grating has 15,000 lines/inch, which gives a dispersion of 5.6 Å/mm in the first order. The instrument is equipped with a 20 inch camera which permits photographing a 2840 Å range. For making spectrophotometric observations the spectrometer was modified so that a 1P21 photomultiplier tube could be swept across the 2840 Å range at speeds between 10.65 Å/min and 1065 Å/min. The output of the photomultiplier tubes is recorded on a 0–1 microamp two channel strip chart recorder. Incorporated in the phototube sweep mechanism is a slide wire resistor and wiper which traces the location of the photomultiplier tube on the same strip chart recorder which records the phototube response.

The optical arrangement is shown in Fig. F–2. The exhaust was viewed through quartz windows mounted in the vacuum chamber and the

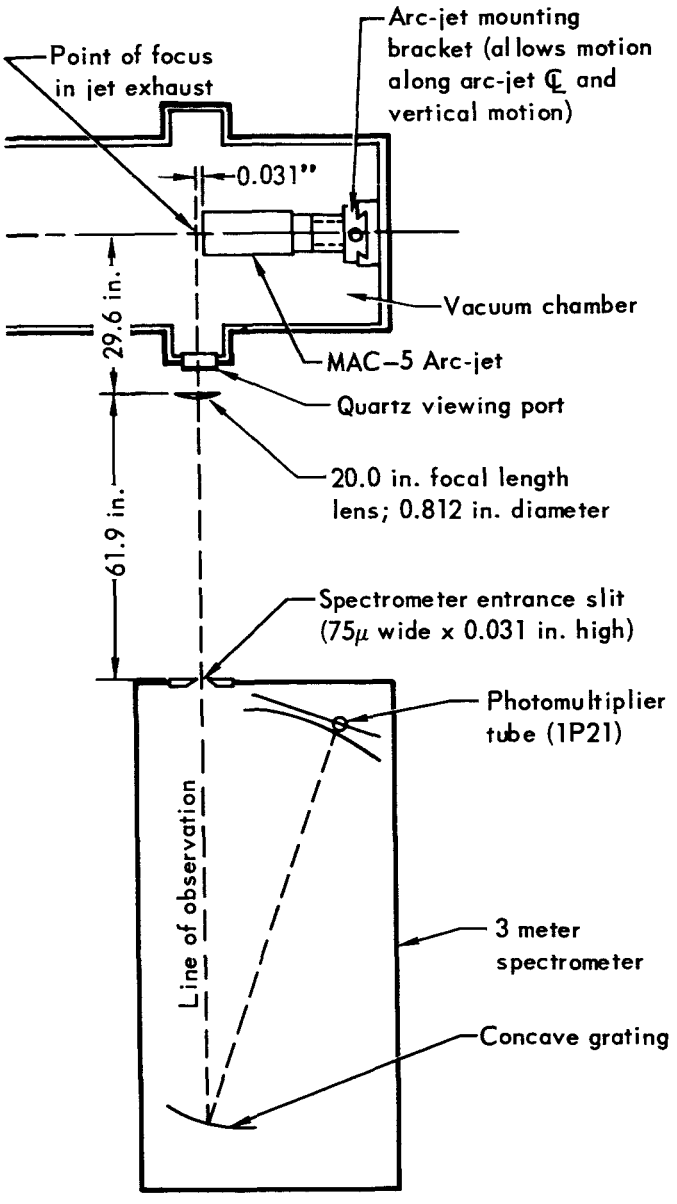

Fig. F–2 Spectrometer optics

line of observation was varied by moving the arc-jet in the vertical direction by means of adjustable platform within the vacuum chamber.

Experimental procedure

The procedure used in taking data was as follows:

- The arc-jet exhaust was focused on the entrance slit of the spectrometer.
- The image of the exit plane was aligned with the entrance slit, and then the arc-jet was moved 0.031 inch so that the line of observation was 0.031 inch from the exit plane.
- The H_β, H_γ, H_δ, and H_ϵ lines were scanned at a particular y position. The y position was then changed by moving the arc-jet vertically. The distance between each y position was 0.062 inch. The position of the photomultiplier tube was recorded on the same strip chart trace on which the spectrum lines were traced.
- This process was repeated until the entire exit plane had been traversed.
- After shutting off the arc-jet, a tungsten strip lamp was placed on the arc-jet centerline. The phototube response to this calibration lamp was then recorded at the wave lengths of the four Balmer lines.

Calculations

Excitation temperature – After having obtained spectral line traces and calibration traces it is necessary to measure the area under the spectrum traces. This was done with a planimeter. The relative spectral line intensity was calculated using the equation shown below.

$$\frac{A}{R_S} I_S K = I_L$$

where I_L = integrated relative line intensity

R_S = phototube response to standard lamp

I_S = spectral radiance of standard lamp

K = constant, dependent upon the wave length of spectral line, the speed at which the line is scanned, and a scale factor.

A = Planimeter area

Upon obtaining I_L, the quantity $\frac{I_L \lambda^3}{f}$ is plotted versus y. A typical plot of

$$\frac{I_L \lambda^3}{f} \text{ versus } y$$

is shown for the Balmer β, λ, δ, and ϵ lines in Fig. F–3. A smooth curve is fitted to this data and the points read from this curve are introduced into the Abel computer program to yield values of

$$\frac{I_L \lambda^3}{f}$$

as a function of radial position which are also shown in Fig. F–3. The results of each of the four Balmer lines observed are used to make a Boltzmann plot at each radial position. The excitation temperature is obtained from the slope of this plot which is shown in the lower curve of Fig. F–3

In general, the hydrogen β line was depressed below the straight line through the γ, δ, and ϵ data points on the Boltzmann plots.

Electron density – The electron density measurements determined by Stark broadening were obtained by measuring the full widths of the hydrogen β and lines at one half of the maximum value and referring to the Tables published by Hill (Ref. 16). For the densities reported an electron temperature of 10,000°K was assumed since this was the lowest published in the tables. It is noted that the effect of temperature is slight and a choice of 20,000°K would only change the electron concentration value by approximately 5%.

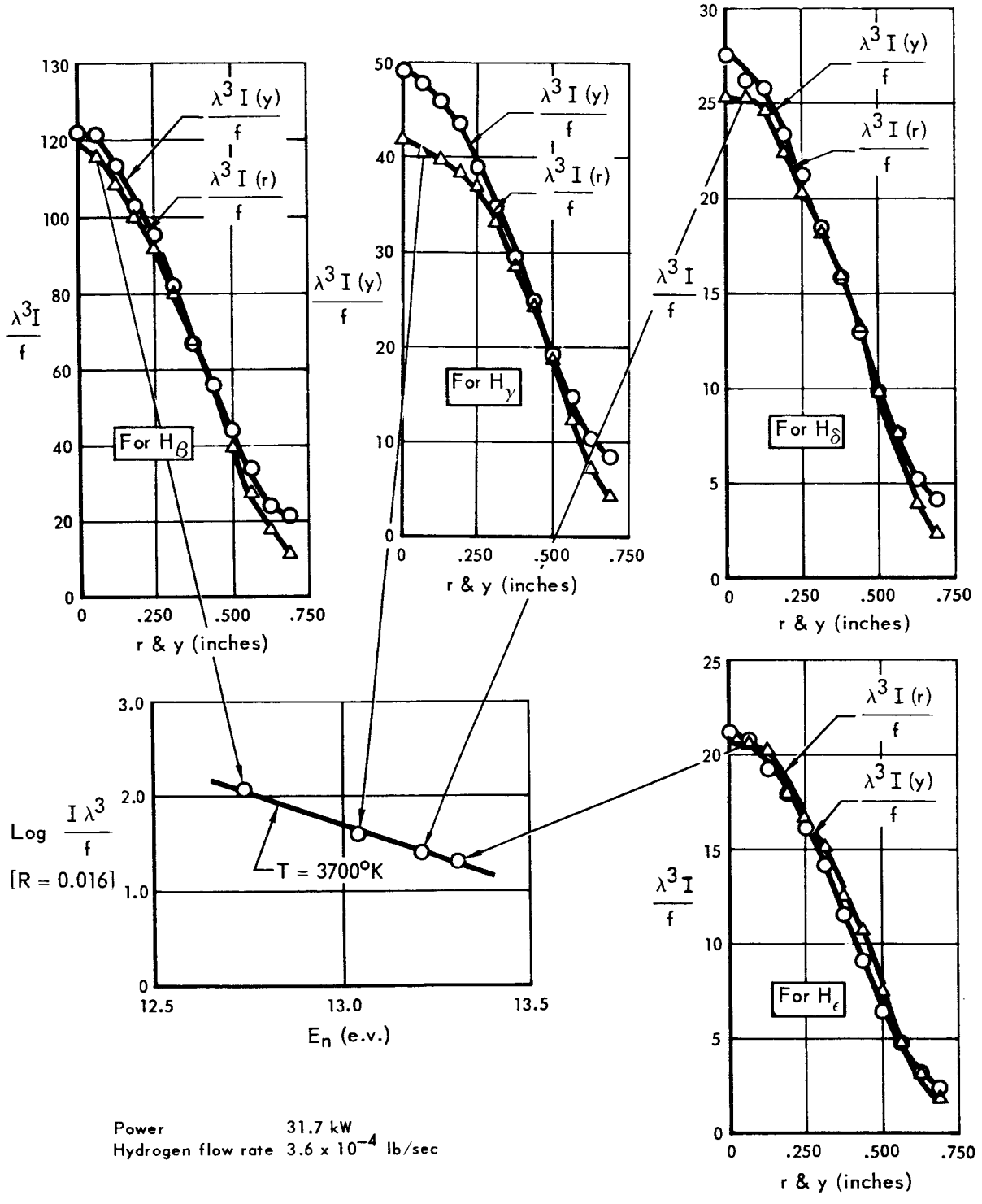

Fig. F-3 MAC-5 Arc-jet intensity profiles

Results

The results of the spectroscopic excitation temperature and electron density measurements are presented in Section 4 of this report along with a discussion of the possible errors in the measurements.

Appendix G Langmuir probe

The purpose of this work was the determination of electron densities in the exhaust region of a hydrogen arc-jet by means of a Langmuir probe.

Theory

A detailed description of the single Langmuir probe technique and the explanation of the Langmuir characteristic curve is given in Ref. 17 and in many other sources. Basic to this technique is the assumption that the electrons within the sheath surrounding the probe possess a Maxwellian velocity distribution. If this condition is fulfilled then the electron current density at the surface of the probe is given by

$$J = eN_e \left(\frac{kT_e}{2\pi M_e}\right)^{1/2} \exp\left(\frac{-eV}{kT_e}\right) \qquad (G-1)$$

Where J = current density coulombs/sec/m^2
k = Boltzmann constant (joules/^oK)
e = electron charge (coulombs)
M_e = electron mass (kg)
T_e = electron temperature (^oK)
N_e = electron density (#/m^3)
V = plasma-probe potential difference (volts)

Taking the logarithmic differential of Eq. (G–1) with respect to voltage, V, yields

$$\phi = \frac{d}{dV}(\ln J) = -\frac{e}{kT_e} = \frac{11{,}600}{T_e} \qquad (G-2)$$

The current density J is obtained by dividing the probe current by the collecting area of the probe. Thus, the quantity ϕ can be determined by the slope of the logarithm of the current density versus probe voltage curve. This is valid when the probe is in the electron collecting region and the plasma potential is constant.

The electron density is obtained by noting when V = 0. Equation (G–1) becomes

$$J_o = eNe\left(\frac{kTe}{2\pi Me}\right)^{1/2} = eNe\left(\frac{11{,}600k}{2\pi Me}\right)^{1/2}\left(\phi^{-1/2}\right)$$

or

$$N_e = \frac{J_o}{e}\left(\frac{2\pi Me}{11{,}600k}\right)^{1/2} \phi^{1/2}$$

$$N_e = \frac{I_o}{eA}\left(\frac{2\pi Me}{11{,}600k}\right)^{1/2} \phi^{1/2} \qquad (G-3)$$

where I_o is the electron current to the probe when the probe voltage is equal to the plasma potential and A is the collecting area of the probe.

Consequently, N_e the electron density is obtained by a knowledge of ϕ and I_o since all other quantities are constant and known.

Experimental apparatus and procedure

Figure G–1 is a photograph of the single Langmuir probe and its housing apparatus. The associated electrical circuit is shown in Fig. G–2. The entire probe system, including the housing, is floated electrically so as to prevent the probe from drawing dc current directly from the arc. The second probe, P_2, completes the electrical circuit but does not change the characteristic single probe effect.

To obtain data, the following procedure is

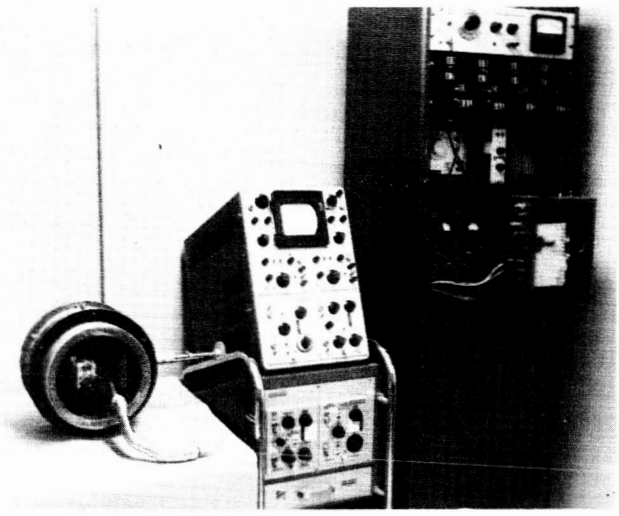

Fig. G–1 Langmuir probe apparatus

used: a 1000 cps wave form is amplified and applied between the two probes. The oscillo- channel of the oscilloscope is utilized to record probe position. The input to this channel is supplied by a rotary potentiometer whose output is proportional to the angular position of the probe arm. The probes are swept through the exhaust stream and the resulting voltage and current characteristics and the probe position are photographed simultaneously from the oscilloscope screen. These data are then used to make a linear plot of total probe current vs. probe-to-probe voltage (Fig. G–3). Since the slope in Eq. (G–2) is that taken from a plot of electron current vs. probe-to-probe voltage, it is neces-

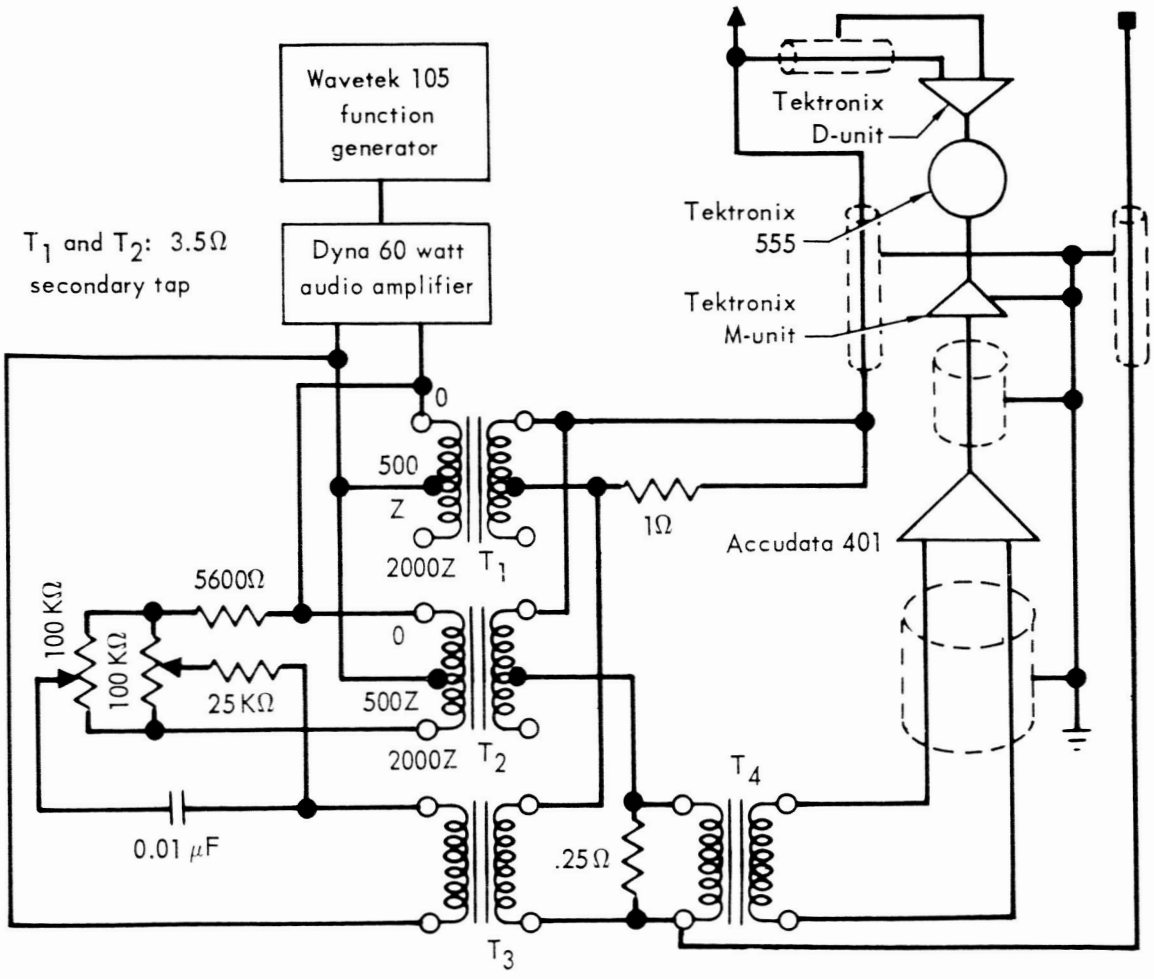

Fig. G–2 Langmuir probe electrical diagram

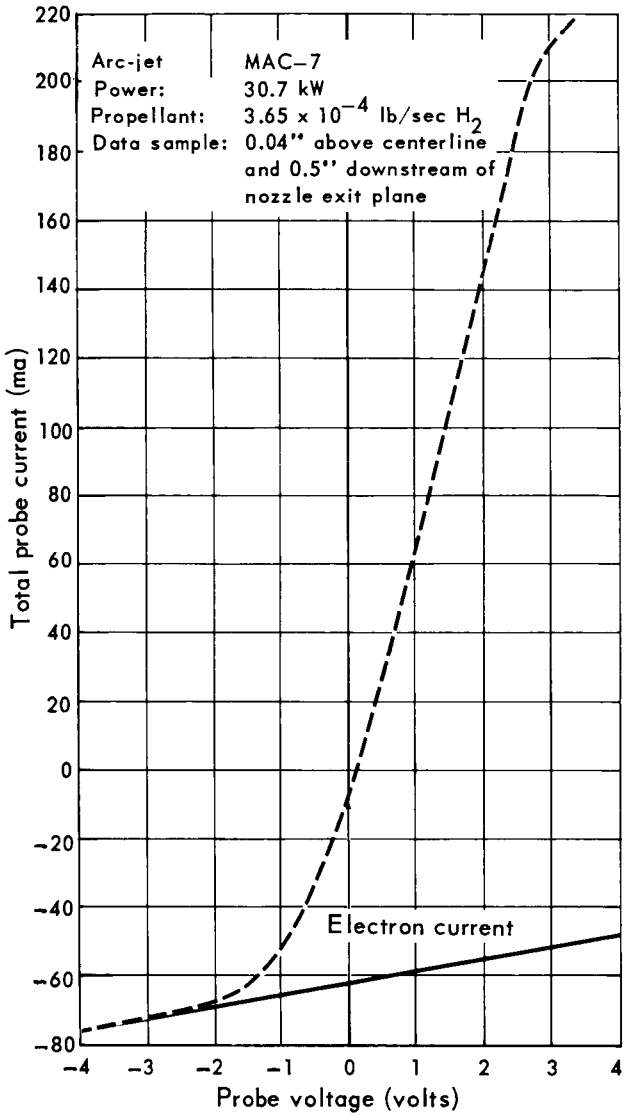

Fig. G–3 Sample Langmuir probe data

sary to extrapolate the lower portion of the curve in Fig. G–3 (positive ion current) over the entire voltage range used and subtract this curve from the total current curve. The semi-logarithmic plot resulting from this procedure is shown in Fig. G–4. Note that the quantity I_o appearing in Eq. G–3 is shown in Fig. G–4 as the value of the point of intersection of the extrapolations of the two linear sections of the curve.

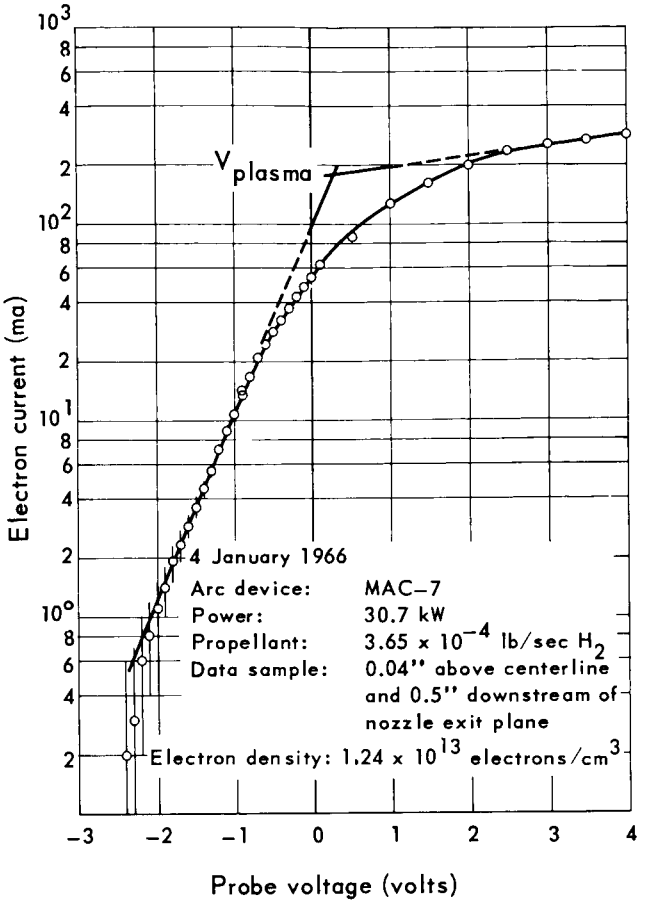

Fig. G–4 Sample Langmuir probe data

Results

The electron density measurements obtained with the Langmuir probe are presented in Section 4 of this report.

Error analysis

The equation used to determine the electron density is

$$N_e = \frac{(\text{constant})\, I_o}{A}\ \phi^{\frac{1}{2}}$$

The estimated uncertainty of each of the experimentally measured quantities is as follows.

I_o = random electron current when probe voltage is equal to plasma potential ±25%.

A = probe collecting area ± 10%

ϕ = slope of I versus V on semilog plot ±75%

$$\frac{\Delta N_e}{N_e} = \left\{ \left(\frac{\Delta I_o}{I_o}\right)^2 + \frac{1}{2}\left(\frac{\Delta \phi}{\phi}\right)^2 + \left(\frac{\Delta A}{A}\right)^2 \right\}^{1/2}$$

and

Thus the estimated uncertainty in N_e is

$$\frac{\Delta N_e}{N_e} = \left(35.5 \times 10^{-4}\right)^{1/2} = 0.59 \times 10^{-2} \text{ or } \pm 60\%.$$

Appendix H Test data

Table H–1 Operating condition for thrust stand tests

Test no.	Hydrogen flow rate (lb/sec x 10^{-4})	Power input (kW)	Exit plane stagnation enthalpy (B/lb)	Thermal efficiency (%)	Arc chamber pressure (torr)
1–NAS1–TS	3.50–5.60	6–36			662–1070
2–NAS1–TS	3.50–5.50	6–33			678–1039
3–NAS1–TS	3.53–5.53	6–32			630–1054
4–NAS1–TS	3.48–5.43	6–30			693–1062
5–NAS1–TS	3.50–5.45	6–30			698–1078
9–MAC2–TS	3.53–5.53	6–29			340–555
12–MAC2–TS	3.53–5.51	17–30			351–552
51–MAC5–TS	4.50	21–32			314–344
52–MAC5–TS	4.01	21–32			288–318
53–MAC5–TS	3.63	21–32			269–295
54–MAC5–TS	3.53	20–33			266–288
55–MAC5–TS	4.50	10–42			283–352
56–MAC5–TS	3.62	11–43			233–298
57–MAC5–TS	4.03–4.52	21–51			303–381
58–MAC5–TS	3.63–4.54	20–43			274–377
59–MAC5–TS	3.61–4.52	21–43			277–381
60–MAC5–TS	3.53–4.54	20–43			274–381
100–X1–TS	4.35	44–80	70,900–115,600	65–72	18–23
107–X1–TS	4.36	30–133			30–34
112–X1–TS	1.32	31–57			17–20
116–X1–TS	1.30	30–70			25–30
123–X1–TS	4.92	12–100	15,600–106,400	54–61	28–66
126–X1–TS	1.06–1.33	27.7	142,000–162,200	65–70	19–22
127–X1–TS	0.86–1.33	22–34	54,100–162,200	32–71	17–22
129–X1–TS	1.04–1.33	30–108	117,600–549,200	39–68	20–31
133–X1–TS	1.06–1.34	30–95	111,500–388,500	40–58	35–40
153–X1–TS	1.32	24–32	123,500–238,500	59–73	18–24
154–X1–TS	1.31	26–81	112,300–359,000	57–61	23–30
155–X1–TS	0.37–1.32	21–93	90,800–476,600	40–62	
187–X1–TS	0.88–1.32	25–87	105,100–585,300	51–63	
201–X1–TS	0.76–1.32	25–94	88,700–596,900	47–57	20–33
203–X1–TS	0.77–1.33	26–90	99,900–567,900	41–57	20–33
205–X1–TS	0.66	27–51	212,400–425,100	53–57	
225–X1–TS	0.75–1.31	25–94	99,100–626,500	52–59	21–32
234–GSC2–TS	7.37	23–30			910–1027
242–GSC2–TS	7.37	22–30			875–970
250–GSC2–TS	7.35	26–30			902–963

Table H-2 Operating conditions for mass flux probe tests

Test no.	Hydrogen flow rate ($lb/sec \times 10^{-4}$)	Power input (kW)	Exit plane stagnation enthalpy (B/lb)	Thermal efficiency (%)	Arc chamber pressure (torr)	Vacuum pressure (torr)
61-MAC4-MFP	3.62	31.0			333	0.80
87-MAC4-MFP	3.62	31.4			326	0.68
91-MAC4-MFP	3.66	33.0			325	0.70
92-MAC4-MFP	3.60	31.3			305	0.68
94-MAC4-MFP	3.63	30.7			315	0.68
101-MAC4-MFP	3.63	32.3			320	
102-MAC4-MFP	3.63	31.0			320	
103-MAC4-MFP	3.64	32.3			323	
108-MAC4-MFP	3.62	20.6	45,500	81.0	290	2.24
109-MAC4-MFP	3.63	26.5	54,400-58,100	76-81	309	
113-MAC4-MFP	3.63	31.0	65,500	78.5	320	
117-MAC4-MFP	3.05-3.62	28.1	61,300-72,600	81.0	312	
118-MAC4-MFP	3.67	31.0	65,000	79.3	325	
120-MAC4-MFP	3.60	30.8	65,600	78.7		
121-MAC4-MFP	3.64	31.6	66,600	79.0	323	0.05-2.11
132-MAC4-MFP	3.63	32.0	67,500	79.0	325	0.09-2.24
136-MAC4-MFP	3.63	31.9	68,000	78.8	325	0.09-2.77
142-MAC4-MFP	3.63	31.5	62,800-71,100	73-86	332	1.19-2.74
145-GSC2-MFP	7.43	28-31			960	
147-MAC4-MFP	3.67	31.7	67,700	80.4	332	1.64-1.96
148-MAC4-MFP	4.57	31.6	54,700	80.7	387	1.50-2.24
150-MAC4-MFP	3.62	30.8	65,700	79.0	327	2.27
151-MAC4-MFP	4.01	31.9	62,800	81.0	350	2.30
152-MAC4-MFP	4.53	31.9	56,300	81.0	387	2.19-2.74
165-GSC2-MFP	7.37	30.5			941-954	
166-GSC2-MFP	7.28	31.0			953	
191-MAC4-MFP	3.60	31.5	66,700	78.5	336	0.32-0.38
193-MAC4-MFP	3.64	31.3	64?300-69,100	77-81	340	0.35-0.38
194-MAC4-MFP	3.55	31.3	66,800-67,700	78.3	344	0.35
199-MAC4-MFP	3.61	31.4	65,300-68,100	78.0	323-337	0.35-0.43
200-MAC4-MFP	3.66-7.37	31.5	35,900-66,800	77-84	342-608	0.39-1.35
210-MAC4-MFP	3.62	31.5	66,000	78.0	330	0.26-0.28
211-MAC4-MFP	3.63-4.52	32.0	53,000-67,500	78.0	332-390	0.26-0.54
212-MAC4-MFP	3.62	20.8	45,200	79.9	302	0.32
213-MAC4-MFP	3.65	20-33	44,900-69,800	77-80	303-340	0.38-0.45
214-MAC4-MFP	3.60	36-42	75,400-87,600	76-78	346-368	0.40-0.43
218-MAC4-MFP	3.63	6-21			282-365	0.28-0.32
220-MAC4-MFP	3.63	21.0	45,800	79.3	298	0.30-0.51
221-MAC4-MFP	4.01	20.8	40,200	78.5	330	0.62
227-MAC4-MFP	3.61	20.6	45,000	79.5	298	0.38
232-MAC4-MFP	3.65-4.54	20.5	34,900-43,200	75-79	305-358	0.38-0.84
253-MAC4-MFP	3.62-4.52	20.8	35,400-44,100	76-79	298-355	0.40-0.77
254-MAC4-MFP	4.02-4.53	25.6	44,300-48,100	74-79	344-380	0.51-0.84
255-MAC4-MFP	3.62-4.52	24-30	49,900-51,900	76-79	314-391	0.38-0.82
256-MAC4-MFP	4.00	30.5	58,000	76-79	357	0.51-0.57
258-MAC4-MFP	3.62-4.51	30-36	60,800-65,900	77-82	332-400	0.40-0.80
263-MAC4-MFP	4.47	35.0	59,200	77.6	402	0.68
264-MAC4-MFP	3.63-4.00	35.0	67,300-73,500	76-79	347-377	0.32-0.45
265-MAC4-MFP	4.53	40.4	68,300	78.7	416	0.77
276-MAC4-MFP	3.63-4.03	30-36	63,600-68,600	79.0	332-382	0.30-0.40
277-MAC4-MFP	3.63	30.4	63,600-65,400	78.5	338	0.35
278-MAC4-MFP	3.62	30.1	58,200-60,300	72.8	337	0.28-0.30

Table H–2 Operating conditions for mass flux probe tests (Continued)

Test no.	Hydrogen flow rate (lb/sec x 10^{-4})	Power input (kW)	Exit plane stagnation enthalpy (B/lb)	Thermal efficiency (%)	Arc chamber pressure (torr)	Vacuum pressure (torr)
279–MAC4–MFP	3.63	30.3	59,700–66,200	73–82	38	0.32
287–MAC4–MFP	3.62	30.0	62,600	77.7	330	0.30
288–MAC4–MFP	3.63	30.7	63,800	77.4	335	0.30
290–MAC4–MFP	3.64	30.7	63,900	77.7	333	0.30
292–MAC4–MFP	3.63	30.7	65,400	79.3	325	0.35–0.38
294–MAC4–MFP	3.66	30.7	64,900	79.4	320	0.30
295–MAC4–MFP	3.65	30.4	64,900	80.1	319	0.30
296–MAC4–MFP	3.63	30.5	64,500–68,200	79.3	325	0.37–0.42
299–MAC4–MFP	3.63	30.6	65,200	79.4	322	0.38–0.40
300–MAC4–MFP	3.99	35.4	73,800	81.1	353	0.42
302–MAC4–MFP	3.97	35.7	71,000	81.2	356	0.40–0.45
303–MAC4–MFP	3.63	35.2	74,500	79.0	335	1.07–1.10
309–MAC4–MFP	3.61–3.99	30–36	64,200–70,400	79–81	318–356	0.32–0.45
312–MAC4–MFP	4.01	35.8	70,800	81.8	360	0.45
314–MAC4–MFP	4.03	35.6	59,600	80.7	360	0.45–0.51

Table H–3 Operating conditions for impact pressure probe tests

Test no.	Hydrogen flow rate (lb/sec x 10^{-4})	Power input (kW)	Exit plane stagnation enthalpy (B/lb)	Thermal efficiency (%)	Arc chamber pressure (torr)	Vacuum pressure (torr)
30–MAC4–PP	3.62	20.5	42,000	75.0	287	0.60
31–MAC4–PP	3.62	31.1	60,300	72.0	322	0.57
32–MAC5–PP	3.61	20–31	40,000–55,000	65–72	278–311	0.45
33–MAC5–PP	3.61	20–34	41,200–62,800	68–73	278–318	0.40
34–MAC5–PP	3.65	10–21	23,700–45,600	79.4	247–285	0.74
35–MAC5–PP	3.65	21–26	53,500–65,800	95.0	287–301	0.80
36–MAC5–PP	3.67	42.1	106,300	96.3	340	0.74
37–MAC5–PP		20–37				
41–MAC4–PP	3.63–4.52	20–42	33,800–77,400	69–74	287–397	0.40–1.28
46–MAC4–PP	4.52	20–41	32,800–62,500	68–72	330–403	0.68–0.80
47–MAC4–PP	3.63–4.04	21–42	36,500–77,100	68–72	298–372	0.35–0.51
48–MAC4–PP	3.62–4.50	20–43	35,000–72,800	68–73	294–408	0.35–0.80
71–MAC4–PP	3.62–4.51	32.0	54,400–68,300	78–81	329–387	0.40–0.71
73–MAC4–PP	3.62	31.8	67,900	79.4	333	0.35
74–MAC4–PP	3.61	32.4	69,600	79.6	332	0.38
75–MAC4–PP	3.63–4.52	21–33	36,700–69,600	78–81	329–392	0.45–0.80
143–GSC2–PP	7.37	25–30				
144–GSC2–PP	7.40	31				

Table H-4 Arc-jet operation conditions for velocity meter tests

Test no.	Hydrogen flow rate ($lb/sec \times 10^{-4}$)	Power input (kW)	Exit plane stagnation enthalpy (B/lb)	Thermal efficiency (%)	Arc chamber pressure (torr)	Vacuum pressure (torr)
10-MAC3-VM	3.64-4.53	6-30	18,000-68,500	86-97	285-480	0.40-0.78
11-MAC3-VM	3.64	9-23	24,100-54,900	86-95	270-384	0.38-1.03
13-MAC3-VM	3.62-4.54	6-23	14,600-55,400	85-95	310-453	0.38-0.72
14-MAC3-VM	3.56-3.57	9-23	26,100-55,400	85-98	322-427	0.40-0.45
15-MAC3-VM	3.58-4.03	6-30	16,400-68,300	84-98	334-483	0.40-0.53
16-MAC3-VM	3.60-3.64	9-29	26,700-66,900	84-98	336-455	0.36-0.40
17-MAC3-VM	3.59-4.44	9-23	30,100-52,700	81-96	347-439	0.32-0.55
18-MAC3-VM	3.59-3.64	9-23	23,600-55,400	84-95	346-405	0.36-0.38
19-MAC3-VM	3.60-4.48	6-23	15,100-54,000	84-95	350-407	0.36-0.63
20-MAC3-VM	3.57-3.98	6-23	16,300-56,600	84-97	349-407	0.32-0.40
21-MAC3-VM	3.58-4.03	6-23	16,200-57,000	84-97	355-437	0.32-0.53
22-MAC3-VM	3.60-4.02	6-23	16,500-60,300	84-97	351-448	0.30-0.53
24-MAC3-VM	3.62-4.61	8-32	16,100-65,000	72-96	306-430	0.38-0.74
25-MAC3-VM	3.63-4.38	7-25	16,200-54,600	75-96	315-411	0.45-0.82
26-MAC4-VM	3.63	30.4	57,700	70	300	0.68
27-MAC4-VM	3.63	31.2	61,000	73	305	0.68
28-MAC4-VM	3.63	30.8	59,500	72	310	0.66
38-MAC4-VM	3.62	25.0	49,900	73	302	0.35-0.40
39-MAC4-VM	3.44-5.30	25-41	36,300-73,300	69-76	302-397	0.30-1.30
40-MAC4-VM	3.42-4.98	20-42			282-442*	0.30-1.28
42-MAC4-VM	4.05-4.38	24-42	42,800-75,800	70-75	328-380	0.45-0.62
43-MAC4-VM	4.38	24.7	39,800	70.8	353	0.74-0.80
44-MAC4-VM	4.37	24.9	39,900	70.6	355	0.62-0.74
45-MAC4-VM	3.61-4.37	23-31	37,300-59,800	69-73	306-353	0.35-0.68
49-MAC4-VM	4.37	25.0	40,300	71	355	0.77-1.05
50-MAC4-VM	4.37	25-32			356-380	0.84-1.12
62-MAC4-VM	4.37	25.6			350	0.68
63-MAC4-VM	3.62-4.40	18-33	39,600-66,000	77-81	290-381	0.62-1.10
64-MAC4-VM	4.05-4.37	25-32	46,500-61,300	77-79	342-381	0.95-2.23
65-MAC4-VM	3.63-4.69	20-38	36,100-76,600	77-80	306-416	1.00-2.27
67-MAC4-VM	3.74-4.38	20-33	38,300-62,800	78-81	304-378	0.40-0.62
68-MAC4-VM	4.37-4.72	21-37	32,300-64,800	71-80	345-414	0.66-0.84
69-MAC4-VM	4.35	26-33	47,100-58,100	79.3	353-374	0.67
70-MAC4-VM	4.37	26.1	46,400	78.9	358	0.68
72-MAC4-VM	3.68-4.70	20-32	42,900-67,900	78-81	306-405	0.35-0.74
78-MAC4-VM	3.94-4.38	25-32	45,100-62,700	77-80	352	0.45-0.71
96-MAC4-VM	3.65-4.55	20-33	34,000-66,400	74-79		
128-GSC2-VM	7.32	31.0			960	0.600
130-GSC2-VM	7.40	26-32			910-962	
131-GSC2-VM	7.43	31.0			935-960	
134-GSC2-VM	7.32	30.4			940-959	
135-GSC2-VM	7.37	30.5			955-968	
137-GSC2-VM	7.35	31.3			947-961	
138-GSC2-VM	7.43	31.0			955-968	
140-GSC2-VM	7.37	31.0			950-965	
158-MAC4-VM	4.49	21.3	36,500	77.0	349	0.71-0.80
159-MAC4-VM	4.55	20-37	35,400-61,000	74-79	347-397	0.80-0.90
161-MAC4-VM	4.52	21-33	35,900-55,100	74-79	352-390	0.71-0.80
164-MAC4-VM	4.49-4.62	31.3	51,100-54,300	66.0	389	
167-MAC4-VM	4.55	21-33	36,100-54,400	76-81	358-396	
168-MAC4-VM	3.65-4.55	21-35	36,500-65,500	75-81	325-372	
169-MAC4-VM	4.53	20-37	35,500-63,000	76-80	355-403	

Table H–4 Arc-jet operation conditions for velocity meter tests (Continued)

Test no.	Hydrogen flow rate ($lb/sec \times 10^{-4}$)	Power input (kW)	Exit plane stagnation enthalpy (B/lb)	Thermal efficiency (%)	Arc chamber pressure (torr)	Vacuum pressure (torr)
170–MAC4–VM	3.62–4.04	21–32	41,600–65,200	78–81	320–356	
171–MAC4–VM	3.66–4.07	21–32	44,800–62,600	76–82	306–360	
172–MAC4–VM	3.63	20–37	45,000–76,900	78–81	299–349	
173–MAC4–VM	3.66–4.08	20–26	44,700–50,400	80.6	299–342	
174–MAC4–VM	3.60–4.50	20–37	45,900–67,500	79–81	301–405	
177–MAC4–VM	4.07–4.55	20–36	36,200–61,400	77–79	323–399	
180–GSC2–VM	7.40	24–32			875–970	
181–GSC2–VM	7.37	31.2			960–972	
186–GSC2–VM	7.40	25–31			927–963	
207–GSC2–VM	7.40	30.6			952	
228–GSC2–VM	7.37	30.1			950	

Table H–5 Operating conditions for enthalpy probe tests

Test no.	Hydrogen flow rate ($lb/sec \times 10^{-4}$)	Power input (kW)	Exit plane stagnation enthalpy (B/lb)	Thermal efficiency (%)	Arc chamber pressure (torr)	Vacuum pressure (torr)
216–GSC2–EP	7.32	30.8				
217–GSC2–EP	7.37	30.5				
229–MAC5–EP	4.54	19.6	33,800	78.2	320	0.62–0.68
230–MAC5–EP	4.03	20.0	38,200	77.2	297	0.40–0.48
236–MAC5–EP	4.52	19.8	34,300	78.2	324	0.54–0.60
238–MAC5–EP	4.52	19.8	34,300	78.2	326	0.57–0.60
240–MAC5–EP	4.50	19.9	34,600	78.2	326	0.57–0.62
241–MAC5–EP	3.99	19.5	37,500	77.2	298	0.35
243–MAC5–EP	3.64	19.8	41,500	76.5	278	0.32
244–MAC5–EP	4.51	25.2	44,300	80.0	342	0.54–0.57
245–MAC5–EP	4.02	25.0	47,000	76.8	315	0.38–0.40
246–MAC5–EP	3.67	25.3	52,600	77.7	292	0.28–0.30
247–MAC5–EP	4.53	30.0	50,300	77.2	356	0.60–0.66
248–MAC5–EP	4.02	30.0	57,700	79.0	329	0.38
251–MAC5–EP	3.64	30.5	63,500	77.7	306	0.35
257–MAC5–EP	3.63–4.53	19–31	34,700–63,400	78.0	207–355	0.30–0.66
261–MAC5–EP	4.52	29.8	50,000	77.2	358	0.54
267–MAC5–EP	4.51	25.5	43,000	77.2	344	0.60–0.62
268–MAC5–EP	4.02	25.0	47,500	77.5	316	0.40
269–MAC5–EP	3.63	25.3	53,200	77.7	294	0.30
270–MAC5–EP	4.00	19.8	37,800	77.2	302	0.40
271–MAC5–EP	3.62	20.0	42,300	77.3	280	0.28
272–MAC5–EP	4.52	30.0	50,300	77.0	359	0.66
273–MAC5–EP	4.00	30.3	58,800	79.0	328	0.38
274–MAC5–EP	3.62	30.6	64,100	77.7	310	0.33
275–MAC5–EP	4.51	20.2	35,000	78.2	329	0.65
280–MAC5–EP	3.63–4.53	19–30	34,900–63,600	77.8	279–356	0.30–0.60
283–MAC5–EP	3.62–4.52	20–30	34,800–63,800	78.0	283–364	0.30–0.62
306–MAC5–EP	3.61–4.51	19–31	34,700–64,100	76–79	284–365	0.30–0.62
307–MAC5–EP	3.63–4.52	19–31	35,600–65,500	76–79	282–350	0.26–0.60
308–MAC5–EP	3.61–4.51	19–31	35,400–64,000	77–79	282–365	0.30–0.65
310–MAC5–EP	3.60	20.0	41,200–44,200	77.8	280	0.30
311–MAC5–EP	3.62	20.5	43,800	78.0	283	0.30
315–MAC5–EP	4.50	35.8	60,000	77.3	380	0.68–0.71
317–MAC5–EP	4.04	35.8	67,500	78.3	349	0.45–0.51
318–MAC5–EP	3.65	35.8	73,300	77.2	320	0.35

Table H–6 Arc-jet operating conditions for spectrometer test

Test no.	Hydrogen flow rate ($lb/sec \times 10^{-4}$)	Power input (kW)	Exit plane stagnation enthalpy (B/lb)	Thermal efficiency (%)	Arc chamber pressure (torr)	Vacuum pressure (torr)
66–MAC5–SP	3.63	31.7	66,100	77.7		0.28–0.35
76–MAC5–SP	3.63	33.2	69,000	77.5	308	0.28–0.35
77–MAC5–SP	3.61	33.0	69,000	77.5		0.40
79–MAC5–SP	3.65–4.07	31.5	59,800–64,800	77–79		0.09–0.17
80–MAC5–SP	4.03	29–33	55,700–62,300	78–79	320	0.40
81–MAC5–SP	4.25	31.6	56,800	78.0	336	0.48
82–MAC5–SP	3.63	36.5	75,400	77.2	313	0.28–0.32
83–MAC5–SP	3.64	26.3	55,000	77.7	288	0.28
84–MAC5–SP	3.63–4.07	20–32	39,600–60,700	77–79	273–323	0.32–0.48
85–MAC5–SP	4.00–4.28	21–27	37,900–49,600	77.5	307–320	0.35–0.45
86–MAC5–SP	4.04–4.30	36–38	62,800–71,800	78.0	333–350	0.38–0.57
88–MAC5–SP	3.60	31.2	65,700	77.7	296	0.30
124–GSC2–SP	7.37	24–32			848–960	
222–MAC7–SP	3.62	25–35			289–313	0.28
321–MAC5–SP	3.65	35.3				0.28–0.30
322–MAC5–SP	3.61–4.27	20–36				0.30–0.51
324–MAC5–SP	3.45–4.00	30–36				0.30–0.51

Table H–7 Operating conditions for langmuir probe tests

Test no.	Hydrogen flow rate ($lb/sec \times 10^{-4}$)	Power input (kW)	Vacuum pressure (torr)
156–MAC5–LP	3.63	21.5	
160–MAC5–LP	3.63	32.3	
178–MAC5–LP	3.61	21.4	
179–MAC5–LP	3.65	21.7	
215–MAC5–LP	3.62	21.0	
223–MAC5–LP	3.64	20.0	0.30–0.35
224–MAC5–LP	3.65	30.1	0.38–0.43
226–MAC5–LP	3.62	18.7	0.30
249–MAC7–LP	3.61	19.3	0.32
251–MAC7–LP	3.61	19–36	0.35
260–MAC7–LP	3.62	30.3	0.37
262–MAC7–LP	3.62	19–30	0.30–0.32
313–MAC7–LP	3.62–4.03	19–36	0.20–0.40
316–MAC7–LP	3.62–4.02	19–35	0.35–0.51

Table H–8 Operating conditions for static pressure tests

Test no.	Hydrogen flow rate ($lb/sec \times 10^{-4}$)	Power input (kW)	Exit plane stagnation enthalpy (B/lb)	Thermal efficiency (%)	Arc chamber pressure (torr)	Vacuum pressure (torr)
319–MAC4–ESP	3.65–4.51	20–31	35,500–52,700	78.9	287–366	0.68–1.23
320–MAC4–ESP	3.63–4.54	19–36	34,900–77,000	78–81	284–380	0.62–1.23
323–MAC4–ESP	3.63–4.04	20–36	39,800–77,300	79–81	284–328	0.40
328–MAC4–ESP	4.00	20–41	39,500–80,000	78–82	309–368	0.60–0.66
325–MAC7–NSP	3.63–4.52	18–26	34,400–53,900	76–79		0.51–0.95
326–MAC7–NSP	3.68–4.57	24–36	41,400–72,000	76–78		0.40–0.98
327–MAC7–NSP	4.00–4.54	35.8	58,700–69,700	76–79		0.57–0.87
329–GSC2–ESP	7.32	30.6				

Table H–9 Operating conditions for calorimeter tests

Test no.	Hydrogen flow rate ($lb/sec \times 10^{-4}$)	Power input (kW)	Exit plane stagnation enthalpy (B/lb)	Thermal efficiency (%)	Arc chamber pressure (torr)	Vacuum pressure (torr)
6–NAS1–C	3.53–5.55	6–31	12,100–73,300	91–96	669–1088	0.30–1.22
7–NAS1–C	3.52–5.50	13–35	23,700–81,000	90–97	622–1082	0.24–1.07
8–MAC3–C	3.51–4.51	12–29	28,800–60,900	85–94	329– 469	0.30–0.59
11–MAC3–C	3.53–4.56	13–29	28,300–62,900	85–93	325– 477	0.38–0.72
16–MAC3–C	3.51–4.49	13–30	29,100–67,600	84–93	379– 535	0.36–0.74

9 References

1. J.P. Todd, et. al., "Thirty kW Arc-Jet Thrustor Research," Giannini Scientific Corporation Report APL–TDR–64–58, (March 1964).
2. M.M. Chen, "Theoretical and Experimental Investigation of Arc-Jet Engine Nozzle Flow," AVCO Corporation RAD, Report RAD–SR–62–212, (September 1962).
3. J.P. Todd and R.E. Sheets, "Development of a Regeneratively-Cooled 30 kW Arc-Jet Engine," AIAA Journal 3, No. 1 (January 1965).
4. "Janaf Thermochemical Tables," Dow Chemical Company, (December 1960).
5. S. Bennett, "Theoretical and Experimental Investigation of Arc-Jet Engine Nozzle Flow," AVCO Corporation RAD Report RAD–TR–63–50, (July 1963).
6. H.A. Stine and V.R. Watson, "The Theoretical Enthalpy Distribution of Air in Steady Flow Along the Axis of a Direct Current Arc," NASA TN–D1331, (August 1962).
7. R.R. John, et. al., "Thirty Kilowatt Plasmajet Rocket Engine Development Third Year Development Program," AVCO Corporation RAD Report RAD–TR–64–42, (July 1964).
8. B.M. Rosenbaum and L. Levitt, "Thermodynamic Properties of Hydrogen from Room Temperature to 100,000°K," NASA TN 1107, (January 1962).
9. W.M. Van Camp, F.D. McVey, D.W. Esker, R.J. Checkley, S.E. Merrifield, C.K. Murch, J.H. Painter, V.S. Scognamiglio, "Analysis of an Arc-Jet Exhaust," McDonnell Report A984, (December 1964).
10. R.R. John, et. al., "Thirty Day Endurance Test of a 30 kW Arc-Jet Engine," AIAA Preprint 63–274 (1963).
11. W.B. Davenport, Jr., and W.L. Root, "Random Signals and Noise," pp. 70–71, McGraw-Hill, New York (1958).
12. L.H. Aller, "The Atmosphere of the Sun and Star," Ronald Press, New York, (1953).
13. C.W. Allen, "Astrophysical Quantities," The Athlowe Press, London, (1963).
14. R.L. Fox, "Optical System for Spectrometric Observations of an Axisymmetric Plasma Jet," McDonnell Report 9771, (July 1964).
15. H.R. Griem, A.C. Kolb, K.Y. Shen, "Stark Profile Calculations for the H_β Line of Hydrogen," The Astrophysical Journal 135, No. 1 (1962).
16. R.A. Hill, "Tables of Electron Density as a Function of the Halfwidth of Stark-Broadened Hydrogen Lines," Journal of Quantitative Spectroscopy and Radiative Transfer 4, (1964).
17. J.B. French, "Langmuir Probes in a Flowing Low Density Plasma," UTIA Report No. 76 (AFOSR 2159) (1961).

10 Distribution list

	Copies
NASA Lewis Research Center 21000 Brookpark Road Cleveland, Ohio 44135	
Attn: Spacecraft Technology Division J. H. Childs	1
Attn: Spacecraft Technology Procurement Section J.H. DeFord	1
Attn: Electrothermal Technology Section James S. Sovey	8
Attn: Technology Utilization Office John Weber	1
Attn: Library	2
Attn: Electric Propulsion Laboratory J. Jack	1
Attn: Reports Control Office	1
NASA Headquarters FOB–10B 600 Independence Avenue, SW Washin gton, D.C. 20546	
Attn: RNT/J. Lazar	1
RNT/J. Mullen	1
NASA Marshall Space Flight Center R–RP–DIR Bldg. 4481 Huntsville, Alabama 35812	
Attn: G. Heller	1
NASA Marshall Space Flight Center R–RP–DIR Huntsville, Alabama 35812	
Attn: Dr. E. Stuhlinger	1
NASA Marshall Space Flight Center R–RP–T Huntsville, Alabama	
Attn: K. Schocken	1
NASA Marshall Space Flight Center R–RP–T Bldg. 4488 Huntsville, Alabama 35812	
Attn: W. Jones	1
NASA Marshall Space Flight Center MS–T Bldg. 4488 Huntsville, Alabama 35812	
Attn: Dan Gates	1
NASA Ames Research Center Moffett Field, California 94035	
Attn: Dr. G. Goodwin	1
NASA Goddard Space Flight Center Bldg. 6 Greenbelt, Maryland	
Attn: W. Isley, Code 623	1

Commander
Aeronautical Systems Division
Wright-Patterson AFB, Ohio 45433
Attn: AFAPL (APIE), R. Supp 1
AFAPL (APIE), P. Lindquist 1

NASA Office of Scientific and
Technical Information
AFSS–A
Washington, D.C. 20546 2

NASA Ames Research Center
Library
Moffett Field, California 94035 1

Aerospace Research Laboratories
Wright-Patterson AFB, Ohio 45433
Attn: Mr. Soehngen 1

Oak Ridge National Laboratories
P.O. Box Y
Oak Ridge, Tennessee
Attn: Dr. E. Shipley 1

AFWL
Kirtland AFB, New Mexico
Attn: WLPC/Capt. C.F. Ellis 1

AVCO Corporation
Research and Advanced Development
Division
201 Lowell Street
Wilmington, Massachusetts
Attn: Dr. R. John 1
Attn: Dr. S. Bennett 1

Electro-Optical Systems, Inc.
125 N. Vinedo Avenue
Pasadena, California
Attn: Dr. R. Buhler 1
Dr. G. Cann 1

General Electric Company
Electric Space Propulsion Projects
Evendale, Ohio
Attn: Dr. M.L. Bromberg 1

University of California
Los Alamos Scientific Laboratory
P.O. Box 1663
Los Alamos, New Mexico
Attn: Mr. Thomas F. Stratton 1

Marquardt Corporation
16555 Saticoy Street
Van Nuys, California
Attn: R. Page 1

Giannini Scientific Corporation
3839 South Main Street
Santa Ana, California
Attn: Adriano Ducati 1
J. Todd 1

AVCO-Everett Research Laboratory
Everett, Massachusetts
Attn: R.M. Patrick 1

Aerospace Corporation
P.O. Box 95085
Los Angeles, California 90045
Attn: Library Technical Documents Group 1

Department of Mechanical Engineering
University of Minnesota
Minneapolis, Minnesota
Attn: Dr. E. Ecker 1

NASA Scientific and Technical
Information Facility
P.O. Box 33
College Park, Maryland 20740
Attn: NASA Representative RQT-2448 6

Westinghouse Astronuclear Laboratories
Pittsburgh, Pennsylvania 15234
Attn: Mr. H.W. Szymanowski
Electrical Propulsion Laboratory 1